Pushing cavity-based single photon sources to the limit

Photon feedback, coherent repumping and multilayer cavities

Juan Rafael Álvarez Velásquez
Mansfield College
University of Oxford

A thesis submitted for the degree of
Doctor of Philosophy
Michaelmas 2022

To my family, for showing me the world.
To my friends, for being there for me.
And to my teachers, who inspired me to make it here.
I wouldn’t have made this without your love.

Pushing cavity-based single photon sources to the limit:
Photon feedback, coherent repumping and multilayer cavities

Juan Rafael Álvarez Velásquez, Mansfield College
Department of Physics

Thesis submitted for the degree of Doctor of Philosophy
at the University of Oxford, Michaelmas 2022.

Abstract

This thesis presents important aspects and limitations of an *a priori* deterministic single-photon source using single ^{87}Rb atoms coupled to a high finesse optical cavity. The photons emitted from this source demonstrate long coherence times, interfering over a time of up to 450 ns, demonstrating a two-photon Hong-Ou-Mandel visibility of 0.78 ± 0.04 over the entire photon interaction time, with no degradation of coherence observed when implementing a feedback mechanism to route the photons through a desired output port.

The later chapters of the thesis examine two challenges that arise when trying to improve the scalability of photon production, with the aim of producing streams of several single photons that could be used beyond two-photon interference:

The first is the production of polarised photons, which has been done so far by unfolding the magnetic structure of the atom, a technique that may result in a nonlinear mixing of the states. In this thesis, we examine a way to produce polarised photons that does not need to unfold the magnetic structure of the atom.

The second is the reduction of the cavity mode volume. As higher photon efficiencies are achieved with ever smaller mode volumes, the fabrication of novel cavities could potentially reach a regime where the multilayer structure of the dielectric mirrors becomes relevant to the interaction of an atom with the cavity. This thesis derives coupling factors that take this structure into account.

Acknowledgements

I have been incredibly fortunate to work on such a sophisticated, state-of-the-art experiment for four years. This work did not start, nor will end with me, but it has shown me how transcendental the ideas of atom-cavity interfaces are relative to the greater field of quantum technologies, which has been under constant evolution for the last three decades.

With experimental devices from the second quantum revolution passing from academic prototypes to full-fledged commercial systems, the systems examined in this thesis have enabled us to understand the properties of quantum light and matter in a way that only a small set of other human beings have been able to examine in History. The deep connection of atom-cavity interfaces with other platforms in the field of quantum technologies has given me an excellent ground in which I have been able to learn and observe from other experiments and research groups, something that enabled by the LIMQUET European innovative training network that allowed me to join the research group of Prof. Axel Kuhn as a doctoral student. To have been able to exist, contemplate and reason about such wonderful things is a privilege that I will cherish for the rest of my life.

These acknowledgements are a maximalist effort to thank the people that somehow made part of this endeavour with me:

I would especially like to thank Prof. Axel Kuhn, who has given me the opportunity to make a part of his team and has been a great support, always providing me with creative ideas, guidance, and for believing in me in countless occasions. There have been many times in which Axel believed in me more than I believed in myself.

To the people with whom I shared time in the group: My PhD twin, Mark IJspeert, with whom I have shared more than four years of work. To this day, Mark continues to inspire me with his extreme creativity, his personality and his incredible way of approaching life. It has been a pleasure to share so much time with him in the lab. Tom Barrett, to whom I owe the experimental setup and expertise for helping me set everything up in the beginning, and who has been a friend and inspiration throughout these years. Thomas Doherty, who was always selfless and extremely knowledgeable, and who was always eager to listen to me and provide support. Marwan Mohammed, who inspired me with his curiosity and love for physics, as well as for his ideas and extraordinary questions. Ezra Kassa, who was a great sensei and friend, and who always believed that I would get better in the lab. Ben Yuen, who shared the love of theory with me and with whom I would

sometimes sit and do integrals. Naomi Holland, who showed her passion and great ability for explaining physics to others. Also, to the newcomers to the lab: Chloe So, whose talent and passion are only surpassed by her willingness to help others, and Jan Ole Ernst, who has been a great friend both inside and outside of the lab, even letting me film his rowing crew with a drone. Without a doubt, the group is left in excellent hands. To the previous generations of students in my lab, who laid the foundation for a great experiment: Oli Barter, Annemarie Holleczek, Jerome Dilley, Pete Nisbet and Dustin Stuart: thank you for your hard work. Finally, to those master students I was fortunate to work with: Jiawang Li, who worked hard deploying the demultiplexer shown here, and Lex Joosten. It was a great opportunity to meet you both.

To the ITN LIMQUET and the amazing people that I met there. Astghik Saharyan, who was a close collaborator in the project shown here in Chapter 6and who was always systematic, careful and enthusiastic, and the other students of the project: Kirthanaa Indumathi, Corentin Pignot, Akshay Balgharkashi, Mateja Prslja, Ana Micevic, and so many others who made our conferences and our project such an interesting ride. Also, to Profs Stephane Guérin and Hans Jauslin, who were so kind and welcoming during my secondment in Dijon.

To the people from the demonstrator lab, especially Elizabeth Gallas and Jenny Barnes, who were always so kind and trusting and allowed me to develop my teaching skills in such a nice environment.

To Professor Alejandra Valencia, who was so supportive and set the cornerstone of what has been my career in quantum optics. She has provided open ears and has been there to listen to my ideas, my doubts and my dreams. Working with her has been fun and I owe much of what I know to the work I did with her as an undergraduate. The same can be said about David Guzman, who provided novel designs for the demultiplexing circuits, and who is an excellent teacher and friend.

To my teachers from school times, especially Beatriz Restrepo, Ángela Martinez, Byron Cardona, Gonzalo Henao, Mariela Pemberty and Carlos Toledo. Thank you for instilling in me the joy of learning which has ultimately led me here.

To the friends and collaborators from ICFO and UPC in Barcelona, with whom I kept collaborations during the PhD: Juan P. Torres, José Lázaro, Joan M. Gené, Daniel Urrego, Oscar Cordero, Roberto León-Montiel, Marcello Passos and Arturo Villegas. Their support and ideas have given me confidence and collaborating with them has been excellent to maintain my mind open towards other areas of quantum optics.

To Mansfield College for its generous support and for allowing me to be a Junior Dean, and to the people who worked as deans, porters and caterers. To the staff in Oxford physics, who made all the paperwork easy and swift, and who were always there to help out. Special thanks to Maria Pinto, Álvaro Fachal, Ionela Rosca, Gail Leckie, Simon Moulder, Erin Wheeler, Tom Spasic and Alan Francis.

To the friends I met in physics and who have helped me so selflessly: Gabriel Araneda, who is always so cheerful and friendly, Raghu Srinivas, who liked practicing his Spanish with me, and Mariella Minder, who was fun to be around to talk about reggaetón.

To my friends during the DPhil times: Blas Kolic, without whose moral support this thesis wouldn't have been finished, Pedro Felipe Santos, Gabriel Barrueco, Ana María Marín, Laura Aristizabal, Amir Farzaneh, Mariana Schuster, Eduardo Gutierrez, Pedro Vallejo, Sushanta Mahanta, Leonardo Castro, Santiago Martinez, Rodrigo Leal, Mohini Gupta, Imran Visram, Martin Wachiye, Sofía and María Gómez, Natasha Arroyave, Angélica Cocoma, Jorge Llorente and Alberto Hernández, who were always great listeners and friends with whom it was always nice to go for a walk, or a swim, or tea, or lunch, or a pint. I am so happy and lucky to have met such a variety of incredible people, doing such different and relevant stuff. Meeting you all here has been the stuff that dreams are made of.

To my friends from Europhotonics: Natalia Herrera, Sidd Shivkumar, Anchit Srivastava, Riya Sett, David Saleta and all the europhotonics people. I wouldn't have made it here without your help. I feel very fortunate to have met each and every one of you.

To those friends I met before Oxford and with which I had the fortune of coinciding again: Andrés Ordoñez and Sebastián Murgueitio. They have been great friends and inspiration of who I want to be as a person. This extends to Daniel Ospino and Stacy Sivinski, who I met here and who became great friends of mine. To those friends who have been far from here but close to my heart: Jorge Madrid, Daniel Henao, Pedro Javier Ortiz, Santiago Zubieta, Pedro Pablo Cadavid, Leidys Gutierrez, Mariana García, Santiago Roa, Antoine Bouffard, Juanita Duque, Christian Poveda, Diva Martinez, Valentina Quiroga, Cristina Navarrete, Liliana Ramos, Nicolás Escobar, Lluc Sendra and Piotrek Węgrzyn. Thank you for being such amazing human beings.

To my housemates, who put up with me and were a great support during the pandemic: Matt Mai, Jesse Murray, Jeremy Steel and Dilyan Georgiev. Much of the sanity I retained during the lockdown days I owe to them. Also to Paula Gómez, the first friend I had here in the UK and who made my arrival to this country feel warm and welcoming, and to Carolina Olave, a great friend from Cornell times who certainly made the UK feel a lot like home.

Last, but certainly not least, to my family: Ana Lucía Carreño, who has always provided support and is such a fun person to talk with, my brother Miguel, my sister Cris and my niece Luciana, who have always been so supportive of what I do and for whom I would do anything in the world. To my father Rafael, from whom I would like to believe to have inherited the calm and joy that has kept me going these last years, and especially to my mother Marta, the bedrock of who I am and a great inspiration in everything she does. I hope I grow to be at least a bit like her, and I feel so honoured to have grown under her guidance and inspiration.

I love you all, thank you for being a part of my life.

Contents

List of Figures

List of Tables

Introductory remarks

Some of the work presented in this thesis is adapted from the publications "*How to administer an antidote to Schrödinger's cat*", published in J. Phys. B **55**, 054001 (2022), and *"Light-matter interaction in open cavities with dielectric stacks"*, published in Appl. Phys. Lett. **118**, 154002 (2021).

"To know a thing well, know its limits; Only when pushed beyond its tolerance will its true nature be seen."

— Frank Herbert, Dune (1965)

1

Introduction and motivation

Quantum mechanics is a non-classical physical theory that describes the behaviour of nature at the atomic scale. Its ideas about wave-particle duality, superposition and entanglement have fascinated generations of scientists and non-scientists, and have provided accurate explanations for the behaviour of diverse physical systems such as elementary particles, atoms and solid state systems. These explanations led to inventions such as the laser and the transistor, devices which now make part of our daily life.

The last two decades of the 20th and the first two of the 21st century have seen an explosion of technological breakthroughs which enabled the study of individual quantum systems. The implementation of single-photon and squeezed light sources, the trapping of single atoms in ion and dipole traps, the creation of Bose-Einstein condensates and superconducting qubits, are all demonstrations unthinkable a century ago which have led to the establishment of the *Second Quantum Revolution*[1]. The accuracy of these implementations has also led to the creation of protocols and devices for measuring, probing and simulating nature precisely, as well as opening the door for novel developments in the fields of computing and simulation. Indeed, the work shown in this thesis uses devices that could not be realised or understood without quantum theory, and for which a significant technological development in the quantum technologies was imperative.

Mathematically, quantum systems are described by complex wavefunctions which grow exponentially in complexity as their number of components increase. This poses a fundamental limit on the use of classical computation for the simulation of quantum systems [2]. Understanding these limitations eventually led to the proposal for a universal quantum computer [3], where the use of entanglement and superposition could help to solve problems much more rapidly due to *quantum parallelism:* the idea that the interference of several quantum states yields results that reduce the computational complexity of the problems treated. Some of the most successful algorithms proven with the quantum architecture in mind involved the Deutsch-Josza algorithm, one of the first quantum algorithms to demonstrate an exponential speedup with respect to its classical counterpart[4]; the Grover's search algorithm, which allowed for the much faster solution of database search, reducing a complexity of $O\left(N\right)$ to one of $O\left(\sqrt{N}\right)$ [5]; and Shor's factoring algorithm, which unveiled excitement for the field as it proved that a quantum computer would be able to factor large integers in polynomial time [6], therefore threatening to break cryptographic protocols such as the RSA scheme [7].

These ideas gave way to the implementation of quantum algorithms and devices for quantum computing in the early 2000s, with the field consolidating on the development of ever larger systems. Photons, for example, make for viable candidates as qubits: Photonic quantum computing had early developments and implementations of some of its most important algorithms performed for systems with a small number of qubits. Two of such examples are Grover's algorithm [8] and Shor's algorithm [9], both of which were implemented using photons produced using spontaneous parametric down conversion [10]. The development of the Knill-Laflamme-Milburn (KLM) scheme demonstrated that efficient quantum computation was possible using only beam splitters, phase shifters, single-photon sources and photodetectors [11, 12].

In practice, however, the large number of optical elements, precision in stabilisation and development of stringent quantum memories required for the implementation of a KLM scheme has led to the development of other quantum computing schemes using linear optics. One of these schemes is measurement-based quantum computing (MBQC) [13, 14], where a large, entangled resource state is prepared and then single-qubit measurements are performed yielding the results of the computation. For this, the realization of quantum photonic applications on a sizeable scale depends on the reliable generation of increasing numbers of indistinguishable photons, enforcing the simultaneous arrival of the wave packets of multiple single photons [15, 16].

The development of complex, large-scale quantum computing devices is already underway, with key developments and results claiming improvements with respect to existing classical computers: sophisticated systems comprising hundreds of physical qubits are now being used to perform computations that, according to their realiser's estimations, would take thousands or even millions of years to perform on classical computers [16–18]. In their photonic implementations, the aforementioned demonstrations that claim quantum advantage rely on the interference of either multiple individual photons or squeezed vacuum states for Boson Sampling [18]. In the most recent years, faster classical algorithms have been found for emulating the processes where quantum computing has claimed an advantage [19], but the achievements of the references mentioned in this paragraph constitute proof of the physical implementation of ever larger quantum systems used for performing large-scale computations.

Another application for which quantum technologies has had an increasing interest is the implementation of quantum networks, where the quantum state of spatially separated nodes is shared using quantum channels. The network, and in particular its nodes, could be used for the generation, storage or retrieval of quantum information. Due to the nature of the entanglement and to the non-local correlations that arise from it, these networks would allow for the realization of distributed quantum computations, more powerful than those hitherto achievable by a single quantum computing device [20].

A promising approach is the use of high finesse optical cavities to couple individual states of light and matter, thereby proving a bridge between stationary emitters and traveling photons as carriers of quantum information. Optical single photons can be faithfully transferred over very long distances, on the order of hundreds of kilometres [21], and their non-interacting nature makes their information robust against decoherence. Individual photons can also be tailored to encode information in several degrees of freedom: their time of arrival, which allows for a $d-$dimensional encoding with $d \geq 2$ [22], their polarisation, as well as photon number states [23]. Simultaneously, single atoms, as well as ions, can be isolated by using laser cooling and dipole trapping techniques, and offer the possibility of storing information during extended times. The interaction between atoms and photons is relatively weak in free space, and greatly benefits from the presence of an optical cavity, which enhances the interaction time between the atom and a single photon, while creating a well-defined optical mode into which the atom can emit a photon. A strong coupling within the cavity allows this to be a controllable, deterministic and inherently reversible interaction, essentially establishing an idealised quantum interface [24]. This allows for the generation of light-matter entanglement [25], entanglement swapping [26] and the distribution of cluster states over an extended quantum network [27].

An elementary implementation of a quantum network has been demonstrated using atoms in cavities [24], where the information of a stationary qubit, represented by an atom in a cavity [28], is mapped onto a flying qubit, taking the form of a single photon. Other approaches have also used photons as flying qubits [29], but have chosen ions [26], quantum dots [30] and Nitrogen-Vacancy centres in diamond [31] for their stationary qubits.

A principal component in the effort of realising distributed quantum computing and quantum networks is to improve the scalability of the current architectures and developing methods for the reliable interconnection of distant qubits and quantum processors[32, 33]. Some of the most pressing challenges in these endeavours involve improving the efficiency and reliability with which light-matter interfaces emit and absorb identical photons. In the case of single-atom single-photon interfaces mediated by cavities, two approaches have been taken to tackle the aforementioned challenges.

The first approach has been to generate polarised sources that allow for the production of identical photons. In particular, this includes the photon polarisation, which has to be well-defined: this is also useful for photon routing based in connection with polarisation switching optics. The generation of polarised photons requires the addressing of specific transitions between magnetic sublevels. This can be done by lifting the Zeeman degeneracy in a magnetic field, such that the cavity modes of specific frequencies are only in resonance with the desired transitions . However, another way of ensuring specific transitions with magnetic sublevels is to prepare the atom in only one magnetic substate, thus reducing the number of levels involved in the generation process so that eventually no application of magnetic fields would be required: this is important, as the presence of strong external magnetic fields can reach the nonlinear Zeeman regime and alter the well-known atomic level structure.

For the second approach, some recent light-matter interfaces have resorted to cavities whose cooperativities are larger, requiring the use of ever smaller cavity mode volumes that can be achieved using fibre-tip [34] or tapered [35, 36] cavities, or by requiring ever shorter cavity lengths. Here, the influence and structure of the multilayer dielectric stacks present in the mirrors has to be taken into account.

In this thesis, we will address these two challenges, and explain how to overcome them from a theoretical perspective. This opens the way for new experiments where the cavity design, the multilayer structures on the mirror and the magnetic field landscapes are well understood and used to the advantage of the light matter interfaces.

Furthermore, this thesis also explains experimentally how to produce single photons whose properties can still be influenced in response to the outcome of first measurements on the entire ensemble of photons in the experimental setting.

This thesis is structured as follows: In **Chapter 2,** we introduce the principles of the single-photon source. We describe all the building blocks of the system theoretically for generating both non-polarised and polarised [25, 37] photons between the magnetic sublevels of the D_2 line of ^{87}Rb, while at the same time introducing the relevant equations and parameters for the rest of the thesis. **Chapter 3** describes the experimental components used and how they are connected to produce single-photon states, while detailing the properties of the single-photon source. **Chapter 4** explains an experiment realised using this source which demonstrates the capabilities of the system and the properties of the photons it produces, while implementing a feedback mechanism that allows to change the properties of the emitted photons as they are being produced. We then describe in detail some of the challenges that single-atom single-photon interfaces face when experimentally implemented: strong magnetic fields, which unfold the magnetic structure of the atom in such a way that nonlinear Zeeman effects [37] are exposed. This generates a limited polarised photon production efficiency. In **Chapter 5** we theoretically show how to overcome some of these issues using adiabatic repumping, and report on the implementation of a single-photon demultiplexer using Pockels cells [38, 39], with the aim of producing streams of photons for time-resolved Boson sampling experiments. After reviewing the conditions for producing single photons more efficiently from our sources, we conclude that higher cooperativities -and therefore smaller cavity mode volumes- are required. For this reason, **Chapter 6** examines the effect that mirrors composed of dielectric stacks have on the coupling between an atom and a cavity. After having examined the key results of this thesis, **Chapter 7** provides perspectives for the future directions of the experiment and some concluding remarks.

"If you wish to make apple pie from scratch, you must first create the universe."

—Carl Sagan

2

Producing single photons with atom-cavity interfaces

In the previous chapter, we have discussed some of the aspects that make atom-cavity based single-photon sources appealing for the implementation of efficient and scalable quantum networks. To understand how atoms and cavities can be used as building blocks of quantum networks, this chapter will focus on explaining the key results that have permitted Rubidium atoms in high-finesse cavities to be a viable source of single-photons.

2.1 Atom-cavity interactions

Quantum optics, is an essential theory based on the principles of quantum mechanics that enables the understanding of atom-light interaction. Spontaneous emission, for example, cannot be understood without a full quantum model of light as a harmonic oscillator. Quantum optics describes spontaneous emission as the interaction of an atom with a single mode of the electromagnetic vacuum, which has a non-zero energy and fluctuates over time [40]. When this happens, the atom can be de-excited to emit a single quantum of light, this is, a single photon. If an atom is continuously interacting with a continuum of different vacuum modes, for example, in free space, light emission can happen in any of the modes, allowing the atom to emit light isotropically.

The modes of light to which an atom has access can be engineered using an optical cavity: an arrangement of mirrors that can be used as a resonator for light waves. This allows for light of specific frequencies to interfere constructively while all other frequencies interfere destructively, setting up standing waves in a region of space for a set of optical wavelengths.

In an optical cavity, field amplitudes are substantially increased for a specific set of optical modes with special directions of propagation and wavelengths. Within a cavity, this set of modes enables the alteration of the radiative properties of single atoms coupled to these modes, enhancing [41] or inhibiting [42] their spontaneous emission.

In this section, we examine the main properties and figures of merit that characterise optical cavities. We then describe the interaction of atoms with cavities (section 2.2), using the Jaynes-Cummings model. Finally, we demonstrate how the interaction between atoms and light can be used for the generation of single photons with tunable properties.

2.2 Properties of optical cavities

An optical cavity is an arrangement of mirrors that acts as a resonator for light, enhancing or inhibiting the propagation of light of specific wavelengths and propagation directions. A Fabry-Pérot cavity is the simplest of such devices, consisting of two mirrors between which light is reflected several times.

A simple Fabry-Pérot cavity can be modelled using two mirrors separated by a distance L_{cav} with intensity transmissivities T_1 and T_2 and corresponding reflectivities $R_1 = 1 - T_1$ and $R_2 = 1 - T_2$, as shown in Fig. 2.1. If an electric field E_0 is directed at mirror 1, it is

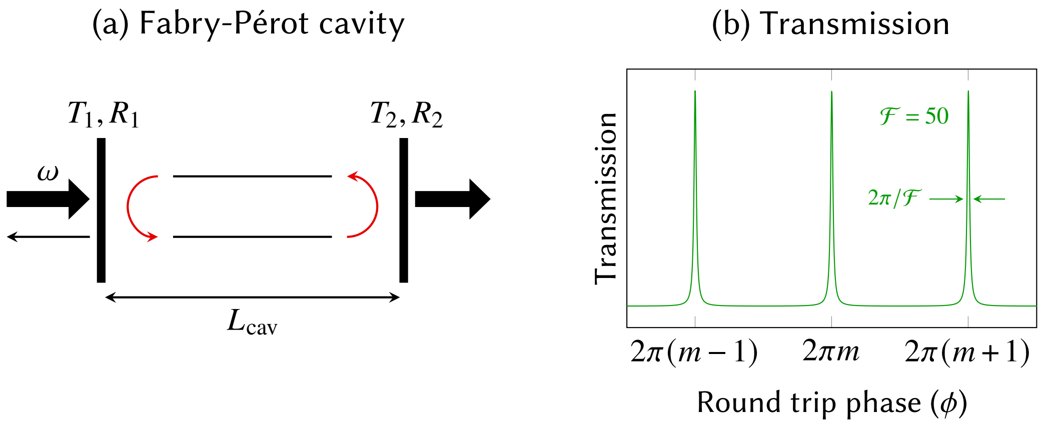

Figure 2.1: (a) Model of a Fabry-Pérot cavity. Two mirrors of transmissivity T_1 and T_2 and reflectivities $R_1 = 1 - T_1$ and $R_2 = 1 - T_2$ are set face to face. The light circulating between builds up a phase ϕ after each trip that depends on the wavelength of the traveling light. (b) Shows the cavity transmission as a function of the round trip phase shift ϕ built in the cavity, which is directly proportional to the value of the angular frequency of the light, ω.

possible to obtain the cavity transmission by summing the progressive transmissions and reflections that the field undergoes as it bounces between the mirrors, while it accumulates a phase of $\phi = 2L_{\text{cav}} \cdot (2\pi/\lambda) = 2L_{\text{cav}}\omega/c$ after each round trip. Assuming that no further losses are present in the system, the cavity transmission is given by [43, 44]:

$$I_T = \frac{T^2}{(1-R)^2} \frac{1}{1 + \frac{4R}{(1-R)^2} \sin^2\left(\frac{\phi}{2}\right)} E_0^2, \tag{2.1}$$

where $R = \sqrt{R_1 R_2}$ and $T = \sqrt{T_1 T_2}$. The light transmission is periodic with respect to ϕ, yielding specific angular frequencies ω_{res} where the field is able to form a standing wave, drastically increasing the intensity of the light enclosed. These resonances occur as integer multiples of $\pi c/L_{\text{cav}}$, a quantity that is known as the free spectral range:

$$\omega_{\text{res}} = \frac{n\pi c}{L_{\text{cav}}} = n\Delta\omega_{\text{FSR}}, n \in \mathbb{Z}. \tag{2.2}$$

It is possible to expand Eq. 2.1 around each of the resonant angular frequencies ω_{res} to find a Lorentzian lineshape in the cavity transmission:

$$I_T = \frac{2}{\pi \Delta\omega_{\text{FWHM}}} \frac{\Delta\omega_{\text{FWHM}}}{4\left(\omega - \omega_{\text{res}}\right)^2 + \Delta\omega_{\text{FWHM}}^2}, \tag{2.3}$$

where the lineshape has a full width at half maximum value $\Delta\omega_{\text{FWHM}}$. By solving Eq. 2.1 for frequencies whose intensity is half the maximum possible intensity, we obtain that

$$\Delta\omega_{\text{FWHM}} = \Delta\omega_{\text{FSR}} \frac{1-R}{\pi\sqrt{R}} = \frac{\Delta\omega_{\text{FSR}}}{\mathcal{F}}, \tag{2.4}$$

where $\mathcal{F} = \pi\sqrt{R}/(1-R)$ is the cavity finesse, which is entirely dependent on the reflectivities of the two mirrors. Conceptually, the finesse can be interpreted as the ratio between the intensities inside and outside the cavity at resonance, modulo a factor of π.

Since the mirrors composing the cavity are partially transmissive, a light pulse circulating within the cavity will partially leak out the cavity mirrors. After each round trip, more and more photons are lost from the cavity, with the intensity decaying exponentially with every reflection. The field is emitted from the cavity at a rate

$$E(t) = E_0 e^{-(\Delta\omega_{\text{FWHM}}/2)t} = E_0 e^{-\kappa t}, \tag{2.5}$$

which provides a characteristic photon lifetime in the cavity, given by [44]:

$$\tau_{\text{cav}} = \frac{L_{\text{cav}}}{c\,(1-R)} = \frac{1}{\Delta\omega_{\text{FWHM}}}. \tag{2.6}$$

This definition also allows us to understand the cavity finesse as the average number of round trips that a single photon makes before leaving the cavity.

The parameters of intensity transmissivity T_1 and T_2 can be chosen to be very different, ensuring that the photon loss occurs with higher probability through one of the cavity mirrors. This will be essential in further chapters for the directional emission of photons.

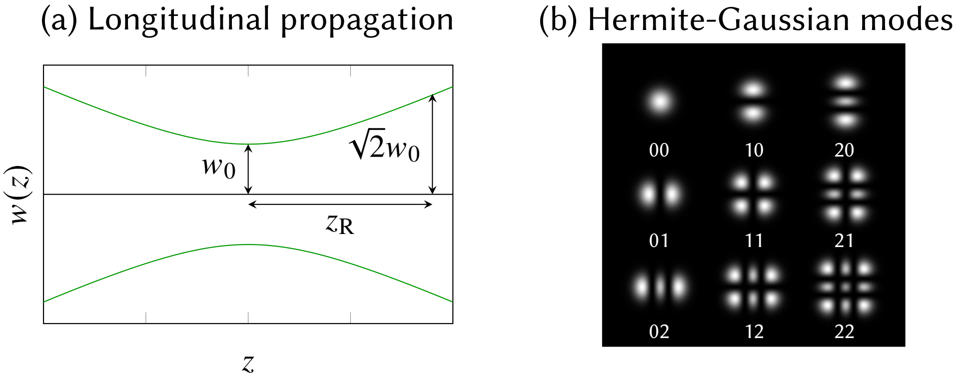

Figure 2.2: (a) Longitudinal propagation of a TEM00 beam within a cavity. (b) Transverse structure of different Hermite-Gaussian cavity modes.

2.3 Transverse structure of cavity modes

In order to ensure that a cavity encloses a finite mode volume, it is necessary to confine the cavity modes also transversely. Practical resonators generally have spherical mirrors whose curvatures must be chosen to ensure that the mode within the cavity does not diverge under successive reflections, ensuring the containment of the light mode within the cavity [36]. Since the longitudinal profile of the stable modes inside a cavity with curved mirrors can be considered to vary slowly with respect to their transverse counterpart, their behaviour resembles that of an almost plane (paraxial) wave [45, 46]. In cartesian and cylindrical coordinates, the fundamental transverse solutions of the paraxial waves within the cavity are either Hermite-Gaussian or Laguerre-Gaussian modes[45–48].

The fundamental Hermite-Gaussian mode is the TEM_{00} (transverse electro-magnetic), whose electric field for a beam of wavelength λ can be expressed as [45, 46, 48, 49]

$$\begin{aligned} E_{00}(x,y,z) =& E_0 \frac{w_0}{w(z)} \exp\left\{ -\frac{r^2}{w(z)^2} \right. \\ & \left. + i\left[\frac{kr^2}{2(z+{z_R}^2/z)} - k(z-\frac{L_{\mathrm{cav}}}{2}) - \Psi_G(z) \right] \right\} \end{aligned} \tag{2.7}$$

for a beam propagating in the z direction. Here, $r^2 = x^2 + y^2$ and $k = 2\pi/\lambda$. The usage of curved mirrors of equal curvature radii enables the propagation of a symmetric TEM00 mode with a waist w_0 at the position $z = 0$. The value of w_0 depends on the radius of curvature of the mirrors R_{cav} and the cavity length, L_{cav}:

$$w_0^2 = \frac{\lambda}{\pi}\sqrt{\frac{L_{\mathrm{cav}}}{2}\left(R_{\mathrm{cav}} - \frac{L_{\mathrm{cav}}}{2}\right)}. \tag{2.8}$$

At a distance z from the waist, the beam has a width given by

$$w(z) = w_0\sqrt{1+\left(\frac{z}{z_{\mathrm{R}}}\right)^2}, \tag{2.9}$$

where $z_{\mathrm{R}} = \pi w_0^2/\lambda$ is the Rayleigh range of the beam, the distance over which the cross-sectional area of the beam doubles. As the beam propagates, it also acquires an additional phase shift, called the Gouy phase, Ψ_{G}, whose value is given by [48, 49]

$$\Psi_{\mathrm{G}}(z) = \arctan\left(\frac{z}{z_{\mathrm{R}}}\right). \tag{2.10}$$

For an arbitrary cavity with an electric field distribution given by $E\left(\mathrm{r}\right)$, the volume of the mode within the cavity is calculated by integrating the electric field distribution inside of the volume of the resonator, as follows:

$$V_{\mathrm{m}} = \frac{1}{\left|E\left(0\right)\right|^2}\int_{\substack{x,y\in\mathbb{R}\\ z\in(0,L_{\mathrm{cav}})}} \left|E\left(\mathrm{r}\right)\right|^2 d^3\mathrm{r}. \tag{2.11}$$

Here, $E\left(0\right)$ is the electric field on the beam axis at the minimum waist, w_0. For a TEM$_{pq}$ Hermite-Gaussian mode volume on a cavity of length L_{cav}, this mode volume is given by [48]:

$$V_{\mathrm{m}} = \frac{\pi w_0^2}{2}L_{\mathrm{cav}}\left(2^{p+q}p!q!\right). \tag{2.12}$$

The mode volume will determine the interaction between the cavity mode and a single emitter within it, as we will see in the upcoming sections. As we will describe in next section, the coupling strength between an atom and the mode of one photon at the place of the atom is inversely proportional to $\sqrt{V_{\mathrm{m}}}$.

One final figure of merit for that characterises the cavities coupling is the extraction efficiency of the cavity, which also takes into account the loss coefficients (L_1,L_2) of the cavity mirrors. If the photon extraction is expected to happen from mirror 2 of the cavity, the extraction efficiency η_{extract} is given by

$$\eta_{\text{extract}} = \frac{T_2}{T_2 + T_1 + L_2 + L_1}. \tag{2.13}$$

2.4 Two-level atoms in cavities

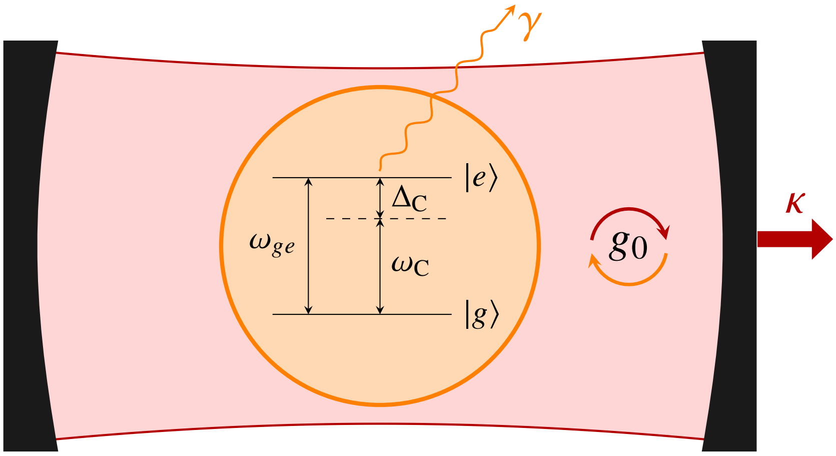

Figure 2.3: Relevant parameters for the coupling of a two-level atom in a cavity. The two-level atom and the cavity interact via the coupling parameter, g_0, which exchanges the excitation of atoms and light in the cavity. The cavity field decays at a rate κ, while an atom within it in the state $|e\rangle$ spontaneously decays with a rate γ. The cavity is tuned to be resonant with a frequency ω_C, detuned from the atomic resonance ω_{ge} by Δ_C.

At the most basic level, the interaction of a single atom with the electromagnetic mode of a cavity can be described using the Jaynes-Cummings model [50]. This model assumes that the electromagnetic field within a cavity, of frequency ω_C, is quantised in a set of discrete levels equally separated in energy, i.e., photon number states $|n\rangle$. Simultaneously, the atom can be modelled as a two-level system with ground state $|g\rangle$, excited state $|e\rangle$, and energy separation $\hbar\omega_{ge}$. A depiction of the atom within the cavity and the relevant parameters is shown in Fig. 2.3. As the cavity field and the atom do not need to have the same frequency, the detuning between them is given by the quantity $\Delta_C := \omega_{ge} - \omega_C$.

The dynamics of the atom-cavity system can be predicted using the Jaynes-Cummings

Hamiltonian, which considers three terms: two independent terms for the atom ($\hat{\mathcal{H}}_{\text{atom}}$), modelled with the Hamiltonian of a two level system:

$$\hat{\mathcal{H}}_{\text{atom}} = \hbar\omega_g \left|g\right\rangle \left\langle g\right| + \hbar\omega_e \left|e\right\rangle \left\langle e\right|, \tag{2.14}$$

and the cavity ($\hat{\mathcal{H}}_{\text{cav}}$), modelled with the Hamiltonian of a Harmonic Oscillator [1]:

$$\hat{\mathcal{H}}_{\text{cav}} = \hbar\omega_{\text{C}}\hat{a}^{\dagger}\hat{a}. \tag{2.15}$$

The third term is a Hamiltonian that describes the interaction between the atom and the cavity. By introducing the atomic state creation and annihilation operators, $\hat{\sigma}^{\dagger} = \left|e\right\rangle \left\langle g\right|$ and $\hat{\sigma} = \left|g\right\rangle \left\langle e\right|$, the interaction Hamiltonian has the form

$$\hat{\mathcal{H}}_{\text{int}} = -\hbar\tilde{g}(\hat{a}^{\dagger}\hat{\sigma} + \hat{\sigma}^{\dagger}\hat{a}), \tag{2.16}$$

where $\tilde{g}$ is an interaction term between the atom and the cavity mode. $\tilde{g}$ is bounded by a maximum coupling g_0[51–54], which for a vacuum field within the cavity is given by

$$g_0 = \left|\boldsymbol{\mu}_{ge}\right| \sqrt{\frac{\omega_{\text{C}}}{2\hbar\varepsilon_0 V_{\text{m}}}}. \tag{2.17}$$

Here, $\boldsymbol{\mu}_{ge}$ is the dipole moment of the atomic transition, ε_0 is the permittivity of vacuum, and V_{m} is the mode volume of the cavity. As mentioned before, this implies that the interaction between any atom and the cavity mode is limited by the size of the mode volume. This can be explained by the fact that the field-atom interaction is given by the field density within the cavity, which is inversely proportional to the mode volume.

For the case where the cavity is in resonance with an atomic transition, we consider that any modes forming within the cavity behave as standing waves with nodes in each of the mirrors. We have seen that the fundamental mode, which has a transverse spatial distribution that follows a Gaussian mode, has a higher intensity in the antinodes of the wave, close to the axis that connects the cavity mirrors. For this reason, atom-cavity

---

[1] whose zero-point energy can be neglected, as it is not relevant for the dynamics of the system.

coupling is never uniform and it depends heavily on the position of the atom within the cavity. In reality, the effective coupling measured in experiments is generally closer to $\tilde{g} \approx 0.7g_0$.

The final Hamiltonian is therefore written as

$$\hat{\mathcal{H}} = \hat{\mathcal{H}}_{\text{cav}} + \hat{\mathcal{H}}_{\text{atom}} + \hat{\mathcal{H}}_{\text{int}}. \tag{2.18}$$

The relationship between the different couplings and decay rates of the atom-cavity system can be characterised using the cooperativity parameter, defined as

$$C = \frac{\tilde{g}^2}{2\kappa\gamma}, \tag{2.19}$$

which can be used to understand the relation that the coherent atom-cavity interaction provided by $\tilde{g}$ has with the incoherent decay rates of the atom (γ) and the cavity (κ). A strong coupling regime occurs when $\tilde{g} \gg \{\kappa, \gamma\}$, which implies $C > 1$. This regime enables the apparition of Rabi oscillations in the atom, with the atom-light interaction dominating over any atom or cavity-related losses. A different behaviour occurs in the bad cavity regime, where the losses through the cavity mode, κ, dominate the interaction: $\kappa \gg \tilde{g}^2/\kappa \gg \gamma$. Here, the emission of light occurs through amplified spontaneous emission[55].

The eigenstates of the Jaynes-Cummings Hamiltonian are mixed atom-photon states, commonly known as dressed states. The degenerate energies of the atom-cavity system unfold, leading to a ladder of energies that connects the atomic ground state $|g;n\rangle$ with the excited state, $|e;n-1\rangle$. Dressed states have the form [44]:

$$\left|\Psi_n^{\pm}\right\rangle = \frac{1}{\sqrt{2}}\left(|g;n\rangle \mp |e;n-1\rangle\right) \tag{2.20}$$

with energies [56]

$$E_n^{\pm} = \left(n + \frac{1}{2}\right)\hbar\omega_C \pm \frac{\hbar}{2}\left(\Delta_{\text{C}} \pm \sqrt{4ng_0^2 + \Delta_{\text{C}}^2}\right). \tag{2.21}$$

Even when no photons are present in the cavity, an atom-cavity system prepared in the eigenstates $\left|\Psi_n^{\pm}\right\rangle$ can be subject to the Rabi oscillation of the atomic population [57].

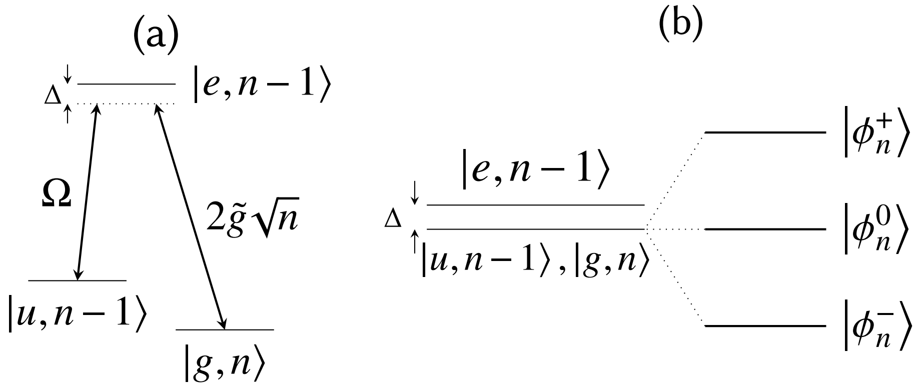

Figure 2.4: When adding an additional ground level in the atom $|u\rangle$, a laser coupling with Rabi frequency Ω and tuning the cavity and laser couplings to Raman resonance, the dressed atom-field states become triplet states with a dark state that enables the transfer of population between the atomic ground states. (a) Shows the energy diagram for the three-level system in Raman resonance, while (b) shows the energy behaviour of the dressed state triplet in Raman resonance, with the dark eigenstate in the middle. This figure is adapted from [55].

Additionally, a splitting in the transmission of a cavity can be seen even when a single atom passes through the cavity mode [58].

2.5 Raman resonance and single photon production

The techniques learned in the previous section allow us to understand the interaction of multi-level atoms with the vacuum field, as well as its use for the generation of single photons using atoms in cavities.

By driving the atom with an additional light field of Rabi frequency Ω (for example, emitted by a laser) and coupling it to a second ground atomic state $|u\rangle$, it is possible to extend the Jaynes-Cummings model to include Raman transitions in a three-level atom. In this case, the interaction Hamiltonian is changed to include the interactions of the laser field driving the transition$|e\rangle \leftrightarrow |u\rangle$, as long as the laser driving and the cavity are only coupled to their respective transitions[55]:

$$\hat{\mathcal{H}}'_{\text{int}} = \hbar\left[\Delta_{\text{L}}\,|u\rangle\langle u| + \Delta_{\text{C}}\,|g\rangle\langle g| - \frac{\Omega}{2}\left(|e\rangle\langle u| + |u\rangle\langle e|\right)\right] - g_0\left(|e\rangle\langle g|\,\hat{a} + \hat{a}^{\dagger}\,|g\rangle\langle e|\right). \quad (2.22)$$

Here, Δ_L is the detuning between the atomic transition ω_{ue} and the laser frequency ω_L. If the detunings are matched to ensure a Raman resonance, i.e., $\Delta_C = \Delta_L = \Delta$, the coupled atom-cavity system will have eigenfrequencies given by

$$\omega_n^0 = \omega_C \left(n + \frac{1}{2}\right), \tag{2.23}$$

$$\omega_n^{\pm} = \omega_C \left(n + \frac{1}{2}\right) + \frac{1}{2}\left(\Delta \pm \sqrt{4ng_0^2 + \Omega^2 + \Delta^2}\right). \tag{2.24}$$

And just like in the previous section, the dressed states will have the form [55, 56]:

$$\begin{aligned} \left|\phi_n^0\right\rangle &= \cos(\Theta)\left|u, n-1\right\rangle - \sin(\Theta)\left|g, n\right\rangle, \\ \left|\phi_n^+\right\rangle &= \sin(\Phi)\sin(\Theta)\left|u, n-1\right\rangle + \cos(\Theta)\left|e, n-1\right\rangle + \sin(\Phi)\cos(\Phi)\left|g, n\right\rangle, \\ \left|\phi_n^-\right\rangle &= \cos(\Phi)\sin(\Theta)\left|u, n-1\right\rangle - \sin(\Theta)\left|e, n-1\right\rangle + \cos(\Phi)\cos(\Phi)\left|g, n\right\rangle, \end{aligned} \tag{2.25}$$

where Θ and Φ are mixing angles defined by

$$\tan(\Theta) = \frac{\Omega}{2g_0\sqrt{n}}, \quad \tan(\Phi) = \frac{\sqrt{4ng_0^2 + \Omega^2}}{\sqrt{4ng_0^2 + \Omega^2} - \Delta}. \tag{2.26}$$

The eigenstate $\left|\phi_n^0\right\rangle$, known as the dark state, does not involve the excited atomic state. Moreover, by changing in the values of Θ (and therefore in the values of Ω for a fixed value of g_0), a transfer of atomic population between ground states is enabled.

By placing an atom in an empty cavity, it is possible to consider only excitations at the single-photon level ($n = 1$), to transfer population between the states in the dark eigenstate $\left|\phi_{n=1}^0\right\rangle$ to produce single photons. The three atomic levels involved are now $|u, 0\rangle$, $|e, 0\rangle$ and $|g, 1\rangle$, coupled respectively to the driving laser (Ω, which couples $|u, 0\rangle$ and $|e, 0\rangle$) and the cavity (whose real coupling $\tilde{g}$ is bounded by g_0, which connects $|e, 0\rangle$ and $|g, 1\rangle$), as seen in Fig. 2.5.

If the atom-cavity system is prepared in the state $\left|\phi_1^0\right\rangle$, it is possible to change the value of Ω (the intensity of the laser beam) adiabatically in order to transfer the population between the ground states $|u, 0\rangle$ and $|g, 1\rangle$ while avoiding any spontaneous emission events [22, 56, 59–61] that occur when the atom is in the state $|e\rangle$. After the value of Θ

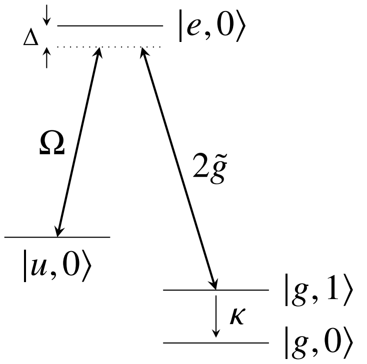

Figure 2.5: The three-level Λ-system used for realising the V-STIRAP process. An additional level for photon decay from the cavity is shown.

is changed from 0 to $\pi/2$, the state has been transferred to $|g,1\rangle$, the field within the cavity decays with a rate κ, eventually leaving the atom-cavity system in the state $|g,0\rangle$, as shown using Eq. 2.5. The adiabaticity required for this process to work, as well as the mediation of the empty cavity gives the method the name of vacuum-enhanced stimulated Raman Adiabatic Passage (v-STIRAP) [62].

In the experimental implementations described in further chapters, photon generation using this method occurs between the hyperfine states of the D_2 line in ^{87}Rb. The ground states generally considered have been the $|u\rangle = |F = 2\rangle$ and $|g\rangle = |F = 1\rangle$ ground states of the atom, while the excited state is the $|e\rangle = |F' = 1\rangle$ state [60]. After the photon has been emitted from the cavity, the state of the atom needs to be brought back to $|u\rangle$, something that is generally done by performing optical pumping, i.e., by exciting the atom with an optical pulse in such a way that the population accumulates in the desired state after several spontaneous emission cycles.

2.6 Control of the amplitude and phase of single photons

The adiabaticity required to avoid spontaneous emission events can also be used to control the dynamics of photon emission from the cavity, and therefore, the amplitude and phase of the photons emitted by the atom-cavity system. Using the triplet of states in Fig. 2.5

and modifying the Hamiltonian of the system to include the non-Hermitian losses caused by cavity decay and spontaneous emission, the dynamics of the system are governed by a time-dependent Schrödinger equation,

$$i\hbar\frac{d}{dt}\begin{pmatrix} c_u(t) \\ c_g(t) \\ c_e(t) \end{pmatrix} = -\frac{\hbar}{2}\begin{pmatrix} 0 & \Omega(t) & 0 \\ \Omega^*(t) & 2i\gamma & 2\tilde{g} \\ 0 & 2\tilde{g}^* & 2i\kappa \end{pmatrix}\begin{pmatrix} c_u(t) \\ c_g(t) \\ c_e(t) \end{pmatrix}, \tag{2.27}$$

where the overall atom-cavity system is in the state $|\Psi\rangle = c_u(t)|u,0\rangle + c_e(t)|e,0\rangle + c_g(t)|g,1\rangle$ at time t.

By imposing a desired single photon wave packet $\psi_0(t)$ in the domain $[0,T]$ with efficiency η, it is possible to link the time evolution of each of the probability amplitudes of the state $|\Psi\rangle$ with the photon wave packet $\psi_{\text{ph}}(t) = \sqrt{\eta}\psi_0(t)$. Following [51], the probability amplitudes are written as

$$c_g(t) = \sqrt{\eta}\psi_0(t)/\sqrt{2\kappa}, \tag{2.28}$$

$$c_e(t) = -\frac{i}{g}\left[\dot{c_g}(t) + \kappa c_g(t)\right], \tag{2.29}$$

$$\Omega(t)\,c_u(t) = 2\left[i\dot{c}_e(t) + i\gamma c_e(t) - g c_g(t)\right], \tag{2.30}$$

As the population of the $|u,0\rangle$ state decreases due to the incoherent channels of spontaneous emission and cavity decay, its value decreases as

$$|c_u(t)|^2 = 1 - |c_e(t)|^2 - \left|c_g(t)\right|^2 - \int_0^t dt\left[2\gamma|c_e(t)|^2 + 2\kappa\left|c_g(t)\right|^2\right]. \tag{2.31}$$

Connecting Eqs. 2.28, 2.29, 2.30 and 2.31, and assuming that $\psi_{\text{ph}}(t)$ is a real function, the Rabi frequency of the driving pulse $\Omega(t)$ is given by the function

$$\Omega(t) = \frac{2\left[i\dot{c}_e(t) + i\gamma c_e(t) - g c_g(t)\right]}{\sqrt{1 - |c_e(t)|^2 - \left|c_g(t)\right|^2 - \int_0^t dt\left[2\gamma|c_e(t)|^2 + 2\kappa\left|c_g(t)\right|^2\right]}}, \tag{2.32}$$

which defines the driving pulse that generates a photon with efficiency η and wave packet

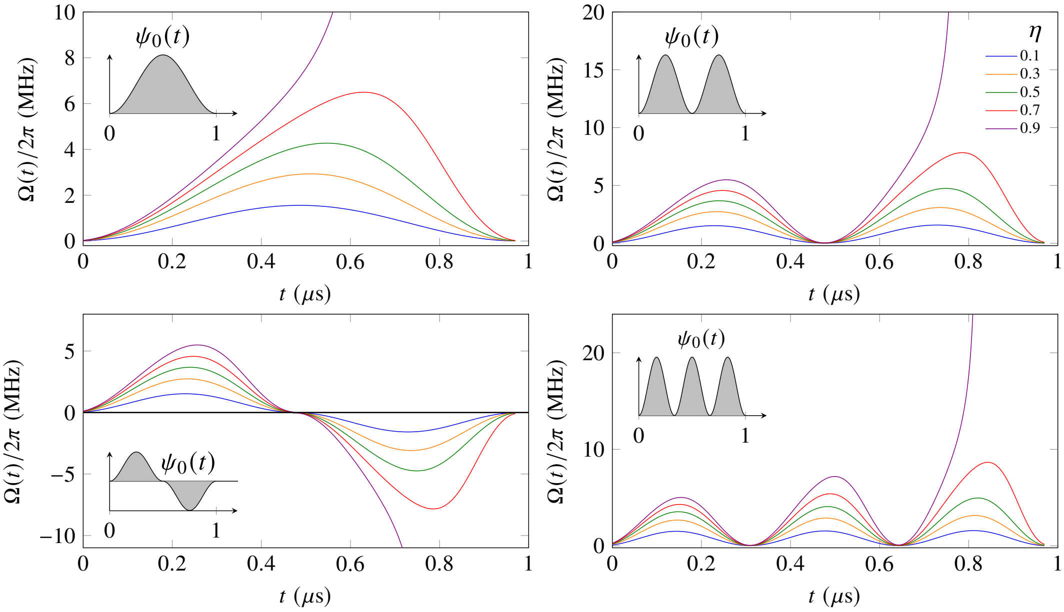

Figure 2.6: This figure shows the required driving pulses to produce the different single-photon wave packets shown in the insets (single, double and triple $\sin^2$ pulse, and double $\sin^2$ pulse with a phase shift of π between its humps) for different efficiencies of $\eta = \{0.1, 0.3, 0.5, 0.7, 0.9\}$ using coupling rates of $\{\tilde{g}, \kappa, \gamma\}/2\pi = \{12, 14, 3\}$ MHz. As mentioned in the text, a diverging photon wave packets corresponds efficiencies that are higher than the physical limit provided by $\eta_{\text{max}} = 2C/(2C+1) = 0.87$. This image is adapted from [63, 64]

$\psi_0(t)$. By choosing $\psi_{\text{ph}}(t)$ to be a real function, $c_g(t)$ will be too, while $c_e(t)$ and $\dot{c}_e(t)$ will be purely imaginary. As a consequence, $\Omega(t)$ in Eq. 2.32 will be a real function. Figure 2.6 shows different driving pulses for the production of single photons of arbitrary shapes with efficiency η. The amplitude, phase and efficiency of the photon wave packets are modifiable, as shown in Fig. 2.6 (c), where the photon amplitude remains the same as in Fig. 2.6(b) but there is a phase shift of π between the first and the second hump of the photon.

Avoiding spontaneous emission by excitation of the atom is a crucial goal for the production of single photons. Nevertheless, it is always possible that experimental conditions make the excited state contribute weakly to a system that is meant to be prepared in the dark state $\left|\phi_1^0\right\rangle$. A bound on the maximum efficiency for producing single photons is found by enforcing that no population lies in the initial state at the end of the pulse, i.e., that [65]

$$\left| c_{uu}(t = T, g, \kappa, \gamma, \eta)|_{\eta=\eta_{\text{sup}}} \right|^2 = 0. \tag{2.33}$$

In this case, an upper bound for maximum efficiency for smooth pulses with smooth derivatives of compact support in $[0, T]$ can be written as

$$\eta_{\text{sup}} = \left[1 + \frac{1}{2C} \left(1 + \int_0^T \left(\frac{\dot{\psi}_0(t)}{\kappa} \right)^2 dt \right) \right]^{-1}. \tag{2.34}$$

For the case of long pulses with $T\kappa \gg 1$, the integral vanishes when T becomes large, making the maximum efficiency limited by

$$\eta_{\text{max}} = \frac{2C}{2C+1}. \tag{2.35}$$

One interesting feature of producing single-photons using temporally shaped driving pulses is that symmetric single photon pulses correspond to asymmetric driving pulses [55]. In the case of a symmetric $\sin^2$ pulse, as the population of the atom-cavity system decreases, it is necessary to increase the Rabi frequency of the system to compensate for the population already depleted from the system. Moreover, from the previous chapter we have seen that the maximum efficiency for photon production is given by Eq. 2.35. This implies that a driving pulse requiring a photon efficiency higher than η_{max} would become diverging, as can be seen in Fig. 2.6 for pulses with efficiency $\eta > 0.9$, as the theoretical maximum for the coupling rates $\{\tilde{g}, \kappa, \gamma\}/2\pi = \{12, 14, 3\}$ MHz is $\eta_{\text{max}} = 0.87$.

2.7 Production of polarised photons

So far, we have described the behaviour of atoms within cavities, as well as the role of external laser fields in the production of single photons when a Raman resonance condition is achieved. Many experimental implementations of the aforementioned photon production systems rely on the loading of alkali atoms like Rubidium or Caesium, whose hyperfine levels serve as the model of the idealised 3-level systems discussed in the previous chapters.

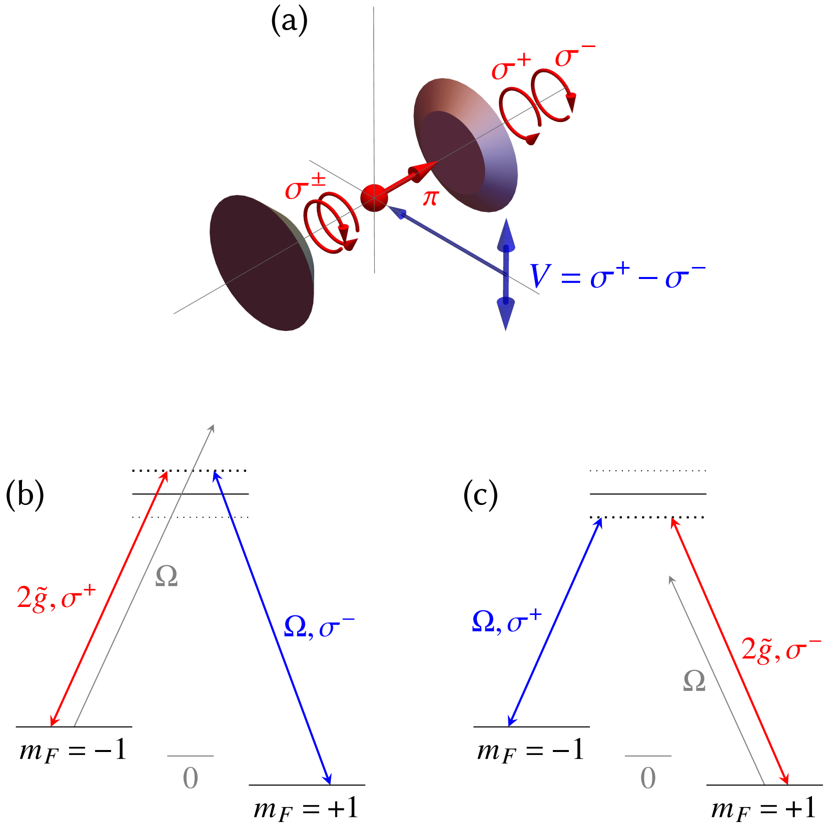

Figure 2.7: Scheme for producing photons of alternating polarisation. (a) The driving pulse, shown in blue, can be decomposed into the σ^+ and σ^- polarisations required for driving the magnetic sublevels of the atom. The frequency of the driving pulse is periodically detuned to create an alternating stream of polarised photons, ensuring that the undesired polarisation of the driving pulse is too far detuned to couple to the levels used for producing photons. This image is adapted from [54].

In general, the hyperfine transitions between atomic levels do not produce polarised photons. Rather, the polarisation of the emitted photons stemming from hyperfine transitions can be considered random or even vary over time, as is the case when a cavity has a significant amount of birefringence[66]. Practical applications require that single-photon sources emit photons that are identical to each other, an idea that we will revisit closely in Chapters 4 and 5. Moreover, the production of polarised photons can also be useful when using deterministic routing switches that allow for the simultaneous arrival of single photons. The routing of photons is customarily used to characterise the quality of the photons produced by means of two-photon interference, an idea that will be explored in Chapter 4.

In order to produce polarised photons, it is possible to address specific transitions between magnetic sublevels in the atom. Generally, this is performed by applying strong magnetic fields that lift the Zeeman degeneracy of the atomic structure [37, 54, 67]. In this way, the cavity modes that address the magnetic transitions are only in resonance with them.

One particular scheme proposed for generating polarised single photons is seen in Fig. 2.7. By using a magnetic field with magnitude B in the orientation of the cavity axis, the $|F=1\rangle$ ground state on the D_2 line of $^{87}\mathrm{Rb}$ is split into three magnetic sublevels, separated in energy by a detuning

$$\mp\Delta_\mathrm{Z} = \mp|g_\mathrm{L}|\mu_\mathrm{B}B, \tag{2.36}$$

where g_L is the Landé factor and μ_B is the Bohr magneton. A driving laser is sent with a polarisation that gets decomposed into the σ^+ and σ^- polarisations of the atom, with the atomic quantisation axis parallel both to the cavity axis and to the orientation of the magnetic field. Keeping the cavity tuned to a fixed frequency, it is possible to periodically detune the frequency of the driving pulses such that a atom-cavity system creates a σ^+-photon followed by a σ^--photon. In this way, the pulse that drives the production of a photon with σ^+ polarisation is also used to prepare the atom in the initial state required to produce a photon with σ^- polarisation. Although this is desirable, as it reduces the time necessary for an atom to be repumped, i.e., the time that an atom is not producing a photon, a failed photon production breaks a long stream of photons irrecoverably.

After photons have been emitted from the cavity, their circular polarisations can be converted into linear polarisations using wave plates, and routed using fibre delay lines that ensure the simultaneous arrival of two or more photons.

2.8 Atomic structure in the presence of a magnetic field

As has been mentioned, a strong external magnetic field can be used to break the degeneracy of the magnetic sublevels in the $|F=1\rangle$ hyperfine state of the D_2 line in

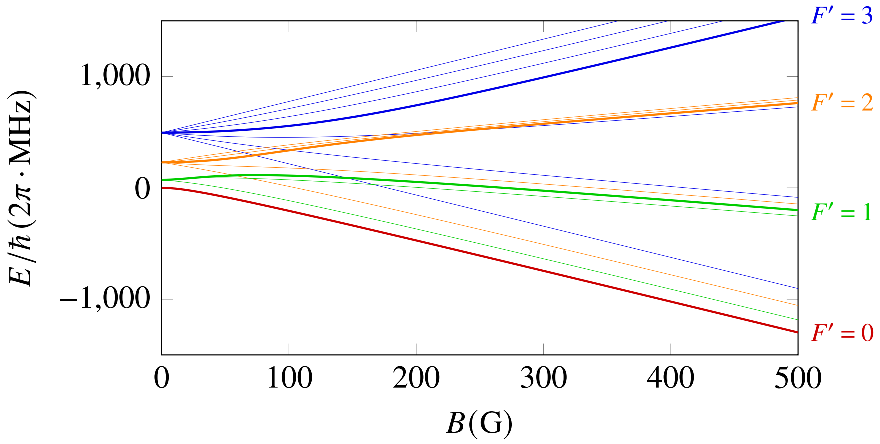

Figure 2.8: This figure shows the energy eigenstates of the excited $5^2\mathrm{P}_{3/2}$ level for the D_2 line of ^{87}Rb line. In the absence of a magnetic field, the levels are separated in energy by the hyperfine interaction, with $|F'=0\rangle$ set to zero. As the magnetic field strength increases, the Zeeman effect lifts the level degeneracies, initially shifting levels linearly proportional to the value of m_F. As the field strengths increase, the states become linear again in the strong-field regime. This time, they are sorted according to their m_I and m_J values, which are decoupled due to the strength of the magnetic field. The states that have $|F, m_F = 0\rangle$ in low fields are shown with thick lines. This figure is inspired in [63, 68].

^{87}Rb. However, the strength of the field (on the order of 20 G) required for a splitting where the driving lasers do not affect unwanted levels is so large in this state (larger than the cavity linewidth, $\kappa \approx 10$ MHz) that it reaches the nonlinear Zeeman regime[37], altering the well-known atomic level structure.

When an atom interacts with a static magnetic field, the Hamiltonian that governs the dynamics of its structure is modified by a Hamiltonian of the form

$$\hat{\mathcal{H}}_{\mathrm{mod}} = hA_{\mathrm{hfs}}\hat{\mathrm{I}}\cdot\hat{\mathrm{J}} - \mu_{\mathrm{B}}\mathrm{B}\cdot\left(g_I\hat{\mathrm{I}} + g_S\hat{\mathrm{S}} + g_L\hat{\mathrm{L}}\right), \tag{2.37}$$

where A_{hfs} is the dipole coupling constant in the ground state of the atom, S, L and I are the spin, angular momentum and nuclear angular momenta operator for the atom, g_{S}, g_{L} and g_{I} are the accompanying electron spin, orbital and nuclear g-factors [69], and $\mathrm{J} = \mathrm{L} + \mathrm{S}$ is the total electron angular momentum of the atom.

As the strength of the magnetic field increases, the coupling between the different magnetic levels changes. Indeed, by considering a Breit-Rabi diagram of the D_2 line of ^{87}Rb, it can be observed how the magnetic sublevels pass through three different regimes.

The two extreme regimes are a weak-field interaction, where the change in energy is linearly dependent on the field strength as the interaction of the nuclear and total orbital angular ($\mathrm{J} = \mathrm{L} + \mathrm{S}$) momentum is stronger than the interaction of either with the external field, and the strong field interaction, in which the interaction of the orbital angular momentum with the external field dominates and the energy level dependence is once again linear with respect to the strength of the external field [37, 68, 70].

The regime in which the field has been historically operated for producing single photons [25, 37, 54] has been intermediate: neither of the aforementioned interactions dominates, making the excited atomic levels interact nonlinearly with the magnetic field. The perturbation introduced by $\hat{\mathcal{H}}_{\mathrm{mod}}$ transforms the hyperfine states $|F, m_F\rangle$ into redefined eigenstates[37, 70] $\left|\tilde{\psi}\left(F, m_F\right)\right\rangle$ which may have contributions from all the former eigenstates of the field-free Hamiltonian. The couplings between two atomic magnetic sublevels i and j, A_{ij}, which have an analytic description in the absence of a magnetic field [70, 71], get modified nonlinearly in the presence of magnetic fields. In the regimes considered here, this state mixing only happens for the excited states.

As an example, the transitions between the ground states $|F = 1, m_F = \pm 1\rangle$ and the excited state $\left|\widetilde{\psi}\left(F' = 1, m_F = 0\right)\right\rangle$ are oppositely affected: while one gets stronger, the other one gets weaker. Moreover, the transition $|F = 1, m_F = 0\rangle \leftrightarrow \left|\widetilde{\psi}\left(F' = 1, m_F' = 0\right)\right\rangle$, initially forbidden, becomes strongly allowed and even surpasses its coupling value with respect to the weaker allowed transition. This is shown in Fig. 2.9.

For the polarised photon production scheme shown in the previous section, a reduced coupling in one of the branches leads to a lower production efficiency for photons with a σ^- polarisation. As mentioned before, the driving pulse also acts as an atomic repumping pulse, making the emission of any given photon dependent on the emission of the previous one. If one of the couplings becomes weaker and asymmetric in the presence of a magnetic field, the emission of the second and all of the subsequent photons becomes drastically impeded.

As a matter of fact, since the transition between the levels $\left|\widetilde{\psi}\left(F', m_F' = 0\right)\right\rangle$ $\rightarrow |F = 1, m_F = +1\rangle$ transition is more efficient than the transition $\left|\widetilde{\psi}\left(F', m_F' = 0\right)\right\rangle \rightarrow |F = 1, m_F = -1\rangle$ in the presence of a magnetic field, the atomic

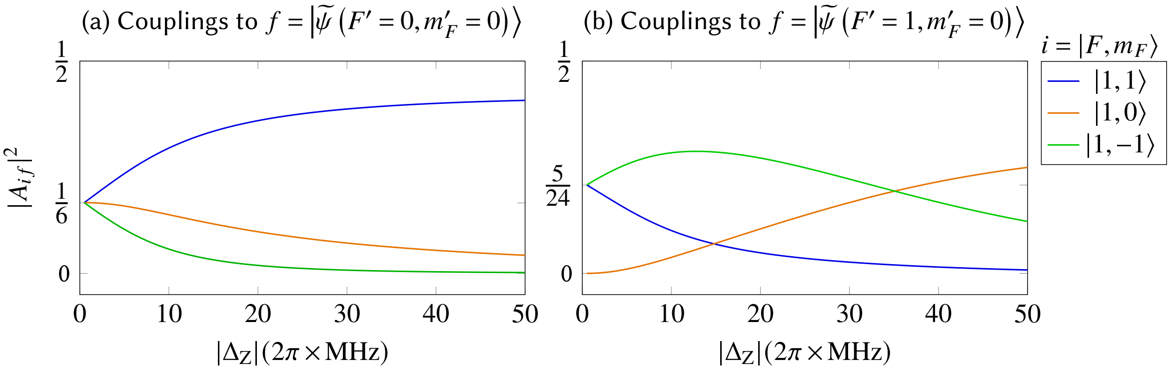

Figure 2.9: Coupling strengths A_{if} from the initial state i to the final state f, dependent on the detuning applied $|\Delta_Z|$ by inducing a static magnetic field (Eq. 2.36). Both figures show the couplings between the three ground states $|F=1, m_F=\pm1\rangle$, $|F=1, m_F=0\rangle$ and the excited states (a) $\left|\widetilde{\psi}\left(F'=0, m'_F=0\right)\right\rangle$ and (b) $\left|\widetilde{\psi}\left(F'=1, m'_F=0\right)\right\rangle$. The couplings change nonlinearly with the field strength, making the forbidden transition $|F=1, m_F=0\rangle \leftrightarrow \left|\widetilde{\psi}\left(F'=1, m'_F=0\right)\right\rangle$ become allowed and stronger than the $|F=1, m_F=1\rangle \leftrightarrow \left|\widetilde{\psi}\left(F'=1, m'_F=0\right)\right\rangle$ used for photon production. This figure has been modified from [63, 66]. As mentioned in the main text, in the presence of the static magnetic field, the ground states can still be considered to have no mixing between them in the magnetic field regimes considered here.

population is unlikely to be repumped efficiently, making it unlikely to recover the state of the atom for producing a subsequent photon.

The method for producing polarised photons discussed here is feasible, and has been shown to work in the past [37, 54]. However, as we have seen, it relies on the lifting of Zeeman degeneracies in a magnetic field that gives rise to nonlinearities. In turn, the production efficiency gets adversely affected, asymmetric and is significantly reduced. In Chapter 5, a promising alternative scheme is introduced that does not rely on the application of magnetic fields to address specific magnetic sublevels in an atom.

2.9 State of the art

The principles mentioned in this chapter have been known and used for several different experimental devices in the last three decades. Here, we examine several of them and their history.

Adiabatic methods that control the population transfer between the ground states of a Λ-system by means of a dark state such as the one presented in the previous chapter have been known as STIRAP [72], an abbreviation of Stimulated Raman Adiabatic Passage. Although STIRAP originated in the early 1990s with applications in chemical dynamics in mind [72–75], the process was popularised from the year 2000 when its use for the interfacing of atoms and light was pioneered by Hennrich *et al.* [59, 62] in the group of G. Rempe. There, three hyperfine levels of a single atom of ^{85}Rb in an optical cavity were used to perform stimulated Raman scattering of a pump laser into the mode of a high-finesse cavity. The Raman scattering was also identified to act as a source of single photons, and was characterised to be a-priori on demand, provided that single atoms were present in the cavity. It also allowed for a narrowband emission, given the high finesse of the cavities used and the precision of atomic transitions. Early implementations of STIRAP methods used continuous lasers: the timing of the interactions was achieved by time-of-flight, with molecules and atoms flying transversely through a pair of overlapping laser beams.

In 2004, the aforementioned source was used to perform the time-resolved interference of two single photons arriving simultaneously at the input ports of a beam splitter [76, 77], a topic that will be discussed carefully in Chapter 4. That same year, the the group of H.J. Kimble demonstrated a deterministic single-photon source [78] by trapping a Caesium atom in an optical cavity for 0.14 seconds.

The source kept being refined, and the ideas for producing polarised photons mentioned in the previous sections were proposed [67] and realised [54] in 2007 by Wilk *et al.*, who lifted the degeneracy of the hyperfine levels in a ^{85}Rb atom to produce polarised photons.

Further efforts to improve the controllability and efficiency of single photons produced with atom-cavity sources were pioneered after 2010, when the shaping of the driving pulses to generate photons with arbitrary wave packets was theoretically proposed [65] and later experimentally realised [60] .

Due to the narrow linewidth of these single-photon sources, their coherence times started to reach timings commensurate with those taken by electronic circuits to perform feedback on experimental systems. This allowed our team to perform partial measurement of two-photon states, enabling an influence in the wave function collapse of a single photon. This is partially recounted in [63, 64, 79], and published in an article titled “How to administer an antidote to Schrödinger’s cat”, which is adapted for inclusion as Chapter 4. The photons produced with this source have also been used to perform quantum operations such as a C-NOT gate, using the photons from our source and silica-on-silicon photonic chips[61].

One of the key applications of these single-photon sources is their application towards the realization of quantum networks. For this, key developments have been the interfacing of single atoms and single photons in 2007 [25, 80], and the proposal of quantum networks with stationary atomic qubits and flying photonic qubits [24, 81]. Over the course of the last decade, different quantum technologies have strived for the realization of elementary two-node quantum networks: some recent examples include trapped ions[82], NV centres in diamond [83] and quantum dots [84]. Moreover, there have been efforts to grow the number of nodes, with a recent result in NV centres implementing a three-node quantum network [85].

In the latest years, the v-STIRAP process has been adapted and improved to use the long trapping lifetimes and gate fidelities of trapped ions, with the intention of realising faithful and reliable quantum networks. Single-photon sources from such systems have been realised (for examples see the work of the groups of Matthias Keller [86–88], Rainer Blatt [89–91]) and Tracy Northup ([92, 93])), overcoming challenges such as the usage of dielectric mirrors close to the ions, which negatively affect the performance of ion trapping.

Finally, a key challenge in the development of atom-cavity based single-photon sources has been the fabrication of cavities with smaller mode volumes, which greatly enhance the coupling between the emitters used and the cavity modes. For this, several approaches have been taken: several research groups in the decade of the 2010’s have implemented fibre cavities, whose small mode volumes greatly enhance the cooperativity of the atom-cavity based photon sources (see, for example, the work of the research groups of Jakob Reichel ([34]), Matthias Keller ([94]) and Dieter Meschede ([95]). Unfortunately, the fabrication of stable fibre-based Fabry-Pérot cavities provides additional complications, as well as difficulties in mode matching for fibre coupling. These difficulties have led to the development of cavities whose mirrors are macroscopic, but tapered in such a way that the mode volumes of the cavities are small, leading to high cooperativities ([35, 36]).

2.10 Conclusions

In this chapter, we have shown the theoretical elements necessary to understand the process of photon production using atoms within cavities. We have described the most important parameters relevant from cavity design, including the mode structure, mirror curvature and field decay. We then explored how the interaction of a cavity with an atom can lead to the generation of dark states, which enable the adiabatic transfer of population between atomic ground states while minimising atomic spontaneous emission. We also showed how the shaping of driving pulses is useful for tailoring the wave packet of single photons, and described how the magnetic structure of an atom is used for producing polarised photons while modifying the coupling of atomic transitions. Finally, we examined the most relevant milestones in the field that have used the techniques of adiabatic passage towards the development of single-photon sources for quantum networking.

"A physicist is just an atom's way of looking at itself."

—Niels Bohr

3

Experimental implementation of an atom-cavity single-photon source

After having described the physical principles required for single-photon production using atoms in cavities, this chapter reviews some of the previous experimental implementations that have produced single photons using atoms in cavities, and details the experimental infrastructure required for producing single photons using an atom-cavity source: the cavity, the atoms used, the mechanisms for laser cooling, the counting and time-tagging modules, and the software used to ensure the correct functioning of the source.

This chapter describes first the historical features implemented by successive iterations of atom-cavity sources (section 3.1) and then recounts the properties and implementation of the current magneto-optical trap and atomic fountain (subsection 3.2), the cavities (subsection 3.3) the laser and locking arrangements (subsection 3.4), the single-photon detection (3.7) and the software to control (3.8) the experimental devices used for this thesis.

3.1 History of the experiment

This is the third iteration of a source initially devised and implemented by Peter Nisbet and Jerome Dilley, upgraded and replicated by Oliver Barter and Annemarie Holleczek in its second generation, and then refined by Thomas Barrett, Dustin Stuart and Oliver Barter in its third generation. The source is itself inspired in the seminal work done in the teams of G. Rempe [54, 59, 96] and H.J. Kimble [78, 97, 98]. Each of these sources was based on the idea of interfacing a high-finesse optical cavity with atoms sourced from a magneto-optical trap (MOT) set up in an atomic fountain configuration. The source's operation is described in detail in the theses of the aforementioned students[52, 64, 99–101], but the bulk of its operation is redescribed here for completeness.

The interfacing of a single atom inside of a cavity is the key element of this experiment, happening for periods shorter than 100 microseconds, with cavities that have optical modes spanning only hundreds of micrometers. Due to the extremely fast velocities that atoms have in atomic vapours, on the order of hundreds of meters per second, the interfacing of atoms requires the use of laser cooling, which diminishes the velocities of the atoms by using a series of lasers and magnetic fields.

Experimental arrangements in the past have dropped a MOT cloud through the cavity mode, limiting the potentially achievable interaction times [54]. More recent developments have focused on the use of different types of dipole traps [35, 95, 102, 103] to localise single atoms and ions within a cavity mode. The use of dipole traps allows experimenters to couple a single atom to the cavity for long times, provided that the distortion of atomic levels by AC-Stark light shifts is corrected. An implementation of a neutral atom in an optical dipole trap within a cavity would allow for improved efficiencies in the production of single photons, greatly improving the ability of this interface as a node for quantum networking. Nevertheless, the effects of light shifts and the frequent re-cooling of the atoms result in a substantially larger experimental complexity. Extensive work inside

[35, 36, 104–106] and outside [102, 107–109] the Atom-Photon Connection research group has been made to trap and control single atoms with dipole traps inside of cavities, but the apparatus reported in this thesis does not contain such a device. Other experimental teams [92, 94] have opted for interfacing trapped ions with optical cavities, using electric fields to hold a single atom within the mode of an optical cavity.

In the device mentioned in this chapter, it has been decided to have the cavity located directly above a magneto-optical trap (MOT), launching it vertically by detuning the trapping beams. A precise detuning of the beams enables the tunability of the launch velocity in the MOT, facilitating precise control of the statistics of the arrival of atoms in the cavity. The cavity and the MOT are placed inside an UHV chamber, where a dispenser provides the Rb gas.

Once atoms arrive at the cavity mode, single photons are generated from the system by applying successive laser pulses to the atom as it interacts with the cavity mode. As it has been shown in the preceding chapter, the temporal shape and intensity of the laser pulses greatly affects the characteristics of the produced photons.

3.2 Laser cooling of ^{87}Rb atoms

In order to contain and confine atoms for times that are large enough to interface them with optical cavities, we first need to reduce their mean velocity. The atoms will be loaded into a cavity using an atomic fountain, but this requires their cooling. This section explains the basic principle behind the functioning of a magneto-optical trap (MOT).

In the experiment, atoms are sourced from a Rubidium dispenser, forming a gas within a UHV vacuum chamber. They are trapped and cooled in a MOT, which uses three pairs of counter-propagating laser beams and a magnetic field to establish a position and velocity-dependent force. Due to the fact that the atoms in a gas move in random directions following a Maxwell-Boltzman probability distribution, the Doppler effect provides a different imbalance of forces to every atom due to the counter-propagating beams.

Let us consider a single atom moving with a velocity v in the direction $+x$. Because of the Doppler shift, the atom will observe an increase in frequency of the light beam that

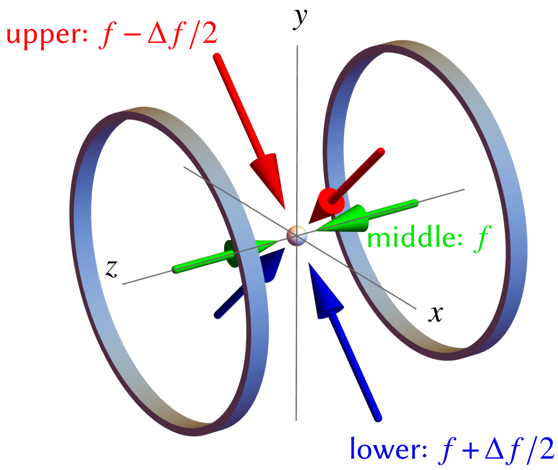

Figure 3.1: This figure shows the orientation and detuning of the MOT beams required to set the atoms moving vertically upwards in an atomic fountain.

it is moving towards, and a decrease in frequency on the beam that it is moving away from. Atoms moving towards a laser beam (of intensity I, on a transition of linewidth Γ with saturation intensity I_{sat}) will absorb photons. Every absorption event provides a net momentum kick in the direction of the beam propagation. This results in a scattering force exerted on the atoms, F_{s}, given by [110]

$$F_{\text{s}}(\Delta) = \hbar k \frac{\Gamma}{2} \frac{I/I_{\text{sat}}}{1 + I/I_{\text{sat}} + 4\Delta^2/\Gamma^2}, \tag{3.1}$$

where $\Delta = \omega - \omega_0 + kv$ corresponds to the detuning of the laser (with frequency ω) from the atomic resonance (ω_0), when considering the Doppler shift from the atom motion. The atom is subjected to a resulting force when moving between two counter-propagating beams. This slows it down, establishing a velocity-dependent force expressed as [110]

$$\begin{aligned} F_{\text{molasses}} &= F_{\text{s}}(\omega - \omega_0 - kv) - F_{\text{s}}(\omega - \omega_0 + kv) \\ &\simeq F_{\text{s}}(\omega - \omega_0) - kv\frac{\partial F_{\text{s}}}{\partial \omega} - \left[F_{\text{s}}(\omega - \omega_0) + kv\frac{\partial F_{\text{s}}}{\partial \omega} \right] \\ &\simeq -2\frac{\partial F_{\text{s}}}{\partial \omega} kv. \end{aligned} \tag{3.2}$$

Here, we have assumed that the atomic velocities are low, i.e., $kv \ll \Gamma$. The imbalance in the forces arising from the Doppler shift constitutes a velocity-dependent force, which exerts damping on the atom, just like a moving particle in a viscous fluid. This velocity dependent behaviour gives this configuration the name of optical molasses [111].

In order to trap atoms for their collection in cavities, a velocity dependent force is not sufficient. In order to add a positionally dependent force, a quadrupole magnetic field can be created using anti-Helmholtz coils, with its zero-point placed at the centre of the optical molasses. This magnetic field creates stronger Zeeman splittings for atoms located far from the molasses centre. As atoms move away from the molasses centre, their energy levels move closer to resonance, therefore increasing the scattering force. If the polarisation of the cooling beams is tuned adequately, with the σ^+ polarisation going in one direction and the σ^- polarisation in the opposite direction, each of the beams addresses only a set of Zeeman transitions. As a consequence, the force exerted to the atom is now position-dependent, and given by [110]

$$\begin{aligned} F_{\mathrm{MOT}} &= F_{\mathrm{s}}^{\sigma^+}\left(\omega - kv - (\omega_0 + \beta z)\right) - F_{\mathrm{s}}^{\sigma^-}\left(\omega + kv - (\omega_0 - \beta z)\right) \\ &\simeq -2\frac{\partial F_{\mathrm{s}}}{\partial \omega}\left(kv + \beta z\right), \end{aligned} \tag{3.3}$$

where βz is the is the Zeeman shift at a displacement z: $\beta = g\mu_{\mathrm{B}}\left(dB/dz\right)/\hbar$.

3.3 The cavities

Three generations of cavities have been used for the experimental realisations presented in this thesis. Two of them are similar in development and scope, with the long-term aim of performing quantum networking experiments with them. The other one is a new prototype, fabricated for the improvement of atom-cavity coupling and the interfacing of cavities with dipole traps.

3.3.1 Traditional design

The cavity design has been the most important experimental aspect that has defined each of the new experimental generations. The two high-finesse cavities under vacuum present in the photon pistol laboratory (017 of the Clarendon Laboratory) are made from BK7 mirrors fabricated by REO in Boulder, Colorado, with curvature radii of $R_\mathrm{c} = 50$ mm. The length of the older cavity is approximately 75 μm, made of mirrors with transmissivities of $\{T_1, T_2\} \approx \{0.5, 40\}$ ppm, while the length of the newer cavity is approximately of 390 μm, made with mirrors of transmissivities $\{T_1, T_2\} \approx \{1, 40\}$ ppm. The old cavity has a measured finesse of $F \approx 74.7 \times 10^3$ and a linewidth of $\Delta_\mathrm{FWHM} = 2\pi \times 23$ MHz [100], while the new cavity's finesse was measured to be of $F \approx 118 \times 10^3$ with a linewidth of $\Delta_\mathrm{FWHM} = 2\pi \times 3.75$ MHz[63]. The newer cavity, with its higher finesse, has been customarily used for the generation of polarised single photons, but it exhibits non-negligible birefringence effects that affect the polarisation of the photons produced with it [66]. Both cavities are made with very similar mirrors, whose losses L_1 and L_2 that do not exceed 2 ppm.

The mirrors from both of these cavities are attached to a non-magnetic stainless steel mount through MACOR ceramic mounts, themselves glued to Noliac shear piezos that are used for displacing each of the mirrors. One of the cavities has been designed with an alignment slot in place. Both mounts have an internal hole to incorporate an eventual dipole trap and provide additional laser driving access.

3.3.2 Tapered cavity

Some recent light-matter interfaces have resorted to cavities whose cooperativities are larger, requiring the use of ever smaller cavity mode volumes that can be achieved using fibre-tip [34] or tapered [35, 36] cavities, where the fabricated mirror facets have a very small radius of curvature that ensures small mode volumes and high cooperativities. The next generation of cavities being fabricated in the R&D laboratory (102 of the Clarendon Laboratory) have been made with such a purpose in mind, as well as their interfacing with dipole traps for atom loading.

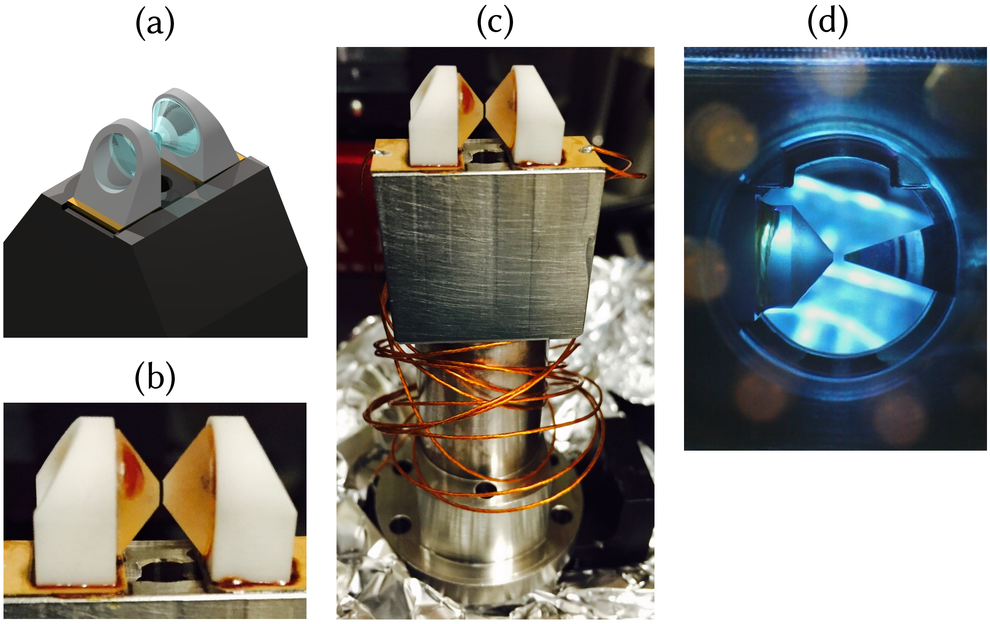

Figure 3.2: (a) This figure shows a 3D render of the first optical cavity, labeled Cav1 in Table 3.1. Cav1 and Cav2 are made of mirrors mounted on ceramic MACOR mounts and Noliac shear piezos, which are glued onto a non-magnetic stainless steel mount. For Cav1, an alignment slot aids in ensuring the motional axes of the piezos are aligned. Cav1 has mirrors of transmissivities $\{T_1, T_2\} = \{40, 1\}$ ppm, a length of 75 μm, a measured finesse of approximately 80×10^3 and a linewidth of $\Delta\omega_{\mathsf{FWHM}} \approx 2\pi \times 24$MHz (Image reproduced from [99]). (b) A detail of Cav2, with a length of 300 μm, a finesse of 150×10^3 and a linewidth of $\Delta\omega_{\mathsf{FWHM}} \approx 2\pi \times 3.75$MHz. (c) The complete cavity mount after bakeout. The alignment slot is absent, but a hole within the mount has been added to incorporate an eventual dipole trap. (Images from (b) and (c) reproduced from [63]) (d) Shows the new, tapered cavity design, using one of the older mirrors from Cav1 and Cav2 in combination with a new, tapered mirror with a smaller radius of curvature ablated in the mirror facet of a pyramidally shaped mirror. (Image (d) provided by Chloe So).

The length of this new cavity is approximately 450 µm, made of two different mirrors: One super-polished out-coupling mirror similar to the ones in the previous cavities and a large radius of curvature, and a tapered, pyramidal mirror [35, 36] with a much smaller radius of curvature of 1.5 mm. The mirrors have transmissivities of $\{T_1, T_2\} \approx \{38.2, 1.75\}$ ppm, a measured finesse of $F \approx 79.3 \times 10^3$ and a linewidth of $\Delta_{\mathsf{FWHM}} = 2\pi \times 4.2$ MHz[35, 36].

3.3.3 Summary

A summary of the most important parameters for this physical system and the three cavities used is shown in Table 3.1.

Name (Symbol)	Cav1	Cav2	Cav3	Units
Length (L_{cav})	74	339	450	µm
Radius of Curvature (R_{cav})	5	5	5 and 0.15	cm
Mirror Diameter ($\varnothing$)	1	1.5	0.3 and 0.1	mm
Mode Waist (w_0)	18.4	26.9	12.2	µm
Mode Volume (V_{m})	4×10^4	3.84×10^5	2.10×10^5	μm^3
Linewidth ($\Delta\omega_{\text{FWHM}}$)	23.7	3.75	4.2	$2\pi\cdot$MHz
Free Spectral Range ($\Delta\omega_{\text{FSR}}$)	2.0	0.442	0.330	$2\pi\cdot$THz
Transv. Mode Splitting ($\Delta\omega_{\text{trans}}$)	35	16.4	15.95	$2\pi\cdot$GHz
Finesse ($\mathcal{F}$)	85×10^3	118×10^3	79.3×10^3	–
Atom-Cavity Coupling (g_0)	15	4.8	11	$2\pi\cdot$MHz
Cavity Field Decay (κ)	12	1.875	2.1	$2\pi\cdot$MHz
Atomic Amplitude Decay (γ)	3	3	3	$2\pi\cdot$MHz
Cooperativity (C)	3.0	2.0	9.6	–
Max. Photon Gen. Efficiency ($\eta_{\text{max}}^{\text{th}}$)	0.86	0.80	0.86	–
Photon Extraction Efficiency (η_{ext})	0.90	0.90	0.50	–

Table 3.1: Summarized cavity and photon-generation parameters. The atomic transition presumed coupled was $|F{=}1\rangle \leftrightarrow |F'{=}1\rangle$ on the D_2 line of ^{87}Rb. The parameters for this can be found in [69], while the cavity parameters have been obtained from [36, 52, 63, 64, 99, 100]. The extraction efficiency of Cav3 is much lower than that of Cav1 and Cav2 as it is a proof of principle cavity whose mirrors are equally transmissive, enabling photon emission through either mirror.

3.4 Lasers and modulators

This section describes all the lasers and modulators present in the optical setup. They are all laid out independently on an optical table physically separated from the optical cavity to ensure stability, adding an additional degree of modularity that permits the driving of two simultaneous experiments. A schematic of the complete laser set-up is shown in Fig. 3.3.

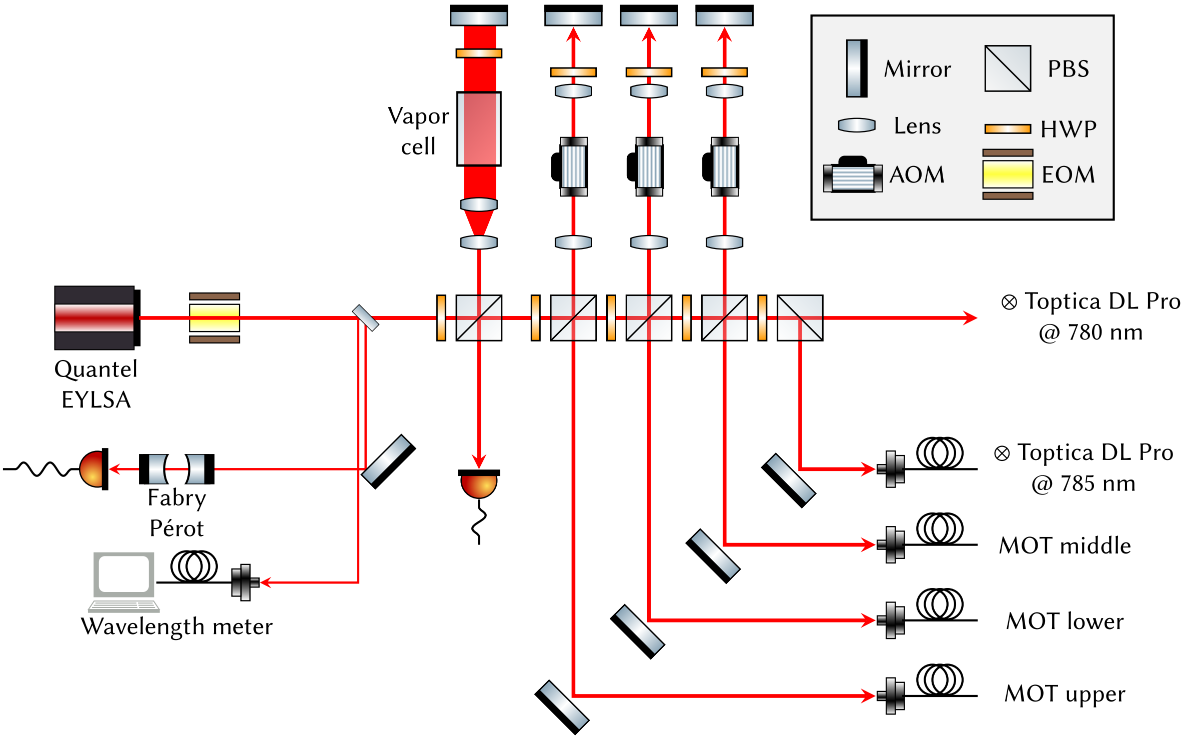

Figure 3.3: Schematic showing the laser set-up used for laser cooling of ^{87}Rbatoms. The cooling laser (upper, Quantel EYLSA 780 fibre laser) drives all of the transitions from the $F = 1$ ground state, with an EOM providing sidebands for continuous repumping from the $F = 2$ levels. Said cooling laser is locked using a Rubidium vapour cell for pump-probe absorption spectroscopy, and its wavelength is measured using a wavelength meter (HighFinesse WS-7). Its beam paths are then split and modified using three double-pass AOMs, which enable the independent tuning of the frequency used for the MOT beams. These beams are then coupled into an optical fibre and sent to another optical table, where they are arranged in the configuration shown in Fig. 3.1.

3.4.1 Laser cooling

For cooling ^{87}Rb, we can use the levels $|F = 2\rangle \longrightarrow |F' = 3\rangle$ from the D_2 line. Since the only decay channel of $|F' = 3\rangle$ is back to $|F = 2\rangle$, a cycling transition is established. There is, nevertheless, a probability that atoms will be excited to the $|F' = 2\rangle$ state, from where the atom may decay to the $|F = 1\rangle$ state that would be too far detuned to interact with the cooling laser. For this, additional light aids to pump atoms from $|F = 1\rangle \longrightarrow |F' = 2\rangle$. From here, the atom would probabilistically decay to the original state, allowing a restart of the cooling cycle. In the experimental setup, the additional light is added using an electro-optical modulator which adds the 6.8 GHz sidebands (the frequency separation between $|F=1\rangle$ and $|F=2\rangle$) to the cooling light for the adequate repumping of the atoms.

The laser used for the main cooling light is a fibre laser, the Quantel EYLSA, locked using pump-probe spectroscopy to a ^{87}Rb vapour cell using a standard Pound-Drever-Hall technique on a Toptica Photonics Digilock module. The EYLSA laser is locked to the resonance $|F=2\rangle \rightarrow C_{13}$ of Rubidium, where C_{13} is the crossover point between the levels $|F'=1\rangle$ and $|F'=3\rangle$: a spectral feature that appears in the transmission spectrum of an atomic vapour when the frequency of a pump-probe beam is exactly between two atomic transitions coupled to the same ground state: The pump and probe beams are resonant with two different transitions within the same velocity distribution, depopulating the ground state and leading to an increased vapour transmission. Additional sidebands around 6.7 GHz are added to the cooling beam using an EOM (iXblue Photline MPZ-LN-10), locked to the $|F=1\rangle \leftrightarrow C_{23}$ transition. These sidebands provide a continuous repumping of the laser beam, ensuring the continued operation of the laser cooling process.

All of the laser beams are tapped off from double-passed AOMs, which ensure that the light addressing the atom and the cavity always has the correct frequency. Three additional double-pass AOMs are added to the upper, lower and central beams of the MOT to control their precise frequencies and, in particular, to drive the atomic fountain described in Section 3.5. These modulators are driven using homebuilt voltage controlled oscillator drivers, driven using DAQ cards connected to the computer (ADLINK DAQ-2502), each one providing 12-bit precision, 10 V outputs, on 8 analogue channels each, updated at up to 100 kHz.

3.4.2 STIRAP

A Toptica DL Pro tunable diode laser is used for driving the STIRAP transitions from the atom in the cavity. This laser is offset locked approximately 6.7 GHz away from the cooling laser, locked around the $|F=1\rangle \leftrightarrow C_{23}$ transition, using a Vescent D2-135 offset phase lock servo capable of performing offset locks by receiving the signal from a fibreised beat note detector, the Vescent D2-160. The D2-135 has an in-built VCO that enables excellent tunability of the laser to other arbitrary frequency points in the D_2 line, ensuring versatility in the system.

Two additional double-pass AOMs are present in the system: one of them ensures adequate cavity transmission of STIRAP light, while the other one is used for driving the atom in the cavity. Additional details on the acousto-optic modulators are provided in Table 3.2.

3.4.3 Frequency comb

As detailed in the previous section, the photon production process is enhanced by locking the cavity to a wavelength that does not correspond to any resonances in the D_2 line of ^{87}Rb. In particular, said locking wavelength is 785.66 nm. The cavities can be stabilised 6 modes red-detuned from the cavity resonance that couples the vSTIRAP transition. Since this wavelength provides no corresponding spectral line for stabilisation, it is possible to stabilise the cavity using a frequency comb that spans this gap.

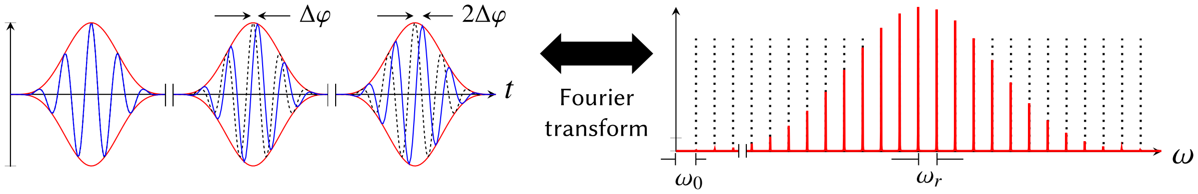

Figure 3.4: The temporal (left) and spectral (right) profiles of the laser pulses that create the frequency comb. Identical pulse envelopes equally spaced in time give rise to a frequency spectrum evenly spaced by the repletion rate, ω_{r}. The different propagation velocities of the envelope and carrier wave result in a phase shift of $\Delta\varphi$ in neighbouring pulses. This gives an overall shift to the frequency spectrum of the carrier envelope offset, ω_0. This is image is adapted from the Menlo Systems FC1500-250-WG User Manual (pg.11).

Our frequency comb is the Menlo Systems FC1500-250-WG, which is based on a pulsed femtosecond fibre laser. In general, the output of a frequency comb can be thought of as a light pulse which circulates in an optical cavity of length L_{cav}, emitting a series of pulses separated by the time that light takes to make a round trip, i.e., $t_{\text{trip}} = 2L_{\text{cav}}/v_g$, where v_g is the group velocity of the pulse. The pulse envelopes are identical, and described by a periodic function $A(t) = A(t-T)$, where T is the period of the pulse envelope. Under a Fourier transform, this pulse train converts into a series of peaks, separated by a repetition rate $\omega_r = 1/T$, as shown in Fig. 3.4, where the pulse train is shown as a function of time and frequency.

Although the function envelopes are the same, the pulse train has a carrier frequency ω_c which leads to differing propagation velocities between the pulse envelope and the carrier wave, making the electric field output non-periodic. The total electric field output from the frequency comb is given by

$$E\left(t\right) = \mathrm{Re}\left(A(t) \cdot \exp\left(-i\omega_c t\right)\right),$$

which under a Fourier transform is written as

$$E(t) = \mathrm{Re}\left(\sum_n A_n \cdot \exp\left(-i\left(\omega_c + n\omega_r\right)t\right)\right) = \mathrm{Re}\left(\sum_n A_n \cdot \exp\left(-i\omega_n t\right)\right), \tag{3.4}$$

Since ω_c may not be a multiple of ω_r, we can renumber the sum in Eq. 3.4 by defining a frequency $\omega_0 < \omega_r$, called the carrier envelope offset (CEO) such that the comb teeth frequencies are given by

$$\omega_n = \omega_0 + n\omega_r.$$

The phase shift buildup that forms between consecutive pulses is given by the presence of ω_0, which leads to an phase shift of $\Delta\varphi$, as well as an overall offset of the comb teeth, $2m\pi \cdot \omega_0 = \Delta\varphi / t_{\mathrm{trip}}$.

A frequency comb is stabilised by mixing its output light with a frequency doubled version of itself. This beat provides a readout of the carrier envelope offset frequency $2\omega_n - \omega_{2n} = \omega_0$, which can be stabilised using a 20 MHz frequency standard, the SRS FS725. The individual frequency contributions of the frequency comb are split using a Bragg grating: by combining the frequency comb output with light from the cooling laser in a Menlo Systems FPD310-FV photodetector, it is possible to lock the spacing of the comb teeth to a value around $\omega_{\mathrm{r}} \approx 250$ MHz.

After the frequency comb has been stabilised in both CEO and comb spacing, it is possible to use its different frequency components to lock the cavity laser to the frequency comb, ensuring a proper phase lock between all the different lasers in the system.

3.4.4 Cavity locking

The Cavity laser is also a Toptica DL Pro laser. As mentioned in the previous subsection, this laser is offset locked to one of the comb teeth from the frequency comb, significantly red detuned from the desired V-STIRAP resonance to which the STIRAP laser is locked.

This laser has been tuned to be resonant with the cavity but very far detuned from the D_2 line resonances, approximately locked around 785.6 nm. This is done with the aim of providing a constant lock to the cavity while not affecting any atomic dynamics. Indeed, there are two Semrock bandpass filters that eliminate all the cavity locking light output while allowing the transmission of the emitted single photons, around 780.2 nm. The dark count rates on the single-photon detectors due to the locking light are negligible, on the order of mHz.

3.4.5 Summary of lasers and modulators

Laser	Modulators	λ	$f = \omega/2\pi$	Details
Cooling		780.246 nm	384.228 THz	Locked to $\lvert F=2\rangle \rightarrow C_{13}$.
	AOM Upper		-(120-200) MHz	Crystal technology 3080-120
	AOM Lower			
	AOM Central			
	EOM		+6.7 GHz	Sidebands at $\lvert F=1\rangle \rightarrow C_{13}$. iXblue Photline MPZ-LN-10
STIRAP		780.232 nm	384.235 THz	Offset locked 6.7 GHz away from the Cooling laser. ($\lvert F=1\rangle \rightarrow C_{13}$.) VCO tunable for versatility.
	AOM cavity		-(120-200) MHz	Crystal technology 3080-120
	AOM drive			
Comb		1050 - 2100 nm	CEO 20 MHz	CEO ($f_0 = \omega_0/2\pi$), is locked to a frequency reference.
			RR ~250 MHz	RR ($f_r = \omega_r/2\pi$) is fixed by locking a comb tooth to the cooling laser.
Cavity		785.656 nm	381.582 THz	Offset locked to a tooth of the frequency comb. Far detuned from the D_2 line.
	AOM		-(120-200) MHz	Crystal technology 3080-120
	EOM PDH		+5-25 MHz	iXblue Photline NIR-MPX800

Table 3.2: Summary of the lasers, modulators and frequencies used by all the devices in the experiment.

3.5 Atomic Fountain

In the two vacuum chambers in the pistol lab, the loading of the atoms happens by using an atomic fountain. In either chamber, the cavity is located 9 mm and 10 mm above the MOT. Here, the magnetic fields are switched off and the atomic cloud is held in a moving molasses. Then, the frequency of the upper and lower beams is detuned relative to the central beam, giving the atomic cloud a velocity of

$$v = \sqrt{2}\lambda\Delta f, \tag{3.5}$$

where λ is the wavelength of the laser and Δf is the relative frequency difference between the upper and lower beams, which is fixed but can be chosen between 0.5 and 1.5 MHz. The atoms are then set in a moving rest frame, and their interaction time with the cavity mode is $t_{\text{int}} = 2\sqrt{2d/g}$, which would be of approximately 4 ms for a 40 μm mode.

As atoms in the MOT and in the atomic fountain have nonzero velocities when launched, the real interaction time between between an atom and the cavity is smaller than the ideal passing time of 100 μs. As the sequence to produce a single photon takes about 1 μs, every passing atom has approximately 100 opportunities to produce a single photon. The atom-cavity interaction durations will be explored in more detail when the single-photon source statistics are analysed.

3.6 Experimental sequence

An experimental sequence for photon production follows a precisely timed sequence. First, atoms are able to gather in a MOT for a loading time of up to one second. After this, they are launched vertically by detuning the lower and upper MOT beams and turning the MOT magnetic field off. After the launch, a continuous sequence of pulses with Rabi frequency $\Omega(t)$ is sent perpendicular to the cavity axis. This enables the generation of STIRAP processes for the production of a single photon in each of the pulses. There are small differences in the driving of the atom-cavity system between the production of polarised and unpolarised photons, which will be detailed in the next subsections:

3.6.1 Unpolarised photon generation

For the generation of unpolarised photons, the atomic levels chosen for the vSTIRAP driving are the $|u\rangle = \left|5^2\mathrm{S}_{1/2}, F=1\right\rangle$ and $|g\rangle = \left|5^2\mathrm{S}_{1/2}, F=2\right\rangle$ ground states of the D_2 line of ^{87}Rb. They are coupled in a Λ-scheme to the excited state $|e\rangle = \left|5^2\mathrm{P}_{3/2}, F'=1\right\rangle$ with a driving laser of Rabi frequency $\Omega(t)$. The cavity decay rates and coupling strengths follow the column Cav1 of Table 3.1. An acousto-optic modulator is used for changing the Rabi frequency $\Omega(t)$, enabling the generation of photons with arbitrary wave packets.

Unpolarised photons are emitted at a repetition rate of 1MHz, with a portion of the cycle (approximately 400 ns) used to produce a single photon. The remaining time of the cycle, 600 ns, is used for the optical pumping of the atom to the state $|u\rangle$, which enables the cycle to be restarted. With atoms being present in the cavity for about 100 microseconds, there are approximately 100 opportunities at generating a single photon per atom used. In reality, the number of single-photon events recorded does not exceed 20 counts per atom, with approximately 10 atoms passing by the cavity in each MOT throw.

3.6.2 Polarised photon generation

While atoms are launched from the atomic fountain, the magnetic field used to lift the hyperfine level degeneracy is activated. Atoms take approximately 60 μs to interact with the cavity, and the magnetic field is activated approximately 3 ms before any atoms reach the cavity. Since the atoms are generally left in the $|F = 2\rangle$ state by the MOT, a short (100 ns) depumping pulse is used to bring any atoms that may have decayed to this state back into the $|F = 1\rangle$ manifold.

Polarised photons can be emitted in rates of up to 1.5MHz, with a production cycle lasting up to 664 ns. Unlike the unpolarised cycle, the polarised photon cycle alternates the choice of the magnetic sublevels $|g\rangle = |F = 1, m_F = 1\rangle$ and $|u\rangle = |F = 1, m_F = -1\rangle$ as ground states by changing the detuning of the driving pulse with Rabi frequency $\Omega(t)$. The excited state is the level $|e\rangle = |F' = 1, m_F = 0\rangle$.

3.7 Single-photon detection

3.7.1 Avalanche photodiodes

Originally, the devices used for the detection of photons were single-photon counting modules (SPCMs), containing avalanche photodiodes with a quantum efficiency of 60-65% and a resolution of < 300 ps (Excelitas SPCM-AQRH-780-14-FC). These devices have dead times of 22 ns and large dark count rates on the order of 60 Hz, leading to unexpected noise and unwanted correlations. The small dead times of these detectors and large time durations of the photon wave packets enables the time-resolved detection of single photons, which will be explored in the next chapter.

3.7.2 Superconducting nanowires

As a consequence, experiments involving the polarised single-photon source (some examples of these can be found in Refs. [27, 37, 66]) have used eight superconducting nanowire single-photon detectors (SNSPDs) fabricated by Photon Spot (NW1FC780), embedded within a single cryostat. These devices have better time resolutions, of approximately 81 ps. On average, each of the detectors has a detection efficiency averaging 80%, including those losses generated by fibre coupling. Unlike the avalanche photodiodes, the dark count rates of the SNSPDs are extremely low, not exceeding the 20 mHz, while their dead times is typically of 50 ns.

3.7.3 Photon counting logic and data recording

The detected photons are counted with an 81 ps accuracy using a qutools quTAU Time to Digital Converter (TDC). This device enables a precise recording of events that enables to understand the time-resolved properties of single photons, as well as their correlations across detectors.

Every photon detection records four parameters:

1. The channel that recorded the detection
2. The time that has elapsed between the start of $\Omega(t)$, called t_{STIRAP}.
3. The time that has elapsed since the MOT was launched vertically, t_{MOT}.
4. The pulse number, n_{pulse}.

3.8 Experimental control

The operation of the whole experimental system requires the synchronisation of modulators (AOMs and EOMs, for controlling beam intensity in the experiment), magnetic field coils, voltage controlled oscillators, single-photon detectors and time-to-digital converters. This task is realised using a custom Python interface that controls three synchronised DAQ cards (ADLINK DAQ-2502), each one providing 12-bit precision, 10 V outputs, on 8 analogue channels each, updated at up to 100 kHz. Additionally, an Arbitrary Waveform Generator (Tabor WX1284C) is used for the writing and driving of pulses in the acousto-optic and electro-optic modulators, essential for the shaping of the amplitude of the driving pulses in the cavity. Its operation and activation is also controlled by the software, which sends an AWG trigger signal.

3.9 Data processing

The data recorded by the single-photon detectors is processed to understand the properties of the single-photon source. This data contains a significant amount of noise coming from detector dark counts and other stray photons, which need to be corrected for. This section accounts the procedures that are performed in the raw data:

3.9.1 Separation of data into signal and noise

It is possible to aggregate the experimental data introduced in section 3.7.3 in different ways, one of which is to perform a histogram of the data following the recording of the t_{STIRAP} data. This exhibits three important features on the experimental data: the first are the dark counts on the single-photon detectors, which can reveal photon counts even when there is no light expected. The second is the repumping cycle, which can be identified as a square function after the photon detection. The last feature is the shape of the photon wavepacket. We fit the following function to the raw data in each detector, grouped by :

$$g(t) = a + \begin{cases} b\sin^2\left(\frac{\pi n_{\text{humps}}(t-p_1)}{p_2-p_1}\right) & \text{for } p_1 < t < p_2 \\ c & \text{for } p_3 < t < p_4 \end{cases} \tag{3.6}$$

Here, p_1 and p_2 encompass the times for photon arrivals, while p_3 and p_4 correspond to times when the repumping is triggered. The time between p_2 and p_3 is used to obtain the dark count rates of the single-photon counting modules. This fitting is shown in Fig. 3.5

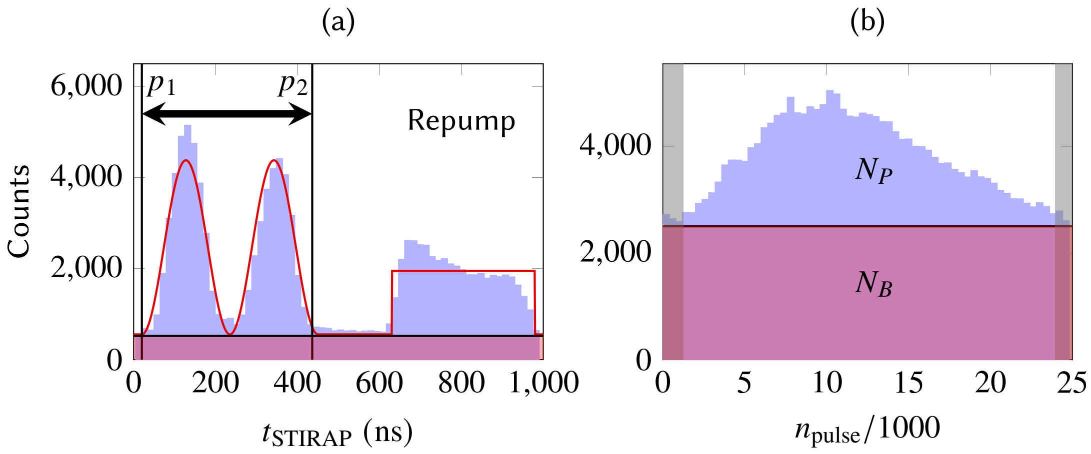

Figure 3.5: (a) Shows one particular curve fit of the photon shape and the repumping following Eq. 3.6. The photon duration begins in p_1 and ends in p_2. (b) Shows a histogram of the total number of photon detections in each of the pulse durations. This allows us to distinguish the distributions from the photon counts, N_P, and those from the background counts, N_B. This is typical data collected by O. Barter [64] using the non-polarised single-photon source. Although the background counts look larger in (b), this is a consequence of grouping signal and noise according to either the time elapsed since the last STIRAP pulse or the time elapsed since the MOT launch.

(a).

3.9.2 Correlation corrections

Additional corrections in the background must be made for those cases where correlations are examined. This can be done by investigating the distribution of all detection events as a function of the pulse number, n_{pulse}. A typical MOT time distribution is found in Fig. 3.5 (b), showing the profile of an average atom transiting the cavity. The background level provided by the detector counts is evident as counts persist even when there are no atoms are in the cavity.

The window in which we consider it possible for atoms to be present in the cavity – and so the data that must be filtered for correlations – is shown in the unshaded area of Fig. 3.5 (b). From this histogram it is possible to extract two distributions for every detector X, describing the detection events due to photons emitted from atoms, $n_{\text{P}}^{(X)}(t)$,

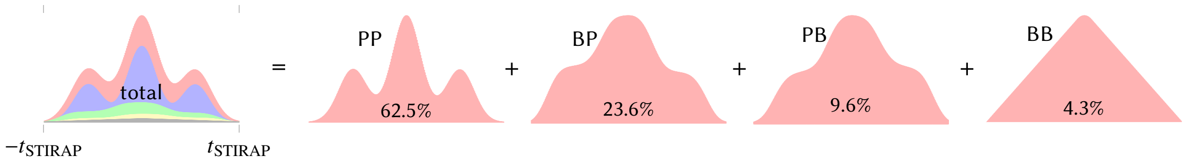

Figure 3.6: Background corrections. The figure shows typical contributions for the four components of the background elimination, $M_{\text{BB}}^{(C)(D)}(\tau), M_{\text{BP}}^{(C)(D)}(\tau)$, $M_{\text{PB}}^{(C)(D)}(\tau)$ and $M_{\text{PP}}^{(C)(D)}(\tau)$, as would be extracted from a data histogram such as that in Fig. 3.5. Due to the different dark count rates in each of the single-photon detectors, the *BP* and *PB* contributions are asymmetric.

and true background detections uncorrelated to atoms, $n_{\text{B}}^{(X)}(t)$. These can be defined as

$$N_{\text{P/B}}^{(X)} = \int_0^{T_{\text{MOT}}} n_{\text{P/B}}^{(X)}(t)dt. \tag{3.7}$$

Here, T_{MOT} is defined as the total MOT time recorded for each throw. In the case of the experimental data shown in the picture, the 25000 pulses, each 1 μs, long, yield a value of $T_{\text{MOT}} = 25$ ms.

When considering the correlations between two detectors, which could either be avalanche photodiodes or superconducting nanowire detectors, both introduced in Section 3.7, it is necessary to consider the different correlation contributions between all the pairwise combinations of distributions. Across two detectors A and B, for a delay of τ, these are $N_{\text{BB}}^{(A)(B)}(\tau)$, $N_{\text{BP}}^{(A)(B)}(\tau)$, $N_{\text{PB}}^{(A)(B)}(\tau)$ and $N_{\text{PP}}^{(A)(B)}(\tau)$, where

$$\begin{aligned} N_{\text{ij}}^{(A)(B)}(\tau) &= \int_0^{T_{\text{MOT}}} n_{\text{i}}^{(A)}(t) n_{\text{j}}^{(B)}(t+\tau)dt \\ &= \left(n_{\text{i}}^{(A)} * n_{\text{j}}^{(B)}\right)(\tau), \end{aligned} \tag{3.8}$$

and i,j $\in \{\text{B}, \text{P}\}$. The total background corresponds to the summation of all contributions

$$N_{\text{total}}^{(A)(B)}(\tau) = N_{\text{BB}}^{(A)(B)}(\tau) + N_{\text{BP}}^{(A)(B)}(\tau) + N_{\text{PB}}^{(A)(B)}(\tau) + N_{\text{PP}}^{(A)(B)}(\tau), \tag{3.9}$$

which are shown in Fig. 3.6.

One important question can arise from this. It may seem counterintuitive to eliminate any photon-photon correlations from the data, as this is precisely a signal of interest.

However, the term $N_{\mathrm{PP}}^{(A)(B)}(\tau)$ does not represent two-photon correlations from the emission of a single atom, but rather, from the emissions of two different atoms that happened to be loaded at the same t_{STIRAP} time. By contrast, any of the two-photon correlations intended to identify quantum effects happen only in small times, and are examined by looking at the second-order correlation function of the source, a topic that will be examined in the next section. We presume and require only one atom to be coupled to the cavity for our single-photon production and so these two-atom events comprise a background to the cases in which we performed our desired experiment.

3.10 Performance of the single-photon source

After having examined how to experimentally record the measurements of light produced with atom-cavity systems, this section examines one part of the performance of the single-photon source: its performance as a single-photon source, which can be determined by a set of metrics regarding the temporal arrival of several single photons.

3.10.1 HBT measurements and source singleness

One of the most important ideas for characterizing a single photon as such is to use the correlations in the detection statistics of two distant detectors, an experimental arrangement called a Hanbury-Brown and Twiss (HBT) measurement. This measurement was born from the field of astronomy, where it was used for characterizing the properties of the light emitted by distant stars [112].

HBT measurements acquired relevance in experimental quantum optics from 1977, when the group of L. Mandel [113] observed the statistics of resonance fluorescence in a sodium atom, obtaining the first measurement of photon antibunching and the first experimental realization of a single-photon state [114], jointly with the group of A. Aspect [115].

Consider two beams of light arriving into two detectors after a beam splitter, labeled I_1 and I_2. It is possible to define the second-order correlation function of a light source as

[116]

$$g^{(2)}(\tau) = \frac{\langle I_1(t) I_2(t+\tau)\rangle}{\langle I_1(t)\rangle \langle I_2(t+\tau)\rangle}. \tag{3.10}$$

The fields leading to this second order correlation function can be quantized, leading to a rewriting of the $g^{(2)}$ function with the probability of single-photon detections in detectors 1 and 2, $P_{1/2}(\tau)$, and the probability of joint single-photon detections in detectors 1 and 2, $P_{12}(\tau)$:

$$g^{(2)}(\tau) = \frac{P_{12}(\tau)}{P_1(t) P_{12}(t+\tau)}. \tag{3.11}$$

Ideally, a single-photon source impinging on a 50:50 beam splitter yields $g^{(2)}(0) = 0$. As single photons cannot take two beam splitter paths, any single photon impinging on a beam splitter must go to either detector. Fig. 3.7 shows the total correlations of a single-photon stream after a beam splitter across two detectors, which have a central dip due to this phenomenon. Nevertheless, experimental errors sometimes lead to remnants of multiple photon emission, explaining why the central dip in the $g^{(2)}$ function does not go to zero. The inset in Fig. 3.7 shows the correlations corresponding to photons emitted within a few driving pulses of each other.

3.10.2 Single-photon routing

3.10.2.1 Unpolarised photons

After being generated by driving the hyperfine levels of the atom, emitted photons on the unpolarised scheme impinge on a polarising beam splitter (PBS), which randomly routes them into into two optical paths, as shown in Fig. 3.8. As the photons are emitted with random polarisations, each of the photons has a 50% probability of being output on either beam splitter port. If one of the output ports is connected to a fibre loop with its optical path length equal to the duty cycle of production of a single photon (300 m, for a 1 μs delay), there is a 25% probability of obtaining two photons simultaneously arriving at the input ports of a beam splitter. A half wave plate (HWP) can be used to set the relative polarisation of both photons.

3.10.2.2 Polarised photons

Polarised photons, alternating in polarisations σ^+ and σ^-, are converted into linear polarisations H and V after using a quarter wave plate. After this, a polarising beam splitter transmits photons with H polarisation to one output path, and reflects photons with V polarisation to another path. As a V-polarised photon is always emitted after a H-polarised photon, one of the paths is combined with an optical fibre delay that has a path length difference equal to the duty cycle of the photon production process. This ensures that both photon wavefronts are equal, something that is essential for the interference of two photons at the input ports of a beam splitter. A diagram describing this process is shown in Fig. 3.9.

3.10.3 Normalisation

Due to experimental errors in detectors such as losses and dead times, it is not possible to identify directly how many individual photon-pair experiments were performed by counting the number of detection events measured in one detector. To overcome this, it is possible to identify that the number of events happening simultaneously is related to the number of events happening separated by two duty cycles, following the relation [64]

$$N_0/N_2 = \frac{\eta_L}{1+2\eta_L+\eta_L^2} \simeq 1/4, \tag{3.12}$$

where η_L is the probability of photon transmission in the long fibre delay.

3.10.3.1 polarisation control

Finally, we examine the production efficiency of each of the polarisations in the polarised photon scheme. In this case, the emitted photons, with a circular polarisation, are sent into a wave plate to maximise the routing into different detection arms. The detection statistics of σ^+ and σ^- photons are similar, implying that a routing of two photons indeed occurs, increasing the probability of two-photon events. The histogram in Fig. 3.10 does not show the conditioning of emission, which would demonstrate that the probability of emitting a σ^+ photon after a σ^- photon is much higher than the opposite case, something that has been amply studied in the past [37, 54]. Moreover, the cavity is birefringent and the frequency sustained by the cavity for each polarisation is different. As a consequence, the emitted photon polarisation evolves over time [66], inevitably enforcing an imperfect routing of alternately polarised photons. This, added with an imperfect polarisation preparation, explains why some of photon detections inevitably happen on even pulses.

3.10.3.2 Distinguishability

Single-photon sources can also be characterised based on the distinguishability of the photons they emit. For this, we require the interference of two single photons that arrive at the input ports of a beam splitter. We have already explained how to make two photons emitted from the same source arrive at the input ports of a BS, but given that a discussion about photon distinguishability requires the understanding of two-photon interference, its discussion is relegated to Chapter 4.

3.11 Conclusions

In this chapter we have discussed the most important experimental aspects used for generating single photons using atoms of ^{87}Rb loaded through an atomic fountain to high-finesse cavities. The development of the source touches on many different aspects and milestones of atomic and laser physics: the development of laser cooling and atomic fountains for atom loading, the fabrication of high-finesse cavities, the usage of frequency combs as references for laser stabilisation, as well as the control and characterisation of single-photon sources using Hanbury-Brown and Twiss measurements. All of these topics enabled the development of a complex experimental device with an excellent degree of controllability. Indeed, this source can produce single photons with controllable wave packets of long duration. The next chapter discusses how such a source can be used to understand, characterise and control the process of two-photon interference.

(a) Unpolarized source $g^{(2)}(\tau)$

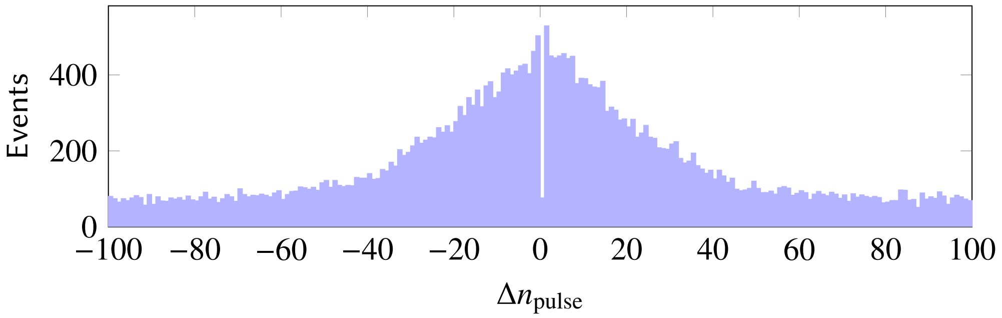

(b) Polarized source $g^{(2)}(\tau)$

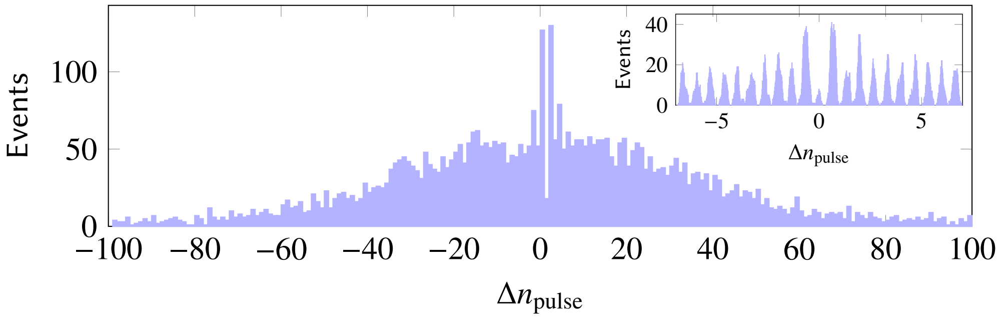

Figure 3.7: Uncorrected Hanbury Brown-Twiss second order correlation function, $g^{(2)}$ for the polarised and unpolarised sources. The correlations in a Hanbury Brown-Twiss set-up are aggregated in a histogram according to the detection pulse number difference. For (a), the unpolarised source, each of the driving pulses plus its repumping is 1000 ns long. For (b) the driving pulse is 664 ns, without a repumping time. The missing central peak in both figures is a symbol of the low probability for generating two photons within the same driving pulse, ensuring the singleness of the photon source. The inset in (b) shows a sliding histogram of the central ±10 detection pulse differences. The source for this data was taken from [63, 64]. The polarised source shows a bunching behaviour which is more peaked around $\Delta n_{\text{pulse}} = \pm 1$, while decaying rapidly. This is potentially due to the fact that the production of streams of more than two photons become harder to produce due to the apparition of nonlinear Zeeman effects, ensuring that the single atoms generally emit only pairs of photons at a time before losing the atomic coherence and thus the correlations with further photons.

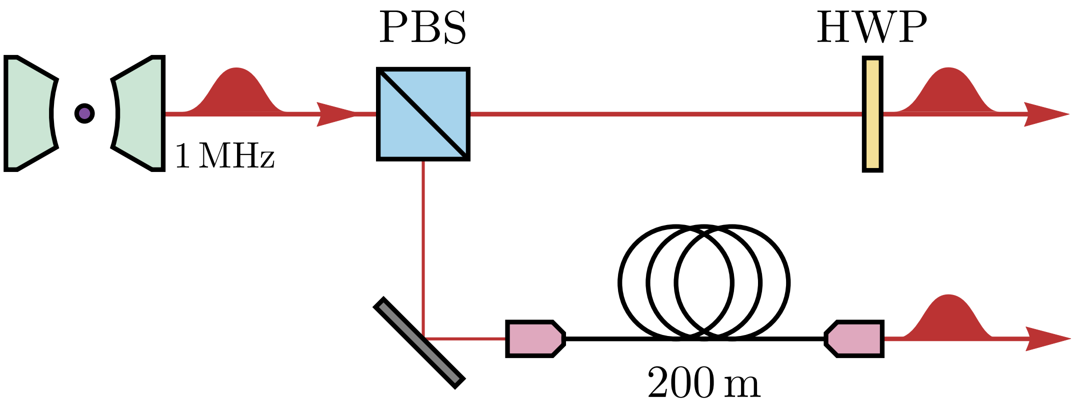

Figure 3.8: The routing of a stream of photons with random polarisations is probabilistic, with a 25% probability of two photons arriving at the input ports of a PBS. After the PBS, both photons are polarised, and their polarisations can be made to coincide by using a HWP. A fibre delay line is used to ensure that the early-emitted photon is able to arrive at the same time as the late-emitted photon.

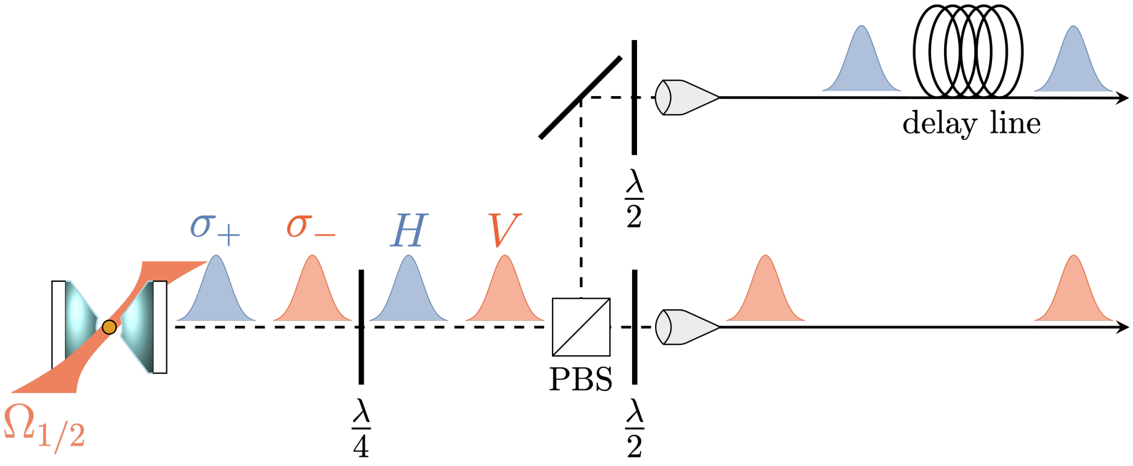

Figure 3.9: This figure shows the deterministic routing of a stream of polarised σ^+ and σ^- photons. A quarter-wave plate transforms these photons to the linear H and V polarisations. Using a PBS, both photons can be routed into different optical paths, one of which has an additional optical fibre delay line with an optical path time equal to the duty cycle of photon production. Wit this, it is possible to make two photons arrive simultaneously at the input ports of a beam splitter, something necessary for two-photon interference. This figure is taken from [63].

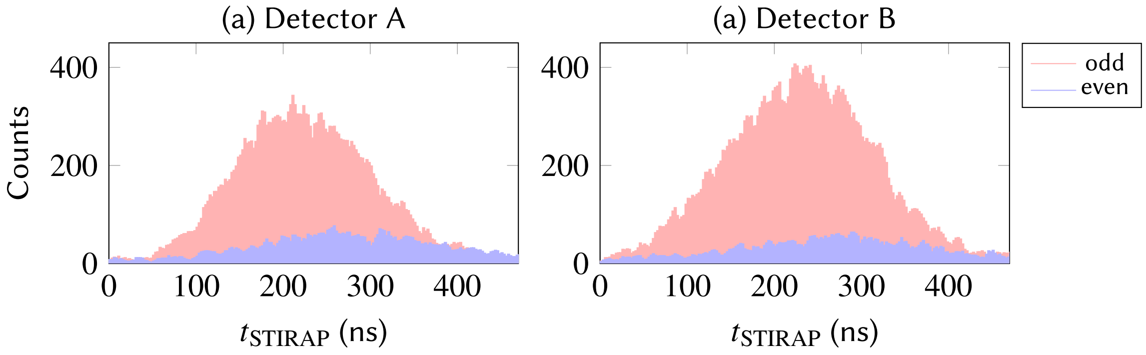

Figure 3.10: Photon wave packets sorted by pulse parity and polarisation. A sliding histogram with a bin width of 10 ns and a pitch of 2.5 ns is used. The photons of orthogonal polarisations are routed using wave plates, and a fibre delay of 134 m is used to delay photons of σ^- polarisation. The alternating polarisations of the emitted photons ensure that up to 86% of all detections are recorded in even pulse windows. The source for this data is [63].

"Quantum mechanics is very formidable. But an inner voice tells me that this is not yet the true Jacob. The theory provides a lot, but it hardly brings us any closer to the mystery of the old one. In any case, I'm convinced that He doesn't play dice."

— Albert Einstein, *1926, Letter to Max Born*

4

How to administer an antidote to Schrödinger's cat

The work presented in this chapter is adapted from the publication "*How to administer an antidote to Schrödinger's cat*", published in J. Phys. B **55**, 054001 (2022) [79].

4.1 Introduction

One of the most intriguing principles of quantum mechanics is that of superposition, which states that a quantum system, before being measured, can be interpreted to be in two simultaneous states at once. In his 1935 Gedankenexperiment [117], Erwin Schrödinger illustrated the paradoxical nature of superposition by depicting a cat in a box whose state (dead or alive) is entangled with a vicious device releasing a poisonous substance upon

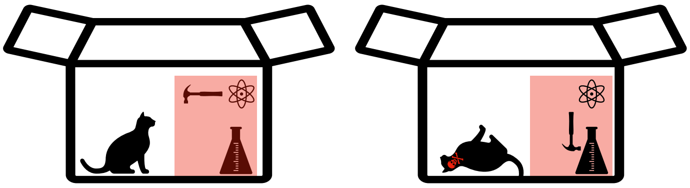

Figure 4.1: Depiction of Schrödinger's cat Gedankenexperiment. A cat is trapped in a box with a vicious device that releases a poisonous substance upon a radioactive decay with a probability of 50%. According to Schrödinger's analogy, it is only possible to know the state of the cat upon opening the box, something certainly not true for a macroscopic system like a cat.

a 50% probable radioactive decay, as shown in Fig. 4.1. Only upon opening the box for the first time, it is possible to determine the state of the combined system of the cat and the radioactive device, which will thereafter remain unchanged. Given the quantum superposition of both states of the cat, we can only expect it to be alive after half of the measurements.

The randomness of outcomes in quantum measurements distinguishes them fundamentally from classical measurements. The process of measurement in quantum mechanics has been central in theoretical physics, where the appearance of sharp measurement outcomes induces apparent contradictions on the predictions of quantum mechanics [118].

Since quantum measurements can be performed on the whole of a quantum system or on parts of it, this begs the question: can a partial measurement of a quantum system provide information to coerce the remainder of the system to collapse into a desired state?

Whether the system is macroscopic or not, feedback loops could be used and implemented to steer their states to a desired outcome: In the example of Schrödinger's cat, this can be translated to observing whether or not the poison has been released, as this normally determines the state of the cat. Given enough time between poisoning the cat and its actual death, performing such a partial measurement would provide the opportunity to administer an otherwise deadly antidote to a poisoned cat, such that it is always found alive. Such an approach would normally be implemented in the form of a feedback loop, by which a device obtains information about the trajectory of a physical system in order to modify it in real time [119, 120].

In quantum systems, feedback can be of two types: the first, measurement-based, occurs when a measurement outcome is re-directed to the original system. The second, coherent quantum feedback, involves no measurements but provides control using a coherent interaction with an auxiliary quantum system.

Both feedback types exist in a range of applications: the generation of amplitude squeezed states in a semiconductor laser [121] , the improvement of single-shot phase measurements in quantum metrology [122], the stabilisation of a combined atom-cavity quantum state [123], and the preparation and stabilisation of Fock states in a high-Q microwave cavity with weak measurements [124].

In the previous chapter, we have examined the figures of merit relative to the singleness of a single-photon source. This chapter will examine how the interference of two photons, in particular the Hong-Ou-Mandel effect, is used to measure the interference of photon pairs incident on the input ports of a 50:50 beam splitter. The results of two-photon interference experiments provide valuable insights about the coherence of the generated photons. Moreover, the long coherence lengths of the photons used allow us to use a feedback protocol to deliver a photonic state with a desired property: that of always exiting through the same output port of a beam splitter.

The usage of an atomic source combined with vSTIRAP produces photons with coherence times significantly longer than the time it takes for a signal to travel from the detector to the source. As a consequence, the time span between the first and second photon detection is long enough for a phase change to be applied on the second photon, still under production. The feedback enables the alternation between a bosonic and a fermionic-like interference in photons that controls the routing of a single photon as desired.

This chapter is structured as follows: In section 4.2, we explain the theory behind the interference of two photons arriving on the two input ports of a beam splitter. This opens the door to the explanation of the feedback experiment introduced here, which is done in section 4.3. Finally, we present the experimental results from this experiment and examine some of its physical consequences in section 4.6.

4.2 Theory of two-photon interference

As mentioned in the previous chapter, we will now examine the theory of two-photon interference, used for characterizing the quantum nature of a single-photon source using the interference of two photons emitted by it, arriving at the two input ports of a beam splitter.

The phenomenon of two-photon interference was originally demonstrated in 1987 [125], when two indistinguishable photons entered a 50:50 beam splitter and bunched, only leaving the beam splitter through the same output port. This is studied in detail in subsection 4.2.1. After this, subsection 4.2.2 explains the role of two-photon interference when the duration of the photons emitted by a single-photon source is much larger than the resolution of the detectors.

4.2.1 Hong-Ou-Mandel (HOM) effect

If, as shown in Fig. 4.2, the two input modes of a 50:50 beam splitter, labeled A and B, are split evenly across its two output modes, labeled C and D, the creation and annihilation operators for single photons in the input and output modes of the beam splitter are connected via a unitary operation that maps them. The mathematical form of this operation is

$$\hat{a}^{\dagger} = \frac{1}{\sqrt{2}}\left(\hat{c}^{\dagger} + \hat{d}^{\dagger}\right), \quad \hat{b}^{\dagger} = \frac{1}{\sqrt{2}}\left(\hat{c}^{\dagger} - \hat{d}^{\dagger}\right). \tag{4.1}$$

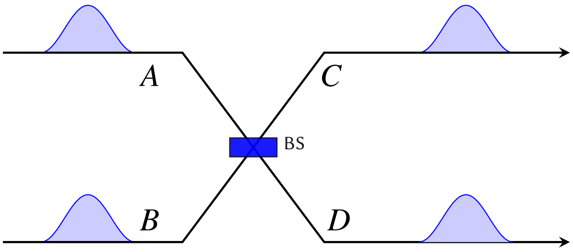

Figure 4.2: This figure summarises the arrangement of input and output modes for a Hong-Ou-Mandel interference setup.

If two single photons are sent simultaneously through the input ports of a beam splitter, two of the output states interfere in such a way that both photons bunch, i.e., they leave through the same beam splitter output port:

$$\begin{aligned}|\Psi_{\text{out}}\rangle &= \hat{a}^\dagger \hat{b}^\dagger |0\rangle \\ &= \frac{1}{2}\left(\hat{c}^\dagger + \hat{d}^\dagger\right)\left(\hat{c}^\dagger - \hat{d}^\dagger\right)|0\rangle \\ &= \frac{1}{2}\left(\left(\hat{c}^\dagger\right)^2 \cancel{- \hat{c}^\dagger \hat{d}^\dagger + \hat{d}^\dagger \hat{c}^\dagger} - \left(\hat{d}^\dagger\right)^2\right)|0\rangle\end{aligned} \tag{4.2}$$

$$= \left(|2_C 0_D\rangle - |0_C 2_D\rangle\right). \tag{4.3}$$

For Hong-Ou-Mandel interference to happen, both photons must be absolutely indistinguishable between each other, enabling the destructive interference of the intermediate terms. One way of introducing this distinguishability is to change the arrival time of one of the photons. When both photons arrive at the same time, the joint detection probability in detectors C and D is zero, only increasing as the arrival time increases [125]. This is customarily known as the Hong-Ou-Mandel dip, and it provides a way of quantifying the distinguishability between two photons emitted by the same source, in a similar way to how the $g^{(2)}$ function quantifies the singleness of photons emitted by a source.

A possible way of exploring the indistinguishability of photons which have not been emitted sequentially would be to circulate the output of a single-photon source through a ring resonator[126]: a ring resonator can be interpreted to be a set of multiple delay lines which could be used for interfering several photons separated spatially by the length of the resonator. This has not been examined further in this work.

4.2.2 Time-resolved two-photon interference

The effect examined above is not temporally resolved, as the measurement of Hong-Ou-Mandel dips reports the number of coincidence counts in a given coincidence time window that is larger than the temporal extent of a single photon. Nevertheless, the previous chapter has illustrated that single photon arrival times from our source occur on the order of several hundreds of nanoseconds, while single-photon detectors have resolutions on the order of picoseconds.

As a consequence, it is useful to describe the phenomena of two-photon interference considering the temporal extent of the photon. This treatment follows closely the results presented in [76, 77].

The temporal dependence of the electric field operator at the detectors can be written as the sum of spatio-temporal functions in distinct modes k, $\zeta_k\left(t\right) = \epsilon_k\left(t\right)\exp\left(-i\phi_k\left(t\right)\right)$:

$$\hat{E}^{+}(t) = \sum_k \zeta_k(t)\hat{k}, \quad \hat{E}^{-}(t) = \sum_k \zeta_k^{*}(t)\hat{k}^{\dagger}, \tag{4.4}$$

where $\epsilon_k\left(t\right)$ corresponds to the photon amplitude in mode k and $\phi_k\left(t\right)$ to its phase. Here, $\hat{k}$ and $\hat{k}^{\dagger}$ are the annihilation and creation operator of single photons in the temporal mode k. Under this formalism, the probability of measuring a photon in mode k at a time t is given by

$$P_i(t) = \langle 1_k|\,\hat{E}^{-}(t)\hat{E}^{+}(t)\,|1_k\rangle = \left|\hat{E}^{+}\left(t\right)\hat{k}^{\dagger}\left|0\right\rangle\right|^2 = \left|\varepsilon_k(t)\right|^2. \tag{4.5}$$

Let us now consider two photons arriving simultaneously at the input ports A and B of a beam splitter (BS), as illustrated in Fig. 4.2.1. In a similar way to Eq. 4.5, the joint probability of both photons arriving at times t_0 and $t_0 + \tau$ at detectors placed at outputs C and D of the BS, respectively, can be written as [77, 127]

$$P_{\text{joint}}\left(t_0, \tau\right) = \left|\hat{E}_D^{+}\left(t_0 + \tau\right)\hat{E}_C^{+}\left(t_0\right)\hat{a}^{\dagger}\hat{b}^{\dagger}\left|\tilde{0}\right\rangle\right|^2, \tag{4.6}$$

where $\hat{a}^{\dagger}$ and $\hat{b}^{\dagger}$ correspond to the creation operators of a photon in the ports A and B, and $\hat{E}_C^{\pm}$ and $\hat{E}_D^{\pm}$ are the electric field operators at the output ports of the beam splitter. In this context, τ can be positive or negative, and $\tau < 0$ corresponds to the detector in port D clicking before that in port C.

We emphasise that τ is a detection time difference giving rise to a time-resolved Hong-Ou-Mandel (HOM) signal [77, 127] , and must not be confused with the photon arrival time difference (Δt) used in many other HOM experiments [125]. Here, we are only interested in the case for which the two photon wave packets arrive simultaneously ($\Delta t = 0$).

Since the detection of a photon can occur at any given time, it is possible to calculate the joint detection probability as a function of the delay between each photon arrival, disregarding the absolute detection times:

$$P_{\text{joint}}\left(\tau\right) = \int_{-\infty}^{\infty} dt_0 P_{\text{joint}}\left(t_0, \tau\right). \tag{4.7}$$

For two linearly polarised photons with a relative polarisation angle θ, Eq. 4.6 can be written as [77]

$$P_{\text{joint}}\left(t_0, \tau\right) = P_{\text{joint}}^{(HV)}\left(t_0, \tau\right) - \cos^2\theta \; F\left(t_0, \tau\right), \tag{4.8}$$

where

$$P_{\text{joint}}^{(HV)}\left(t_0, \tau\right) = \frac{1}{4}\left(\left|\epsilon_A\left(t_0\right)\epsilon_B\left(t_0+\tau\right)\right|^2 + \left|\epsilon_A\left(t_0+\tau\right)\epsilon_B\left(t_0\right)\right|^2\right) \tag{4.9}$$

and

$$F\left(t_0, \tau\right) = \frac{\epsilon_A\left(t_0\right)\epsilon_B\left(t_0+\tau\right)\epsilon_A\left(t_0+\tau\right)\epsilon_B\left(t_0\right)}{2} \times \cos\left(\phi_A\left(t_0\right) - \phi_A\left(t_0+\tau\right) + \phi_B\left(t_0+\tau\right) - \phi_B\left(t_0\right)\right). \tag{4.10}$$

When both input photons have orthogonal polarisations ($\theta = \pi/2$), $P_{\text{joint}}\left(\tau\right)$ can be written as the convolution of their spatio-temporal squared amplitudes,

$$P_{\text{joint}}\left(\tau\right) = \frac{1}{2}\left(\left|\varepsilon_A\right|^2 * \left|\varepsilon_B\right|^2\right)\left(\tau\right), \tag{4.11}$$

rendering the choice of ϕ_A and ϕ_B irrelevant. This is in sharp contrast to the case for which both input photons have parallel polarisations ($\theta = 0$). The expected behaviour of $P_{\text{joint}}\left(\tau\right)$ for the particular case of two photons of perpendicular polarisation with temporal shape $\epsilon\left(t\right) = \sin^2\left(2\pi t/\delta t\right)$, is shown as a solid, dark curve in Fig. 4.8(a) for $\delta t = 400$ ns. The three peaks that are shown in Fig. 4.8(a) correspond to the detection of coincidences in detectors C and D delayed by varying time differences $\tau \in \left[-400, 400\right]$ ns.

We subdivide the overall duration of the photons into two distinct intervals (bins) of equal length labeled I_1 (early) and I_2 (late). Additionally, let us assume that, for the photon arriving through A, $\phi_A\left(t\right) = 0$ for all times, and that, for the photon arriving through B,

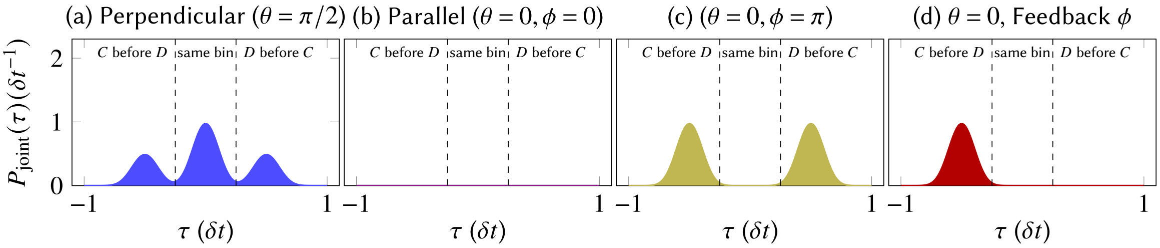

Figure 4.3: Theoretical curves for $P_{\text{joint}}(\tau)$ for the cases of orthogonal polarisation (a), identical photons ($\phi = 0$,b), $\phi = \pi$ (c) and Feedback (d).

$\phi_B(t) = 0$ for $t \in I_1$, and $\phi_B(t) = \phi$ for $t \in I_2$. In the Schrödinger picture, the temporal evolution is gathered in the quantum states [77] and the state entering the BS is given by

$$|\Psi_{\text{in}}\rangle = \frac{1}{2}\left(\hat{a}_1^\dagger + \hat{a}_2^\dagger\right)\left(\hat{b}_1^\dagger + \mathrm{e}^{i\phi}\hat{b}_2^\dagger\right)|0\rangle\,, \tag{4.12}$$

where $\hat{a}_j^\dagger$ and $\hat{b}_j^\dagger$ correspond to the photon creation operators in ports A and B in the time intervals I_j, with $j \in \{1,2\}$, and $|0\rangle$ is the vacuum state in the basis of all the temporal and beam splitter input paths: $|0\rangle = |0_{A1}0_{A2}0_{B1}0_{B2}\rangle$. For the cases $\phi = 0$ and $\phi = \pi$, the theoretical predictions of $P_{\text{joint}}(\tau)$ are shown as dashed curves in Figs. 4.3(b) and (c). For the case of Fig. 4.3(b), both input photons are identical and feature photon bunching in the output detectors. For this reason, the expected behaviour would not include any coincidences between detectors C and D. In contrast, in Fig. 4.3(c) the photon entering through port B acquired a π-phase change from I_1 to I_2. This is the only difference between the two photons. Therefore, if both photons are detected during either I_1 or I_2, the photons are indistinguishable and no correlations are found with $\tau \simeq 0$. However, if the photons are detected in different intervals, the change in phase drives them to different outputs, resulting in a coincidence probability that is twice as large as the orthogonal polarisation case for $\tau = \pm 200$ ns.

Figs. 4.3(b) and (c) exhibit a form that corresponds to a different type of interference between the two photons depending on the value of ϕ. Bosonic ($\phi = 0$) and fermionic interference ($\phi = \pi$) is found with photons either bunching in the same outputs or avoiding each other's outputs and giving rise to coincidences. To see this, consider the following argument, using the Schrödinger picture: the operators after the beam splitter in the output channels C and D in I_j are linked to those before it by the standard unitary relation $\hat{a}_j^\dagger, \hat{b}_j^\dagger = \left(\hat{c}_j^\dagger \pm \hat{d}_j^\dagger\right)/\sqrt{2}$. Therefore, after the beam splitter, Eq. 4.12 results in:

$$
\begin{aligned}
|\Psi_{\text{out}}\rangle = \frac{1}{2\sqrt{2}} \Big(&\left(\hat{c}_1^\dagger \hat{c}_1^\dagger + \mathrm{e}^{i\phi} \hat{c}_2^\dagger \hat{c}_2^\dagger - \hat{d}_1^\dagger \hat{d}_1^\dagger - \mathrm{e}^{i\phi} \hat{d}_2^\dagger \hat{d}_2^\dagger\right) \\
&+ \left(\mathrm{e}^{i\phi} + 1\right) \left(\hat{c}_1^\dagger \hat{c}_2^\dagger - \hat{d}_1^\dagger \hat{d}_2^\dagger\right) + \left(\mathrm{e}^{i\phi} - 1\right) \left(\hat{c}_2^\dagger \hat{d}_1^\dagger - \hat{c}_1^\dagger \hat{d}_2^\dagger\right) \Big) \left|\tilde{0}\right\rangle . \qquad (4.13)
\end{aligned}
$$

Here, $\left|\tilde{0}\right\rangle$ is the vacuum state in the basis of all the output ports and temporal modes: $\left|\tilde{0}\right\rangle = |0_{C1} 0_{C2} 0_{D1} 0_{D2}\rangle$. The first four terms account for both photons arriving at the same detector in the same time bin. These terms lead to the standard boson bunching reported in the standard HOM effect mentioned in the previous subsection.

The last four terms correspond to cross-correlations between detectors and/or time bins. Unless the single-photon detectors are number resolving, it is not possible to measure outcomes where both detections occur at the same detector in the same time interval, which correspond in operator form to those terms of the form $c_i^\dagger c_i^\dagger$ and $d_i^\dagger d_i^\dagger$, where $i \in \{1, 2\}$. These terms correspond to the canonical HOM effect, where both photons arrive at the same detector on the same time interval. Restricted to arrivals in different intervals, it is possible to eliminate these terms and rearrange the output state. As a consequence, the observable sub-state from Eq. 4.13 becomes

$$
\begin{aligned}
\left|\tilde{\Psi}_{\text{out}}\right\rangle = \frac{1}{2\sqrt{2}} \Big(&\hat{c}_1^\dagger \left(\left(e^{i\phi} + 1\right) \hat{c}_2^\dagger - \left(e^{i\phi} - 1\right) \hat{d}_2^\dagger\right) \\
&+ \hat{d}_1^\dagger \left(\left(e^{i\phi} - 1\right) \hat{c}_2^\dagger - \left(e^{i\phi} + 1\right) \hat{d}_2^\dagger\right) \Big) \left|\tilde{0}\right\rangle . \qquad (4.14)
\end{aligned}
$$

In this sub-state, the phase appears explicitly. By setting $\phi = 0$, Eq. 4.14 reads

$$
\left|\tilde{\Psi}_{\text{out}}^{(\phi=0)}\right\rangle = \frac{1}{2\sqrt{2}} \left(\hat{c}_1^\dagger \hat{c}_2^\dagger - \hat{d}_1^\dagger \hat{d}_2^\dagger\right) \left|\tilde{0}\right\rangle . \qquad (4.15)
$$

This state again leads to the canonical HOM effect, yet across the time bins this time. Therefore, both photons arrive at the same detector, but in separate time intervals. In this sense, photons behave as bosons in the detector mode, despite arriving at separate time intervals.

In contrast, setting $\phi = \pi$, Eq. 4.14 now gives

$$\left|\tilde{\Psi}_{\text{out}}^{(\phi=\pi)}\right\rangle = \frac{1}{2\sqrt{2}} \left(\hat{c}_1^\dagger \hat{d}_2^\dagger - \hat{d}_1^\dagger \hat{c}_2^\dagger\right) |\tilde{0}\rangle , \tag{4.16}$$

which is strikingly different to Eq. 4.15. The photons arrive to different detectors, and in this sense one can assign a fermionic behaviour to them. However, as for Eq. 4.15, the photons arrive at different time intervals.

Switching between the bosonic and fermionic behaviour by choosing ϕ allows one to put the system into a pre-defined quantum state conditioned on the random outcome of the first measurement. This is implemented in the form of a feedback mechanism, where a photon detection at either detector in I_1 reveals the required change of ϕ to steer the remaining photon in I_2 to a specific detector. For instance, if detector D clicks in I_1, the second detection would normally occur in detector D, due to the canonical HOM effect. However, as the second halves of the photons have not reached the input ports at the moment of detection, we can use a detector click to change the phase between I_1 and I_2 for one of the incoming photons at the time that defines the intervals. As a consequence, we can change the port in which the second detection occurs. By choosing $\phi = \pi$ and projecting the output state in Eq. 4.16 onto the measured state $|0_{C1} 1_{D1}\rangle = \hat{d}_1^\dagger |0_{C1} 0_{D1}\rangle$ (involving only the first time bin, since the second one has not yet occurred), the state reduces to

$$\left\langle 0_{C1} 0_{D1} \middle| \hat{d}_1 \middle| \tilde{\Psi}_{\text{out}}^{(\phi=\pi)} \right\rangle = \frac{1}{\sqrt{2}} \hat{c}_2^\dagger |0_{C2} 0_{D2}\rangle . \tag{4.17}$$

This state clearly shows that, when a measurement occurs in I_2, any click will be recorded in detector C. Analogously, if detector C clicks in I_1 and $\phi = 0$ is chosen, both photons are identical in their two halves and any detection in I_2 will always occur at detector C. This reduces the quantum state to

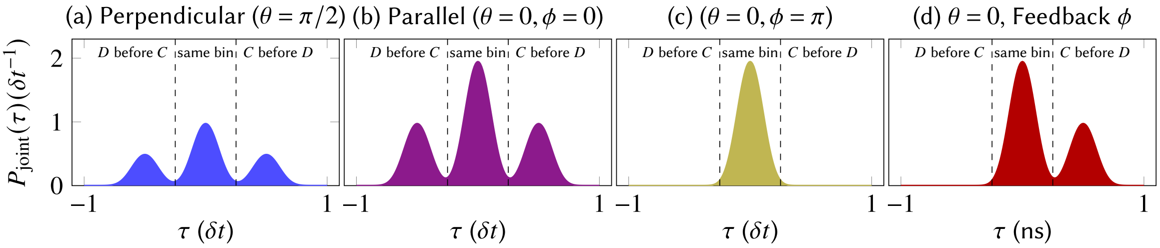

Figure 4.4: Theoretical curves for $P_{\text{same}}(\tau)$ for the cases of orthogonal polarisation (a), identical photons ($\phi = 0$,(b)), $\phi = \pi$ (c) and Feedback (d). Subfigure (b) shows that, when photons are identical, all the detections happen in the same detector, albeit possibly in different time bins.

$$\left\langle 0_{C1}0_{D1}\right|\hat{c}_1\left|\tilde{\Psi}^{(\phi=0)}_{\text{out}}\right\rangle = \frac{1}{\sqrt{2}}\hat{c}_2^{\dagger}\left|0_{C2}0_{D2}\right\rangle. \tag{4.18}$$

Again, when a measurement occurs in I_2, any click will be recorded by detector C. Eqs. 4.17 and 4.18 imply that ϕ can be used as a parameter for feedback control, to steer the remaining photon to a desired output.

Returning to the Heisenberg picture and following Eqs. (4.7) and (4.8) with a value of ϕ conditional on the measurement of a photon in I_1, we observe the expected behaviour of $P_{\text{joint}}(\tau)$, as illustrated in Fig. 4.3(d). Fig. 4.3(d) shows increased coincidences with $\tau < 0$, for which a detection in D occurs before a detection in C. There are significantly less coincidences with $\tau > 0$, as this would correspond to detector C firing first and detector D second, which cannot occur with an active feedback that always prompts the second detection in C. Fig. 4.3 shows the subset of probabilities for cross-detector correlations only. For this reason, the value $\int P_{\text{joint}}(\tau)\,d\tau$ is bounded by $1/2$. A prediction of the theoretical curves for same-detector correlations, given by $P_{\text{same}}(\tau)$ can be shown in Fig. 4.4. Given the different possibilities that can arise from photon routing, the normalisation for the joint detection probability is given by

$$\int \left(P_{\text{joint}}(\tau) + P_{\text{same}}(\tau)\right) d\tau = 1. \tag{4.19}$$

With this, knowing the value of $P_{\text{joint}}(\tau)$, it is possible to find the value of $P_{\text{same}}(\tau)$.

4.3 Feedback experiment

Using the methods of chapter 3 for the unpolarised source, the atom-cavity system is initially prepared in $|F=2,0\rangle$. The laser adiabatically drives the system to $|F=1,1\rangle$, whereupon the photon is emitted from the cavity mode, leaving the system in $|F=1,0\rangle$, decoupled from further evolution.

The driving laser is used to generate double-humped photons, whose phase is controlled using a separate, fast electro-optic modulator (EOM), that directly maps the phase of the laser to the emitted photon. The photons have a total duration of $\delta t = 450$ ns, evenly distributed in two intervals of 225 ns. By applying an external voltage, the phase of the laser can be alternated between 0 and π and characterized using a fibreised Mach-Zehnder interferometer to determine the voltage applied that generates the desired phase shift.

After being emitted from the source, the photons, which have random polarisations, are randomly routed into the output ports of a PBS, as described in Section 3.10.2.1. In 25% of the occasions, the early-emitted photon is sent through a 300 m fibre, while the late-emitted photon is sent directly through a shorter fibre of 1.5 m, ensuring that both wave packets arrive simultaneously at the input ports of a beam splitter. Both photons emerge polarised after the PBS, and a HWP can be used to control the relative polarisation of both photons, ranging from parallel to orthogonal polarisations.

The first halves of the two interfering photons span 67.5 m ($\sim$ 225 ns), despite the optical path length between the cavity and the detectors being only 1.5 m or 301.5 m, depending on whether the photon has taken the direct route to the detector or has been delayed with an optical fibre. We only restrict ourselves to the cases where we obtain two photons arriving at the same time at the detector. As a consequence, the photon going through the short path is always the one emitted later. This means that the first time interval of the two photon state is already being measured before the second half of the second photon leaving the cavity (travelling along the shorter path) has been fully generated. The length of the interfering photons is sufficient for a feedback loop to alter the phase ϕ of the second half of the photon under production, conditioned on the measurement outcome within the first time interval (Fig. 4.5.)

4.3.1 Implementation of feedback

The feedback is implemented using a home-built circuit controller and single-photon counting modules (SPCMs) with a quantum efficiency of 60-65% and a resolution of < 300 ps (Excelitas SPCM-AQRH-780-14-FC). The total feedback loop latency, from the EOM via the cavity to the SPCM, then back to the EOM via the controller circuitry is 97.0 ± 0.2 ns. Therefore, a conditioned phase change cannot be realised in time if a photon detection in I_2 occurs less than 97 ns after a detection in I_1. The resulting error rate is limited to 0.2% for a $\sin^2(t)$ photon amplitude envelope. All photon counts are recorded with 81ps accuracy using a qutools quTAU time-to-digital converter (TDC). Detections within the 450 ns photon window are further processed for a dark count correction for each SPCM. We now turn to a detailed description on the error rates, time budgets and the implementation of the logical feedback circuit.

4.4 Latency of feedback

To ensure adequate feedback, it is crucial to perform a timely change on the phase ϕ, conditional on detections only in the first time bin. However, not every detection of the SPCM can be used to change the phase of the photon: the latency between the SPCM click and the effect of the feedback electronics can affect the production of a proper photonic state which can be used for feedback. As mentioned before, the photon signal takes around 75 ns to reach the output of the SPCMs from the EOM, during which there is no possibility of achieving feedback control.

The probability of a correlation (with one detection in each time bin) occurring during the dead time is given by

$$P(\tilde{t}) = \int_{\max\left[\frac{1}{2}-\tilde{t},0\right]\delta t}^{\frac{1}{2}} \varepsilon(t_1) \int_{\frac{1}{2}}^{\min[t_1+\tilde{t},1]\delta t} \varepsilon(t_2)\, \mathrm{d}t_2\, \mathrm{d}t_1 \tag{4.20}$$

where $\tilde{t}$ is the dead time given as a fraction of the total photon length δt, $t_1 \in \left(0, \frac{1}{2}\right)\delta t$ and

Element	Time (ns)
Optical Transit Time EOM → Cavity → SPCM	45
SPCM Response	35
Circuit Response	7.0
Signal Rise Time	5.5
Total Cable Delay SPCM → Control → EOM	4.5
Total	97.0

Table 4.1: A breakdown of the contributing elements to the feedback delay. The first two rows are not known absolutely, only their sum was measured. From discussions with the manufacturer it is believed that the SPCM response (time delay between photon impact and TTL output) is around 35 ns.

$t_2 \in \left(\frac{1}{2}, 1\right)\delta t$, and $\varepsilon(t)$ is the normalised intensity envelope of the photons,

$$\varepsilon(t) = \frac{16}{3}\sin^4(2\pi t/\delta t) \tag{4.21}$$

The error rate remains extremely small for dead times of up to around a fifth of the total photon length before increasing rapidly, as shown in Fig. 4.6. In our experiment, the control and effecting stages are implemented in 13ns, resulting in a total latency for the feedback of 97ns, corresponding to an expected error rate of 0.2%. Table 4.1 details the latency breakdown.

4.5 Fast electronics

The task of the feedback controller is to decide whether or not a phase should be applied to the second time bin and, if so, quickly supply sufficient voltage to the electro-optic modulator to enact that phase change. To that end, a custom in-house circuit was built using off the shelf transistor-transistor logic (TTL) integrated circuit (IC) logic chips. The circuit toggles between one mode of operation with no effect and another one which ensures a phase change to the EOM during the second time bin. An abbreviated circuit logic diagram outlining the functioning of the circuit is shown in Figure 4.7. The control circuit receives as inputs a copy of the TTL output from the SPCM of interest, det, and two 215 ns TTL window pulses from the AWG, $\mathrm{W}_{\mathrm{det}}$ and $\mathrm{W}_{\mathrm{phase}}$, which respectively outline the first time bin for the registering of detections and the second time bin for the output phase voltage, phase.

4.6 Results and discussion

There are two different ways to look at the measured data. One has been discussed previously and corresponds to Fig. 4.8, which shows the coincidence probability as a function of the time-difference between two detections. However, our main interest is whether both detections are registered within the same or opposite time intervals (I_1 and I_2). Therefore, the same data can be represented in a cross-correlation diagram (Fig. 4.9) showing the four possible values of the coincidence probability between detectors C and D firing in either I_1 or I_2. In contrast to Fig. 3, this allows to further differentiate between coinciding detections in I_1 and I_2.

The cross detection probability of interfering photons with perpendicular polarisations is shown in Fig. 4.8(a). This gives rise to the random routing of the simultaneously arriving photons, such that the resulting time-resolved coincidence rate yields the autocorrelation function of the photons' intensity profile. The cross-correlations are depicted in Fig. 4.9(a). For the case of photons with orthogonal polarisations, these are identical and theoretically equal to $1/8$.

For photons with parallel polarisations, the cross correlation probability is shown in Fig. 4.8(b) for $\phi = 0$. This measurement follows the predictions of photon bunching in the canonical HOM effect, for which we expect no coincidences. Photons bunch in the same output regardless of the actual detection time. Thus, the probability of cross channel detections is expected to be zero for all time differences (Fig. 4.9(b)).

Fig. 4.8(c) shows the cross detection probability for photons with parallel polarisations when $\phi = \pi$. In this case, the photons anti-bunch (i.e., they are found in different output channels if detected in different time intervals). The maximum probability to find photon-photon correlations occurs at $\tau = \pm\delta t$, where δt is the length of the photons. This maximum probability is twice the reference value of Fig. 4.8(a), which is in accordance with the cross-channel detections shown in Fig 4.9(c). Nonetheless, the likelihood of correlated photon detections in the same time interval is close to its theoretical value of zero.

Finally, the cross detection probability shown in Fig. 4.8(d) represents the case of active feedback on ϕ, for which we expect any photon recorded in I_2 be detected at C. Therefore, the number of "D before C" correlations reaches a maximum while we barely see any "C before D" correlations, as shown in Fig. 4.9(d). Our experimental results demonstrate that classical feedback control of a quantum excitation spanning multiple systems (RF pulse driving AOM → driving laser → atom → cavity → quantum field modes) can be achieved, resulting in a photonic state with the property of always exiting through the same output of a beam splitter. Since the photonic excitation spans different systems, including the atom itself, it could be possible to understand the behaviour reported here in terms of the entangled state between the atom and the detected photon, but many other different devices are also entangled with this state, some of which are under full classical control.

Some differences between theoretical expectations and experimental results are visible in Figs. 4.8 and 4.9. These can be attributed to a partial loss of coherence or depolarisation of the interfering photons, most evident from the presence of correlations in the side lobes of Fig. 4.8 (b). The mutual coherence between photons is often characterised by the HOM visibility, defined as

$$V_{\text{HOM}} = 1 - \frac{N_{\|}}{N_{\perp}} \tag{4.22}$$

where $N_{\|}$ and $N_{\perp}$ are the total number of correlations observed for interfering photons with parallel and perpendicular polarisations, respectively. Using the results obtained with $\phi = 0$ for $N_{\|}$ we find $V_{\text{HOM}} = 0.78 \pm 0.04$. However, we measure a reduced visibility of $V_{\text{ref}} = 0.61 \pm 0.04$ if we restrict our analysis to those correlations with detections across time intervals I_1 and I_2. This serves as a reference for all effects discussed here, as these affect only the correlations across both time intervals.

The visibility under phase control upon switching between $\phi = 0$ and $\phi = \pi$ reads

$$V_{\phi} = \frac{N_{\pi} - N_0}{N_{\pi} + N_0}, \tag{4.23}$$

where N_0 and N_{π} represent the coincidence counts between pairs of photons with relative phase shifts of $\phi = 0$ and π, respectively. Again, we only count coincidences across I_1 and I_2, and find $V_\phi = 0.56 \pm 0.06$, in agreement with V_{ref} within error bars. This validates the robustness of the phase switch as no further loss of coherence is induced[1].

Since the feedback relies on a conditional phase switch, we quantify its visibility by comparing coincidence counts between intervals where a measurement in D occurs before one in C (N_{D1C2}), and vice-versa (N_{C1D2}):

$$V_{\text{feed}} = \frac{N_{D1C2} - N_{C1D2}}{N_{D1C2} + N_{C1D2}}. \tag{4.24}$$

For our experiment, we find $V_{\text{feed}} = 0.56 \pm 0.06$, which is identical to V_ϕ and equally within error bars of V_{ref}. We therefore conclude that the feedback works as expected, without introducing any loss of coherence.

4.7 Interpretation

Going back to the analogy between photon interference and cat-poison states, shown in Fig. 4.10, the goal of the feedback has been to break the correlation between them. Where before the system was characterised by the cat-poison state as

$$|\psi\rangle = \frac{1}{\sqrt{2}} \Big(|\text{alive}\rangle_{\text{cat}} |{\downarrow}\rangle_{\text{poison}} + |\text{dead}\rangle_{\text{cat}} |{\uparrow}\rangle_{\text{poison}} \Big), \tag{4.25}$$

a measurement on the state of the poison and the implemented feedback loop have enabled us to apply a phase change in the state of the system, ensuring that the cat is always measured alive.

In this experiment, it is possible to assign the state of the poison to that of the two-photon state in the first interval. A measurement of a broken poison corresponds to observing the first photon in detector C, i.e., $|{\downarrow}\rangle_{\text{poison}} = c_1^\dagger |\tilde{0}\rangle$, while a non-broken poison corresponds to observing the first photon in detector D, $|{\uparrow}\rangle_{\text{poison}} = d_1^\dagger |\tilde{0}\rangle$. In a similar way, the cat states correspond to $|\text{alive}\rangle_{\text{cat}} = c_2^\dagger |\tilde{0}\rangle$ and $|\text{dead}\rangle_{\text{cat}} = d_2^\dagger |\tilde{0}\rangle$.

---

[1] V_{ref} and V_ϕ are expected to yield the same value, assuming $N_{\parallel} = N_0$ and $N_{\perp} = (N_0 + N_\pi)/2$ due to the random splitting of photons.

In the system mentioned in this chapter, administering an antidote corresponds to applying a phase change from $\phi = 0$ to $\phi = \pi$ depending on the outcome of the measurement in the first interval. This enables us to change from $\left|\tilde{\Psi}_{\text{out}}^{(\phi=0)}\right\rangle$ to $\left|\tilde{\Psi}_{\text{out}}^{(\phi=\pi)}\right\rangle$, changing the distinguishability between the photons interfering and therefore its bunching nature, from bosonic to fermionic in the detectors.

A question that can arise naturally from this analogy is why the antidote is not administered to all of the cats. After all, in the usual analogy between cat and poison, an unbroken poison would always leave the cat unharmed. Similarity to the experiment is recovered when considering an antidote that can only work in combination with the poison, this is, one that could otherwise be deadly to the cat. A constant change of the phase of the system to $\phi = \pi$, even before the feedback has taken place, ensures that early detections in C (unbroken poisons) correspond to late detections in D (dead cats), something understandable from the fermionic nature of the interference.

Finally, a limited visibility in the feedback also has an interpretation in this system, as some phase changes (influenced by the poison state) do not lead to living cats. We have already explained that this loss of coherence is due to the distinguishability of the photons, something that is understandable given the large amount of noise sources present in the laboratory, including drifting magnetic fields and changing cavity couplings.

An important caveat must be remarked here: the states we consider in Eq. 4.25 could also be interpreted as Bell states, and the collapse of this superposition occurs successfully for microscopic, individual quantum objects such as a single photon. As such, the intepretation of this state is not appropriately described by what are customarily described in the literature as cat states, which are generally described as having the form $|\mathfrak{cat}\rangle = (|\alpha\rangle + |-\alpha\rangle)/\sqrt{2}$, for $|\alpha\rangle$ a coherent state of light. These states have been experimentally realised in the past in other research groups [128, 129], but the work here does not involve the implementation of any states of this form. Indeed, some of the ideas about the cat and antidote analogy presented here do not have an analogous interpretation in a conventional cat state: Since applying the antidote requires an action on the state of the cat prior to the beamsplitter, administering an antidote to a cat which behaves as a superposition of two macroscopically distinct states would not be possible.

Other differences are related to the time delay between the poison and the cat, which would place no role in the time delay between the two parts of the $|\mathfrak{cat}\rangle$ wavefunction. A final one has to do with the fact that, in this experiment, the atom in the cavity can be interpreted to play the role of a quantum memory for a single photon, something which could not be realized with a cat state.

4.8 Conclusions

We have demonstrated a technique for steering the measurement of a quantum superposition towards a definitive result. This was achieved by using a feedback mechanism that enforces either bosonic or fermionic behaviour on interfering photons with long coherence lengths.

We emphasise that a classical interpretation of the described experiment fails. Classically, one might expect the feedback control to be successful only when the first detection corresponds to the photon in the delay arm. Otherwise, if the first detection was of the photon in the short arm, the phase change of the driving laser would have no effect (as the photon under generation has already been detected). In a classical description, one would expect a random routing of the second photon regardless of the phase switch, and a reduction of the feedback visibility to zero, which is clearly not the case.

This result constitutes an elementary step towards introducing active control into processes such as quantum random walks and optical networks [130]. Generalisations of the technique demonstrated here are suitable candidates in photonic switchyards requiring multiple photon streams for studying multi-mode interferometry [27], where the deterministic routing of photons would be performed using feedback operations.

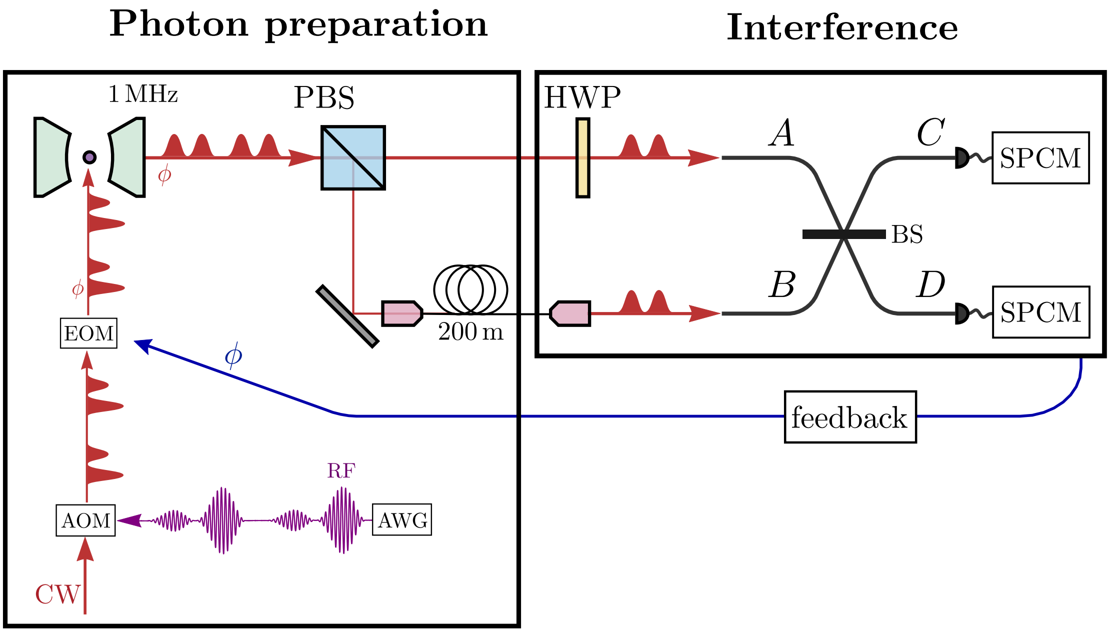

Figure 4.5: Experimental arrangement: Two long, double-hump photons interfere in a beam splitter. Photons are emitted at a repetition rate of 1 MHz from an atomic source driven by a laser pulse controlled by an acousto-optic modulator (AOM), whose phase is changed using an electro-optic modulator (EOM). The AOM pulses are generated by an arbitrary waveform generator (AWG). A delay line with an optical path length of 300 m ensures the simultaneous arrival of two sequentially emitted photons. The emitted photons have such long wave packets, that the first time bin of both photons interferes before the relative phase ϕ of the second photon in the second time bin is set. Furthermore, the emitted photons have random polarisations. Using a polarising beam splitter (PBS), photons are routed into random paths, and two photons simultaneously impinge on the input ports A and B of a beam splitter (BS) in 25% of all possible cases. The relative polarisation between both photons is changed using a half wave plate (HWP). Photons then interfere in the BS and exit through the ports C and D, upon which measurements are performed using single-photon counting modules (SPCMs). The outcome of a measurement in the first time bin is used to perform feedback on the value of the phase, ϕ during the second half of the driving pulse.

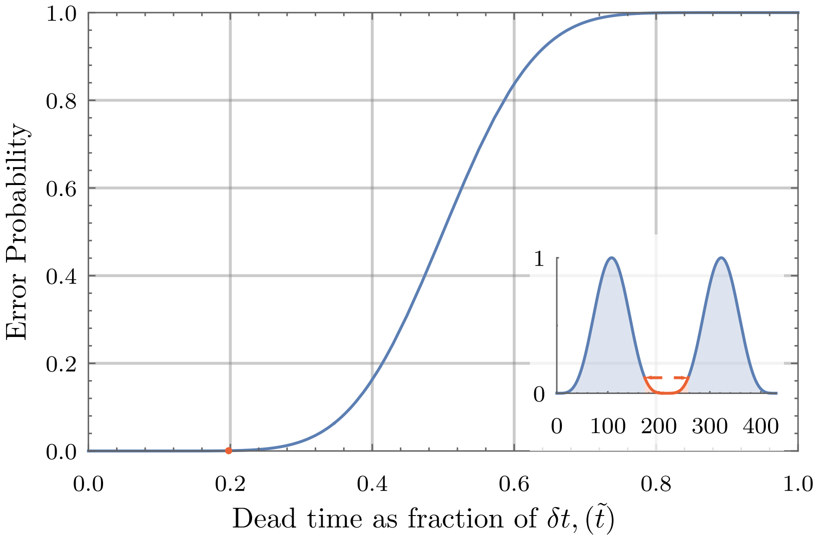

Figure 4.6: Analysis of feedback error induced by latency. The dead time is the feedback delay of the system, here shown as a fraction of the photon length. It corresponds to time taken for a signal to pass from the EOM to the cavity and the detectors, be processed by the controller and return to the EOM. During the dead time, the feedback control cannot be achieved. This introduces an error rate (Eq. 4.20). The profile of the considered photon is shown in the inset along, with a section highlighted in red corresponding to the measured 97 ns feedback delay of the setup. The error rate of 0.2% obtained for this delay is shown in the horizontal axis. This figure is taken from [64, 79]

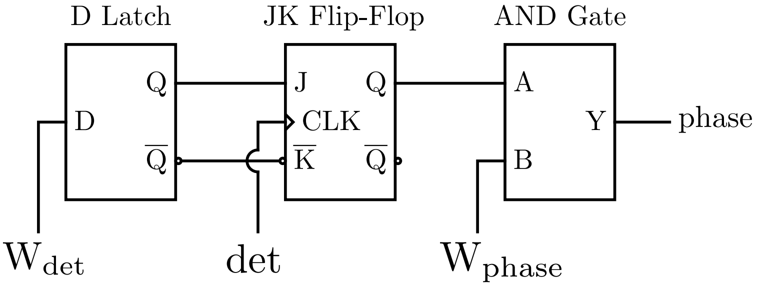

Figure 4.7: Control circuit: The JK flip-flop (Texas Instruments SN74F109N) controls the state of operation of the circuit. When Q is 0, no phase signal will be output, but when Q is 1, the output, phase, follows W_{phase}, using a wired AND gate with open collector TTL gates (N74F07N). Toggling between these two states is triggered by a signal on the JK flip-flop CLK (clock) input from a detector, det, but only when the JK is in toggle mode. With Q($\overline{Q}$) high (low) the JK is in toggle mode, with Q ($\overline{Q}$) low (high) the JK is in Hold mode. The D latch (TI SN74LS375N) buffers the input W_{det} to provide a duplicated and negated copy.

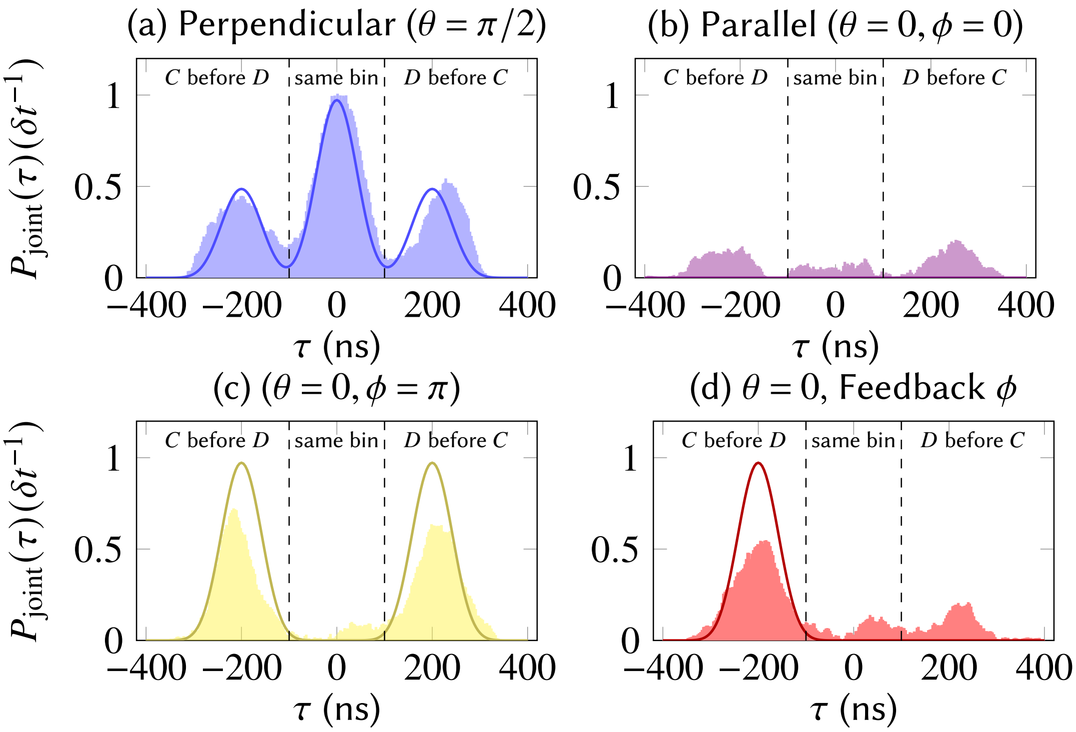

Figure 4.8: Coincidence probability densities and sliding histograms (whose bin width is larger than its bin separation) showing the theoretical (solid) and experimental (filled) values for $P_{\text{joint}}(\tau)$. This illustrates the time-resolved HOM interference of two photons under three different conditions. (a) shows the random routing of photons with perpendicular polarisations, which serves as reference. (b) shows the interference between indistinguishable photons ($\phi = 0$) with parallel polarisations, resulting in almost no coincidences between the two detectors. (c) shows the trace obtained for photons with phase shifts of $\phi = \pi$ without feedback. (d) shows the asymmetric pattern observed under feedback control, where the feedback has prevented (most) correlations in the right satellite peak. The data shown here has been corrected for correlations involving background noise, as explained in Chapter 3. The method of sliding histograms has been used to better represent the results, requiring fewer data than a usual histogram where each of the data points contributes only to a single bin. Only the cross-detector probabilities are shown, as the used detectors cannot count two photons on the same detector in the same time bin.

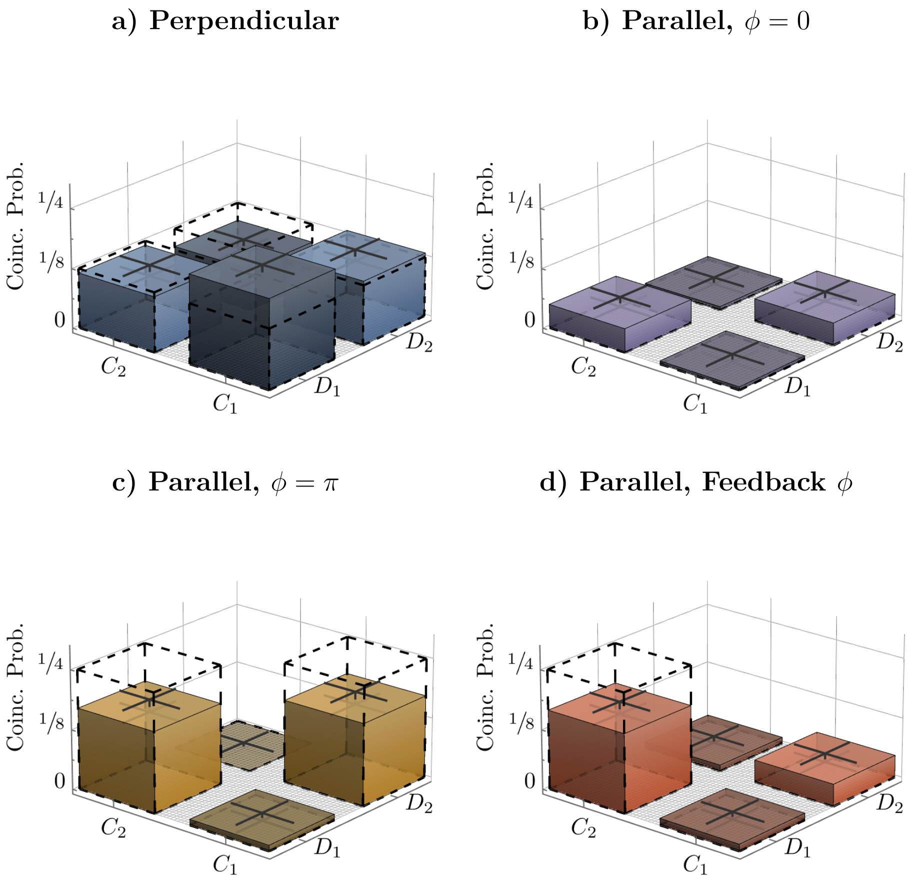

a) Perpendicular

b) Parallel, $\phi = 0$

c) Parallel, $\phi = \pi$

d) Parallel, Feedback ϕ

Figure 4.9: The correlations from Fig. 4.8 are now shown according to the exact detector-time-bin detections, demonstrating an increase in the correlations between C_2 and D_1 (implying that a detection in D in I_1 has been used to steer the measurement of a photon in I_2 to C). The limited visibility is evident when comparing the data to their theoretical values, shown dashed. The data shown here has been corrected for correlations involving background noise, as explained in Chapter 3.

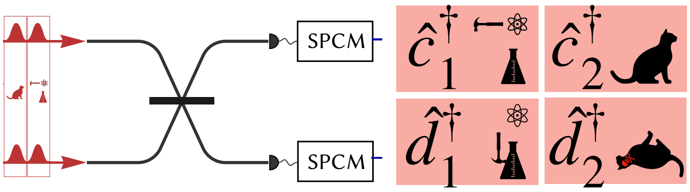

Figure 4.10: Interpretation of two-photon interference as a Schrödinger's cat experiment.

"To infinity and beyond!"

—Buzz Lightyear

5

Using atom-cavity based single-photon sources beyond two-photon interference

5.1 Introduction

In the previous chapters, we have explained several of the methods used for producing single photons using an atom inside of a high-finesse cavity. Our ideal goal would be to obtain N photons simultaneously arriving -ideally from different sources- in different input channels of a multimode interferometry chip: a device consisting of multiple input and output ports to generate unitary operations connecting them, as shown in Fig. 5.1. Interestingly, depending on the nature of the light arriving on the input ports, the resulting interference can generate quantum states that can be used for practical quantum-based applications, as has been mentioned in chapter 1.

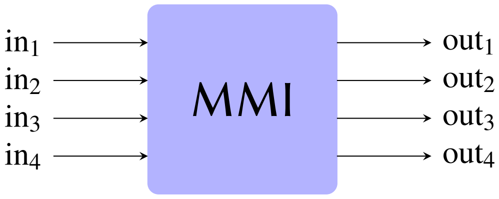

Figure 5.1: A multimode interferometer (MMI) is a device consisting of multiple input and output optical ports, which enables the generation of unitary operations linking them. When used in conjunction with long photons, an MMI can generate entangled photonic states useful for quantum applications [27].

We have shown how one of the implemented sources is able to produce photons of arbitrary wave-packets that do not have a defined polarisation. This source has enabled the characterisation of two-photon interference in a multimode interferometer [27] when the photon source has been combined with a polarising beam splitter and the use of delay lines equal to the temporal separation between two consecutive photons.

If the photons emitted from the atom-cavity based single-photon source do not have a defined polarisation after being emitted, placing a polarising beam splitter after the source only produces two photons simultaneously arriving at the output ports in 25% of the cases 4.

A remedy to overcome this post-selection has been to generate single photons of alternating polarisations [27], which have a natural routing when emitted towards a polarising beam splitter. Adding a delay line equal to the photon length and one half wave plate, the source can deliver two simultaneous photons of equal polarisations in different optical paths.

As mentioned before, to generate the aforementioned photons we apply a magnetic field to unfold the magnetic structure of the D_2 line of ^{87}Rb, generating detunings between the different m_F sublevels of the ground state. The photons emitted from the magnetic sub-level transitions are polarised, and the driving pulse can be tuned to be used as driving or repumping in an alternating manner between these transitions. The detunings between the levels must be large enough for the cavity to resolve the transitions and not address unwanted atomic states. Unfortunately, as mentioned in Section 2.7, this requires the usage of strong magnetic fields which place the light-matter interaction in an intermediate

Nonlinear Zeeman regime which does not allow for the faithful production of a stream of more than two sequential photons with high efficiency [54].

To overcome this, in this chapter we study several theoretical proposals to produce a stream of polarised single photons which is resilient to the nonlinearities induced by strong external magnetic fields. We then examine the devices used to make these photons arrive simultaneously at the input of a multimode interferometer, using a photon switchyard composed by free-space Pockels cells, beam splitters and fibre delay lines. Although no single photons have been routed by the switchyard, we characterise the switchyard using coherent light.

5.2 Improving the emission efficiency of polarised single photons

We seek for a process that minimises the impact of a photon emission as a prerequisite for the emission of the next. This can be achieved by not using the vSTIRAP pulse as a repumping pulse for the atom, but rather to rely on methods that repump the atom back to its initial desired state in a separate process before attempting the production of a subsequent photon. Moreover, since the efficiency of generating photons of alternating polarisation is hindered by a weaker coupling in one of the driving branches of the process, it would be desirable that the photons produced are all identical.

In what follows, we present two methods that overcome the detrimental consequences of nonlinear Zeeman effects for efficiently producing polarised single photons from an atom-cavity system. The first of these methods operates at the nonlinear Zeeman regime and is completely coherent, using two lasers deployed for a STIRAP re-pumping scheme, as shown in section 5.2.2. The second one does not require the usage of a magnetic field but relies on incoherent methods (and therefore on atomic spontaneous emission) to bring the atom back to its original state after several rounds of excitations, as shown in section 5.2.3.

5.2.1 How simulations are performed

The simulations in this chapter use similar methods to the ones used for predicting the behaviour of single photon production in the presence of strong magnetic fields [37, 63]. They make use of a full-fledged atomic structure to predict the behaviour and efficiency of the atomic system. By considering the atom-cavity system to span a basis of eigenstates $|i, n_1, n_2\rangle$, where i is the atomic state, and n_1 and n_2 correspond to the number of photons in the two orthogonal polarisations sustained by the cavity.

Since the operation of the system occurs at the single-photon level, we can consider the optical modes in the cavity to be two coupled two-level systems, with the photon number in each of the polarisations being either zero or one. The combined Hamiltonian describing the evolution of the system retains the form of the Jaynes-Cummings Hamiltonian described in section 2.4,

$$\hat{\mathcal{H}}_{\text{full}} = \hat{\mathcal{H}}_{\text{atom}} + \hat{\mathcal{H}}_{\text{cav}} + \hat{\mathcal{H}}_{\text{int}} , \tag{5.1}$$

where the atomic Hamiltonian is given by the populations of different energy levels $|i\rangle$, each one detuned by Δ_i from an energy level reference:

$$\hat{\mathcal{H}}_{\text{atom}} = \hbar \sum_i \Delta_i |i\rangle\langle i|. \tag{5.2}$$

In a similar fashion, the Hamiltonian for the cavity, which is detuned by Δ_C from the transition between $|F = 1, 0, 0\rangle$ and the energy level $|i\rangle$ with energy zero, is proportional to the total number of photons present in the cavity,

$$\hat{\mathcal{H}}_{\text{cav}} = \hbar \Delta_C \left(\hat{a}_1^\dagger \hat{a}_1 + \hat{a}_2^\dagger \hat{a}_2 \right). \tag{5.3}$$

Here, $\hat{a}_1^\dagger$ ($\hat{a}_1$) and $\hat{a}_2^\dagger$ ($\hat{a}_2$) correspond to the creation (annihilation) operators of photons in the orthogonal polarisation modes 1 and 2 of the cavity.

The interaction Hamiltonian shows how the atomic states $|i\rangle$ and $|j\rangle$ are coupled using a driving pulse with Rabi frequency $\Omega(t)$, and also ensures that the atom-cavity coupling factor g enables an atomic transition and the creation of a photon of polarisation 1 or 2 while following the selection rules. It has the form

$$\hat{\mathcal{H}}_{\text{int}} = -\hbar \sum_{i,j} \frac{1}{2} \left\{ A_{ij} \bar{\Omega}(t) (|j\rangle\langle i| + |i\rangle\langle j|) + A_{ij} \bar{g} \left(|j\rangle \left\langle i \middle| \hat{a}_{1/2} + \hat{a}^{\dagger}_{1/2} \middle| i \right\rangle \langle j| \right) \right\}, \tag{5.4}$$

where $\bar{g}$ and $\bar{\Omega}(t)$ are the atom-cavity coupling rate and Rabi frequency of the driving laser after factoring all the angular dependencies, which are themselves summarized in the coupling factor A_{ij}:

$$g = A_{ij} \bar{g}, \quad \Omega(t) = A_{ij} \bar{\Omega}(t). \tag{5.5}$$

This dynamics of the system are solved for a density matrix $\hat{\rho}$ using a master equation of the form [131]

$$\frac{\mathrm{d}}{\mathrm{d}t} \hat{\rho} = -\frac{\mathrm{i}}{\hbar} [\hat{\mathcal{H}}, \hat{\rho}] + \hat{L}(\hat{\rho}), \tag{5.6}$$

where $\hat{L}(\hat{\rho})$ is the Lindblad operator of the system, written as a sum of collapse operators $\hat{C}_n$[131]:

$$\hat{L}(\hat{\rho}) = \sum_n \left(2\hat{C}_n \hat{\rho} \hat{C}_n^{\dagger} - \hat{\rho} \hat{C}_n^{\dagger} \hat{C}_n - \hat{C}_n^{\dagger} \hat{C}_n \hat{\rho} \right). \tag{5.7}$$

The collapse operators, which in our case represent the loss of population in the system due to spontaneous emissions and photon losses from the cavity (with decay rate κ), can be written as $\sqrt{2\kappa}\hat{a}_1$ ($\sqrt{2\kappa}\hat{a}_2$) for a photon emission of polarisation 1 (2), and as $\sqrt{2\gamma_{ij}} * |s_j\rangle \langle s_i|$ for a spontaneous emission process that takes the atom from the state $|s_i\rangle$ to $|s_j\rangle$ at a rate γ_{ij}.

After setting up the Hamiltonian and collapse operators for the system, whose couplings are provided using the Atomic Density Matrix package for Mathematica [132], the master equation 5.6 is solved using the `mesolve` method from the quantum toolbox in Python (`QuTiP`) [133]. The techniques summarized here are packaged on the `rb-cqed` Python package [134].

5.2.2 Fully coherent method

The repumping of the atom could be performed by using coherent methods such as STIRAP, where two laser pulses are shaped to adiabatically transfer the state of an atom while avoiding the appearance of incoherent processes such as spontaneous emission. This idea leads to an estimated enhanced emission of sequential photons, and allows for the atom to be prepared in its desired state faster and more precisely than incoherent methods would. In what follows, we detail a potential procedure for repumping the atom using STIRAP, in two stages, as shown in Fig. 5.2.

5.2.2.1 Photon production stage

The photon production stage starts by having an atom prepared in the state $|F=2, m_F=-2\rangle$, where a v-STIRAP process 10MHz detuned below the resonance of the $|F'=2, m_F=-2\rangle$ state is driven to transfer the atom to the state $|F=1, m_F=-1\rangle$. For a 460 ns long pulse, the simulations yield a typical maximum emission efficiency of around 67%, which is as good as the coupling strength of the present cavity allows for the length of the pulse. The transition used has a stronger coupling than either of the transitions used in the previous scheme and, due to the adiabaticity of the production, the efficiency of the production process can be increased by producing longer photons. The ratio of photon emission into the cavity against spontaneous emission for this process is 1.6, which is better than what was achieved with the old polarised scheme, where a value of 1.4 was obtained [101]. Still, there is room for improving this further, and efforts are underway to determine the optimal set of parameters to be used.

5.2.2.2 Coherent re-preparation stage

Once the atom has emitted a photon, it must be brought back to the original state for another photon to be produced. For this reason, the repreparation state uses a regular STIRAP process, in which two lasers mediate the population transfer instead of it being driven by the cavity. This process transfers the atom from $|F=1, m_F=-1\rangle$ back to $|F=2, m_F=-2\rangle$. It can be driven with a laser with π polarisation (from $F=1$) and a circularly polarised [1] laser from $F=2$. The process is driven with two $\sin^2(t)$ pulses, each of them 150 ns long and separated by 45 ns. The intensities of each pulse are tuned such

---

[1] i.e. linearly polarised and injected orthogonally to the cavity axis, such that it decomposes into an equal superposition of $\sigma^+$and σ^-

that each transition sees a peak Rabi frequency of $2\pi \times 140\mathrm{MHz}$ (i.e. much more powerful that the v-STIRAP laser). This process is $\sim 96\%$ efficient, according to simulations.

5.2.2.3 Complete cycle

Successive v-STIRAP and STIRAP re-preparation cycles are the key to the application of this scheme. By preparing the atom in $|F = 2, m_F = -2\rangle$ and applying three photon production and re-preparation cycles there is a $\sim 25\%$ chance of 3 consecutive photon emissions. The fundamental upper limit that can be expected is given by the efficiency of each process when the system is prepared in its initial ideal state, and the probability of producing a photon being independent on whether a photon has been emitted in the previous step:

$$\mathcal{P}_{\text{limit}}(3) = (0.67 \times 0.96)^3 = 0.26.$$

One of the factors that will limit the repreparation efficiency is the population left over in undesired states after each v-STIRAP attempt. In general, an atom entering the cavity cannot be efficiently prepared into the Zeeman substate $|F = 2, m_F = -2\rangle$. Rather, when entering the cavity, a loaded atom will be prepared in a random ground state. A continual driving of the atom using successive photon production and coherent re-preparation cycles eventually makes the population accrue in the desired substates, as shown in Table 5.1. This has an important consequence: using the coherent repumping method does not need a separate repumping process. Just running the sequence eventually brings the atomic population back to the desired state, even when the atom has been incorrectly prepared.

In the simulations, an atom is initialised in one of the Zeeman sublevels of the ground states. As the desired laser pulses are applied, a percentage of the population larger than 50% ends up in the desired substate: the population of the atom was examined after 5, 10 and 15 combined cycles. The detuned driving of the the undesired states starts cascading the population towards the desired states. This can be seen in Fig. 5.2.

Since the atoms traverse the cavity mode for around 100 cycles, this means that the same atom could be able to produce multiple several-photon shots, making the efficiency of the source high enough for applications involving the use of multiple photons.

Initial atomic state $\|F, m_F\rangle$	$\mathcal{P}_{\|2,-2\rangle}$ after 5 cycles (%)	10 cycles (%)	15 cycles (%)
$\|1,-1\rangle$	69.2	64.3	63.8
$\|1,0\rangle$	55.5	62.8	63.6
$\|1,+1\rangle$	50.4	62.2	63.6
$\|2,-2\rangle$	67.6	64.2	63.8
$\|2,-1\rangle$	58.6	63.2	63.7
$\|2,0\rangle$	57.7	63.0	63.6
$\|2,+1\rangle$	58.2	63.1	63.6
$\|2,+2\rangle$	54.8	62.7	63.6

Table 5.1: Table describing the percentage of the population that ends up in the original state after 5,10 and 15 photon production and re-preparation cycles.

5.2.3 Method without magnetic fields

In what follows, we propose the implementation of an atomic source of polarised single photons which does not require a strong external magnetic field. The idea behind this method has been conceived and numerically simulated by Jan Ole Ernst, who intends to continue with its experimental implementation.

This method depends on a conceptual change with respect to the previous experimental methods used: the quantisation axis is now considered orthogonal with respect to the cavity axis. The method is composed of three stages: The first, a v-STIRAP photon production process similar to the one described in the previous method. The second: a coherent repumping of the atom back to its original state. This stage occurs continuously and on the scale of hundreds of nanoseconds, generating a stream of photons on the MHz scale. The third stage is an intermittent optical pumping cycle, used either to reinitialise atoms after a failed photon production sequence, or periodically, on a much slower, microsecond scale. Optical pumping is an excellent technique for re-initialising atoms that were lost to non-participating states during the preceding sequence, but its operation takes much longer than the coherent repumping because it involves a random population walk based on spontaneous emissions. The details of these three stages are described in the following subsections:

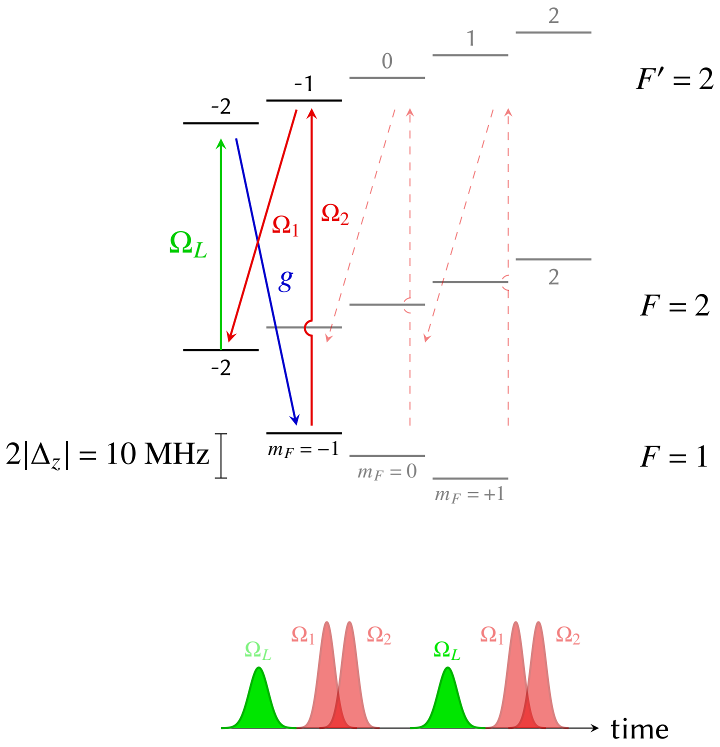

Figure 5.2: STIRAP re-pumping is used here to recover the initial state of the atom in a more selective and fast way with respect to optical pumping mechanisms. As the spontaneous emission is avoided, the photon emission process is completely coherent. This enables a precise control of the atomic population. The detuned driving of the undesired ground states also contriubutes to the cascading of the population towards the initially desired state, recovering the initial population.

5.2.3.1 Photon production stage

A cornerstone to comprehend this proposal is a change in the choice of quantisation axis. Unlike existing methods, where the quantisation axis is taken to be parallel to the cavity axis[37, 66], in this method we redefine the quantisation axis to be perpendicular to the cavity axis. This leads to a clear definition of the emitted photon polarisation, as will be outlined in the following.

Customarily, the quantisation axis is picked to lie along the cavity axis (which we have described as the z axis, as shown in Fig. 5.3 (a)), such that the cavity supports the two circularly polarised light modes (σ^+, σ^-) corresponding to the atomic transitions $\Delta m_F = \pm 1$ [37, 66]. In the laboratory frame, superpositions of the two circularly polarised light modes give rise to the following linear polarisations: $H = (\sigma^+ + \sigma^-)/\sqrt{2}$ and $V =$

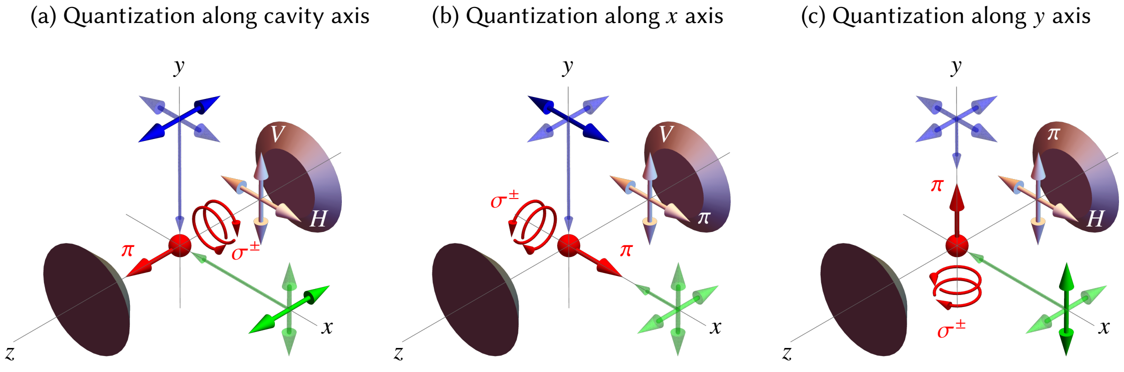
(a) Quantization along cavity axis (b) Quantization along x axis (c) Quantization along y axis

Figure 5.3: Atomic quantisation axis direction, either (a) parallel or (b,c) perpendicular to the cavity axis. In red, we see the orientation of the π, σ^+ and σ^- polarisations with respect to the quantisation axis. In green and blue, the light sent across the axes perpendicular to the cavity axis is shown. The polarisation bases for each of the beams describe a plane perpendicular to the axis of propagation. In solid blue and green colours, the polarisations of the beams which the atom will interpret as π-polarised are shown. In white, we see the two orthogonal modes that can be supported by the cavity, a key aspect for the production of polarised photons without the presence of magnetic fields.

$(\sigma^+ - \sigma^-)/\sqrt{2}i$, defined with respect to the laboratory frame and irrespective of the chosen quantisation axis. In contrast, for quantisation axes along the x and y directions, the cavity supports the polarisation modes spanned by (π, V) and (π, H), respectively.

Due to the physical arrangement of the experimental setup, the driving of the atom within the cavity is performed with laser light propagating parallel to the x or y axes. With a quantisation axis parallel to z, π-polarised light enters the cavity through either of these axes, as shown in Fig. 5.3 (a).

Without loss of generality, let us consider a quantisation axis parallel to the y axis. The subsequent photon production sequence is inspired by the atom-photon entanglement scheme first introduced in [25]: a single ^{87}Rb atom is coupled to an optical cavity and initially prepared in the state $|F = 2, m_F = 0\rangle$, meanwhile, the cavity is tuned to be resonant with the $F' = 1 \longrightarrow F = 1$. A laser with $\pi-$polarisation and Rabi frequency Ω_π, near-resonant on the $F = 2 \longrightarrow F' = 1$ transition, addresses the atom in the cavity, establishing a coupling to the level $|F' = 1, m_F = 0\rangle$.

The cavity supports the dipole allowed $\sigma^\pm$ transitions while the transition to

$|F=1, m_F=0\rangle$ is dipole forbidden. Therefore, no π polarised photons can be emitted. A v-STIRAP process adiabatically transfers the population from the initial state to a superposition of hyperfine states of the $F=1$ level and leads an atom-photon superposition state which reads:

$$\left|\Psi_{\text{atom, photon}}\right\rangle = \frac{1}{\sqrt{2}}\left(\left|m_F=+1, \sigma^-\right\rangle - \left|m_F=-1, \sigma^+\right\rangle\right). \tag{5.8}$$

Any emitted photon will either have σ^+ or σ^- polarisations with respect to the quantisation axis, but the cavity, with its quantisation axis along y, can only sustain the superposition $H = (\sigma^+ + \sigma^-)/\sqrt{2}$. Therefore, all the emitted photons will forcibly have this polarisation.

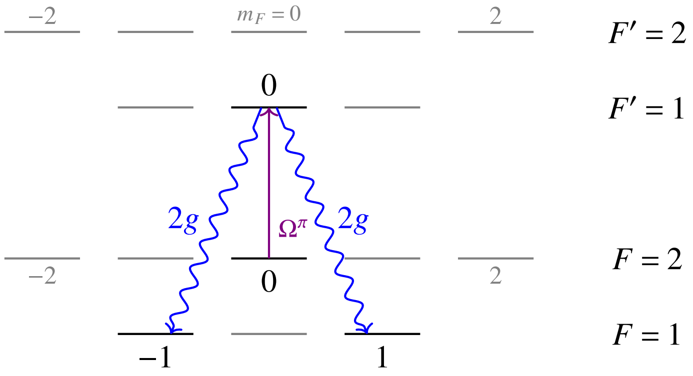

Figure 5.4: Photon production stage. The atom is originally prepared into the $|F=2, m_F=0\rangle$ state and driven using a laser and the cavity into a superposition between the states $|F=1, m_F=1\rangle$ and $|F=1, m_F=-1\rangle$. This leaves any photon emission to have a superposition in its polarisation between σ^+ and σ^-, but the cavity can only sustain the superposition $(\sigma^+ + \sigma^-)/\sqrt{2}$, leading to a horizontally polarised photon being emitted from the cavity.

After having estimated the driving of these processes using the methods shown in Chapter 2, we have simulated this process for two existing cavities: one operating at the edge of the strong coupling regime with a cooperativity factor around $C = 1.5$ [66], and one that operates deeply in the strong coupling regime with a cooperativity around $C = 10$ [35]. With these two cavities, we have been able to simulate photon production processes achieving total efficiencies[2] of up to 77% and 86% respectively.

5.2.3.2 Coherent re-preparation stage

After a photon has been successfully emitted, the atom is left in the state $|-\rangle = (|F=1, m_F=-1\rangle - |F=1, m_F=-1\rangle)/\sqrt{2}$. It can be prepared back into the desired initial state, $|F=2, m_F=0\rangle$ using a coherent STIRAP [72] procedure which, as in the previous method, also involves two laser pulses.

The transition between the two ground states is dipole forbidden so a two-photon resonance condition is established between the transitions between the superposition of $F=1$ ground states ($|-\rangle$ 5.8) and $F'=1, m_F=0$ and the transition between $F=2, m_F=0$ and $F'=1, m_F=0$. One pulse is polarised such that its polarisation corresponds to a linear combination of σ^+ and σ^- polarised light pulses, resonant with the $F=1 \longrightarrow F'=1$ transition. The polarisation of the laser light and thus the phase between the two circularly polarised components must match the phase of photon polarisation derived from 5.8. The other pulse is π polarised and resonant with the $F=2 \longrightarrow F'=1$ transition. Both laser pulses have equal effective Rabi frequencies (re-scaled with respect to the atomic transition strengths). Treating the Rabi frequencies of the two transitions as time dependent control parameters and shaping them optimally [135] allows for simulated theoretical efficiencies that reach up to 97% with pulse shapes such as the ones shown in Fig. 5.5. Given that the system has spontaneous emission losses given by a γ commensurate with the other atom-cavity parameters, unit fidelity cannot be achieved [136].

5.2.3.3 Incoherent re-preparation stage

During the photon production cycle, the atom may decohere into an undesirable Zeeman state, which could arise from a loss of adiabaticity when experimentally driving a vSTIRAP pulse. Moreover, an arbitrary ^{87}Rb atom passing through the cavity can be initially populated in a random ground state after having left the MOT.

To ensure an adequate re-preparation of the atom, a two-stage optical pumping process

---

[2] In this context, a total efficiency corresponds to the combined efficiency of producing a single photon and re-preparing the atom back to its original state.

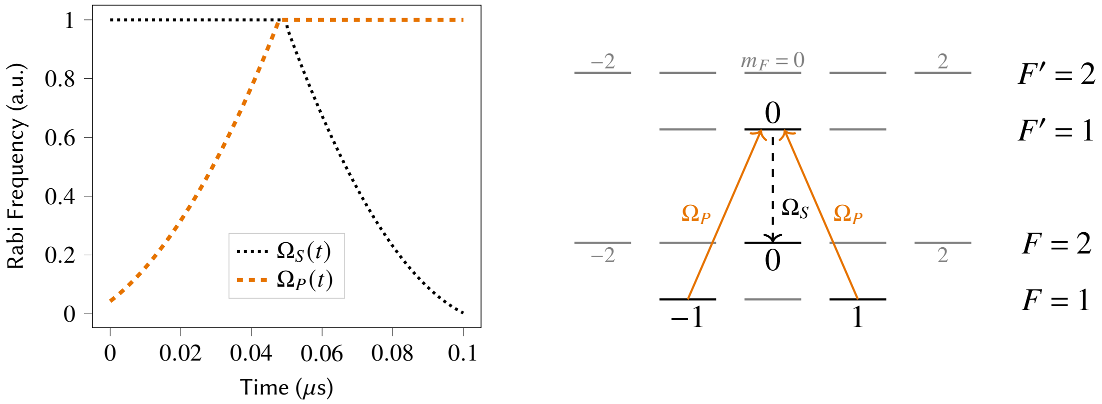

Figure 5.5: (a)The optimally shaped pulses used for the STIRAP process that coherently repumps the atom. (b) Outlines the repumping scheme, transferring the atomic population from Eq. 5.8, back to the desired initial state $|F = 2, m_F = 0\rangle$.

$F = 2, m_F =$	-2	-1	0	1	2
$n = 1$	0	0.01	0.878	0.01	0
$n = 10$	0.121	0.078	0.44	0.078	0.121
$n = 100$	0.129	0.109	0.358	0.109	0.129

Table 5.2: Population after several repumping cycles.

can be used to periodically bring the atom back into the initial $|F = 2, m_F = 0\rangle$ state used for photon production.

One possible optical pumping procedure would require two π-polarised lasers (with respect to the quantisation axis, travelling along the x-axis), nearly resonant with the $F = 1 \rightarrow F' = 2$ and $F = 2 \rightarrow F' = 2$ transitions. The first laser, from $F = 1$ to $F' = 2$, ensures that any population in $F = 1$ is eventually pumped into the excited state and decays to $F = 2$ through spontaneous emission. As a consequence, the population gradually accumulates in the $F = 2$ level. The second laser ensures that continued excitation from $F = 2$ to $F' = 2$ and spontaneous emission brings the atomic population back to the original state, since the transition $|F = 2, m_F = 0\rangle \longrightarrow |F' = 2, m_F = 0\rangle$ is dipole forbidden. This is shown in Fig 5.6.

Since the initialisation and re-preparation efficiencies occur over different time scales, a careful optimization of the parameters can be performed. Due to the randomness associated with the incoherent re-preparation process, the time scales associated with it are generally longer than those associated with a coherent re-preparation. This can

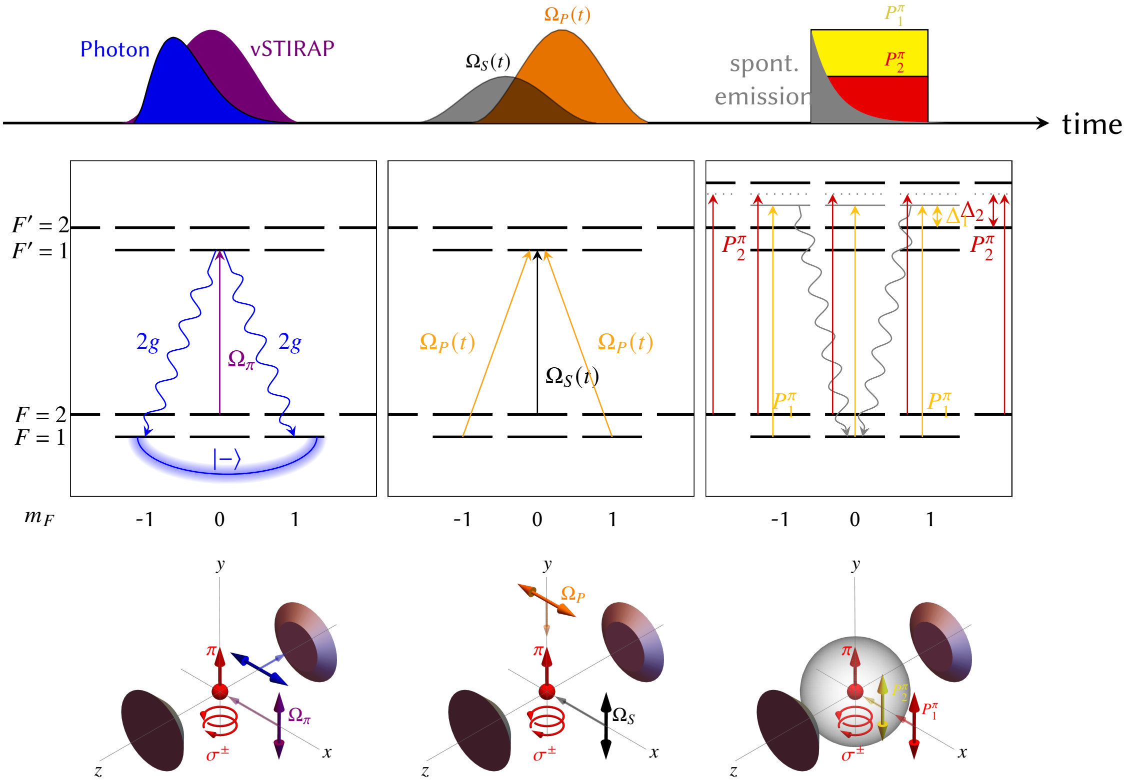

Figure 5.6: The entire experimental sequence for the method for producing polarised photons without magnetic fields is shown here. First, V-STIRAP is performed, leaving the atom in the coherent superposition state $|-\rangle$. This is followed by a fast coherent repumping, which generates a stream of several photons. After a failed coherent re-preparation, the atom can be brought back into the desired initial state using incoherent methods, i.e., optical pumping. This is also used to initialise the atom into the desired Zeeman state when it is first loaded into the cavity. As the incoherent methods rely on the spontaneous emission of the atom, which is isotropic, it is represented by the grey sphere shown in this figure.

be counterintuitive, given that coherent methods are generally adiabatic. However, their specificity and the design of pulses to optimise population transfer make them rapid with respect to incoherent methods.

It is important to stress that a correct atomic preparation is crucial for the generation of polarised photons. Indeed, if the atom is incorrectly re-prepared into a wrong state, for example, $F = 2, m_F = -1$, the π transition would no longer be dipole forbidden.

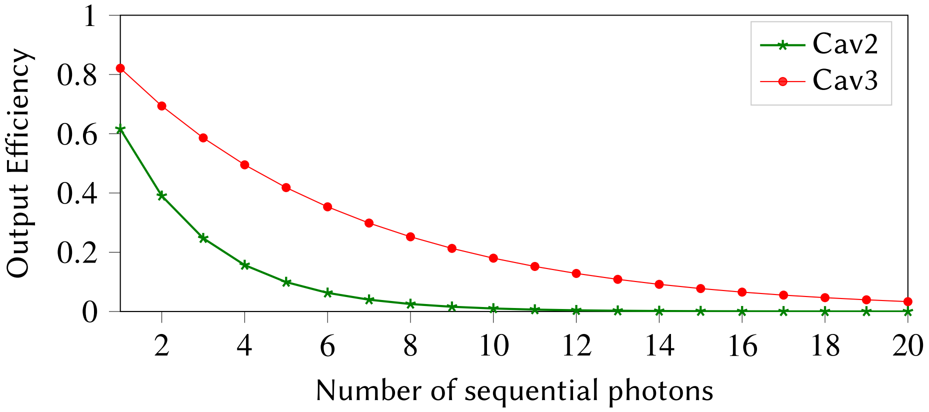

Figure 5.7: This figure compares the efficiency of producing a stream of single photons using cavities of different cooperativity. For a cavity with $C \approx 10$, the efficiency of producing streams of more than 10 photon theoretically reaches around 20%. This simulation has been performed by Jan Ernst using the `rb-cqed`[134] Python package.

5.2.4 Pushing single-photon sources to the limit

The single photon production efficiencies presented in this chapter, derived from simulation, are pushing atom cavity sources to the limit. Theoretically, the driving systems described here would be possible to achieve 10 consecutive photon streams with a production efficiency of up to around 20%. This is shown in Fig. 5.7. Additionally, recent results in the community [109] show the excellent scalability that cavity-QED systems provide for the generation of entangled cluster states with respect to other platforms, further making the case for improving the efficiency of producing polarised single photons using the methods described in this chapter.

The efficiency of single photon production processes is, in theory, limited by $\eta_{\text{max}} = 2C/(2C+1)$. When considering idealised three-level atoms embedded within the cavities, a lack of cross-talk between atomic transitions enables the realization of theoretical efficiencies close to η_{max}. This is, unfortunately, not the case when considering the full atomic structure of the atom. As a consequence, Fig. 5.8 shows that the photon production efficiency in the D_2 line of ^{87}Rb is already capped at around 80%, for cavities with cooperativities of $C \approx 10$, a requirement similar to those achieved by our most recent cavity designs, such as the tapered cavity design, Cav3, mentioned in Chapter 3.

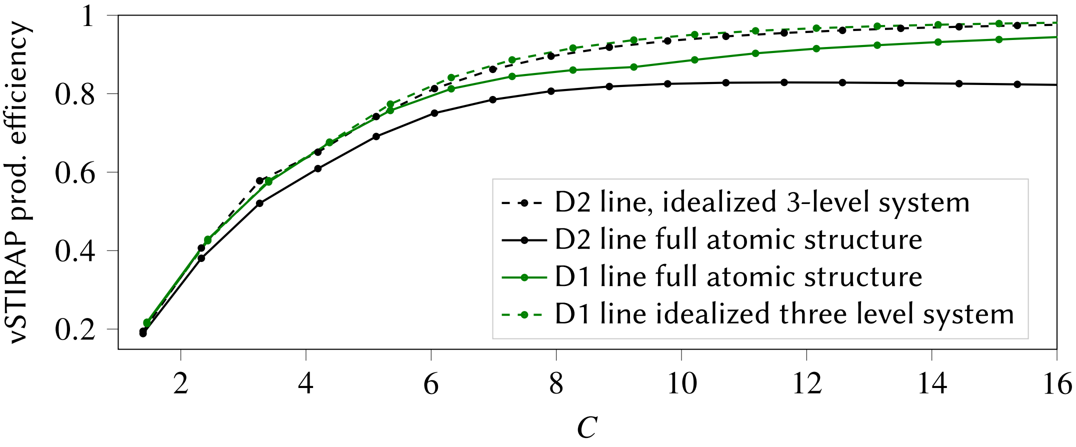

Figure 5.8: This figure compares the efficiency of single photon production processes, theoretically limited by $\eta_{\max} = 2C/(2C+1)$ against the cooperativity. For idealised three-level systems with no cross-talk between transitions, the theoretical efficiencies achieved reach almost $\eta_{\max}$. This is not the case when the full atomic structure of the D_1 and the D_2 line of ^{87}Rb are considered. Indeed, the limit for photon production using the D_2 line, 80%, is already achieved for cavities with cooperativities of $C \approx 10$, such as Cav3 from Chapter 3. This simulation has been performed by Jan Ernst using the rb-cqed Python package.

5.3 Single photon demultiplexing

So far, we have described efforts and methods for generating several single photons serially leaving the cavity with high efficiencies. However, one key requirement for moving beyond two-photon interference and into reaching the goal of having the time-resolved interference of several single photons at the entries of a multimode interferometer or other optical quantum network is to use a single photon demultiplexer: if photons are being input in series from the same input channel, the action of the demultiplexer is to emit each of the photons at the same time through different output channels.

At the heart of the operation of a demultiplexer is an Electro Optic Modulator (EOM), a device which can switch the polarisation of the light passing through it depending on an applied voltage. If we operate an EOM at half of the repetition rate of our single-photon source, a continuous stream of horizontally polarised light will be converted into a stream of light with alternating horizontal and vertical polarisations. This stream can then be split deterministically using polarising Beam Splitters (PBS), which deviate the light to different paths depending on its polarisation. By introducing a delay line after the earliest pulse, two pulses of alternating polarisation which were previously arriving one after the other can now be parallelised to arrive simultaneously. The concatenation of an EOM, a PBS, a HWP and a delay line composes a *switching unit* that converts a stream of identical photons into a pair of photons whose wave packets arrive at the same time in different outputs. The concatenation of several switching units allows for the construction of a demultiplexing unit to probe the time-resolved interference of several single photons. In this section, we will explain the working principle and characterisation of a single-photon demultiplexer which has been implemented[3] to eventually perform the interference of multiple single photons at the input ports of a multimode interferometer.

5.3.1 Electro-optic modulators

In order to understand how a single switching unit operates, we need to understand the behaviour that allows EOMs to switch the polarisation of incident light. EOMs rely on the Pockels effect, where the birefringence of a crystal varies following an applied electric field, E [38]. This leads to a change in the refractive indices of the crystal, as:

$$n_j(E) = n_j - \frac{1}{2} r_j n_j^3 E,\ j \in \{x, z\}. \tag{5.9}$$

Here, r_j is the electro-optic coefficient associated with the jth axis of the crystal (x for extraordinary, z for ordinary), and E refers to the applied electric field across the EOM. This change of refractive index in each of the crystal axes creates a phase difference $\delta\varphi$ between the components of the electric field, given by

$$\delta\varphi = \left[(n_x - n_z) + \left(\frac{1}{2} r_z n_z^3 E - \frac{1}{2} r_x n_x^3 E\right) \right] kl, \tag{5.10}$$

---

[3] The construction of this demultiplexer has been done in close collaboration with Jiawang Li and Jan Ernst, respectively a master and a DPhil student in the laboratory.

where k refers to the wave-vector in vacuum and l is the length of the crystal in the direction the electric field is propagating. Since the applied field E is linearly dependent on the voltage V across the crystal, the additional birefringence is also proportional to the voltage applied, and the contributions of the applied voltage to the overall phase shift can then be written as [137]

$$\delta\varphi = \frac{\pi(V - V_{\text{off}})}{V_\pi}, \tag{5.11}$$

where V_{off} is an offset voltage that when applied exactly compensates for the natural birefringence of the crystal, resulting in no phase shift and therefore no rotation of linearly polarised light. In contrast, V_π is defined as the voltage that results in a phase shift of π between the z and x components of the propagating electric field. The voltage required to generate an *overall* phase shift of π, taking into account the natural birefringence of the crystal, is then $V_\pi + V_{\text{off}} \equiv V_{\text{on}}$. From this, the relationship between the expected power from an EOM output channel and the phase shift induced by the EOM is given by

$$P = P_{\text{total}} \cos^2\left(\frac{\delta\varphi}{2}\right) = P_{\text{total}} \cos^2\left(\frac{\pi\,(V - V_{\text{off}})}{2V_\pi}\right). \tag{5.12}$$

In practical terms, with the incoming light polarised to match the slow axis of the EOM, it is possible to change the EOM voltage between V_{off} and V_π in such a way that the outgoing light alternates between being horizontally (no change) and vertically polarised.

Experimentally, the EOMs used are EXCELITAS LINOS LM0202, suitable for a 400-850nm operation.V_π is quoted as 210V±10V at 633nm, which translates to 258V±26V at a wavelength of 780nm. Each EOM is driven by a LINOS DIV20 pulse amplifier capable of delivering square signals with voltages between 0 and 590V. These pulse amplifiers are in turn fed with TTL[4] input signals at 50Ω or 600Ω impedance.

The operation voltages for the EOM are characterised by sending continuous light at 780nm of fixed polarisation into a single switching unit as described in Fig. 5.10 using a polarisation maintaining fibre, while manually varying the voltage applied across the EOM from 0 to 500V. The output light is then sent to a PBS whose transmissive polarisation matches the slow axis of the EOM, and the light from the transmitted arm is read out in a

---

[4] Electronic signals with logical states 0 and 1 defined by voltage ranges 0V-0.8V and 2V-5V respectively.

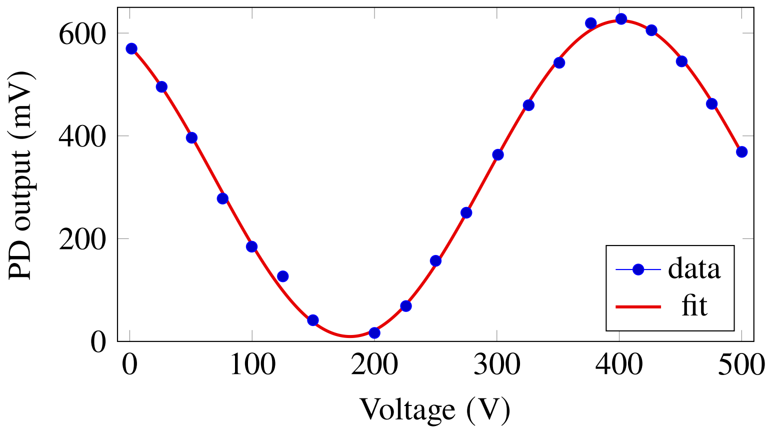

Figure 5.9: Characterisation of EOM displaying a sinusoidal relationship between power output and voltage applied. The experimental fit follows the relationship $I_{\text{out}}(V) = 316.77 + 307.249\cos(13.15 + 0.01421V)$. This behaviour leads to operation voltages of $V_{\text{off}} = (180 \pm 10)\,\text{V}$ (the minimum power output), $V_{\text{on}} = (400 \pm 22)\,\text{V}$ (the maximum power output) and $V_{\pi} = (220 \pm 32)\,\text{V}$. The value of V_{π} found experimentally is consistent with the manufacturer's value of 258V±26V.

photodiode. The results are shown in fig. 5.9.

5.3.1.1 Single Switching Unit

When combining the operation of an EOM with a PBS, pulses of light of alternating polarisation exit the setup through the different PBS output ports. As a result, the photons are sorted deterministically into different output channels. The operation of a single switching unit is summarized in Fig. 5.10, where photons are represented by coloured squares.

To characterise the switching efficiency of a switching unit, we must understand how the light is transmitted between the V_{off} and V_{π} modes of operation of an EOM. The visibility, v, provides a convenient way of quantifying the accuracy with which a single switching unit is able to route light into the desired channels. The visibility v is defined by

$$v = \frac{I_{\text{max}} - I_{\text{min}}}{I_{\text{max}} + I_{\text{min}}}, \tag{5.13}$$

where I_{max} and I_{min} are respectively, the maximum and minimum intensities measured from the output of a PBS after an EOM [138].

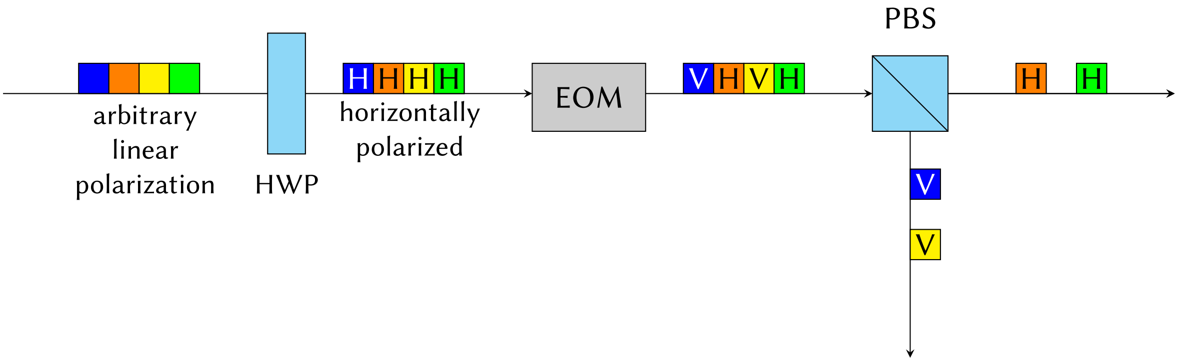

Figure 5.10: Operation of a single switching unit. H and V represent light pulses of horizontal and vertical polarisations, respectively. The HWP rotates the polarisation of the incoming photons. The EOM then imparts horizontal and vertical polarisations alternatingly to the photons, which are subsequently sorted by the PBS.

In the ideal case, a switching unit will show $I_{\text{min}} = 0$ when the EOM is set to V_{π}, which indicates that all input light is being correctly sorted into the reflected channel of a PBS. Thus, eq. 5.13 yields a v of 100% for an EOM exhibiting perfect switching behaviour. Hence, it legitimately quantifies switching accuracy. The visibility, however, does not account for overall losses at each optical component including those from incomplete coupling of light into the fibres. For each of the single switching units implemented, the visibility is estimated to be of approximately 92%.

5.3.1.2 Photon Switchyard

The completed switchyard comprises three single switching units concatenated as shown in Fig. 5.11, where the signals driving the respective EOMs are indicated by the red and purple traces. In this setup, EOM 1 is driven with a square wave of frequency $f/2$, where f is the intended photon repetition rate. This ensures that the input photons are alternatively sorted into the two output channels of the first PBS, while EOMs 2 and 3 are driven at $f/4$. Each EOM in a switching unit is connected to a separate pulse amplifier, but all three pulse amplifiers are connected to the outputs of a TTL counter[5] that ensures

---

[5] Originally custom made using a 74LS93 integrated circuit, then expanded and fabricated by Tausand electronics to support eight channels.

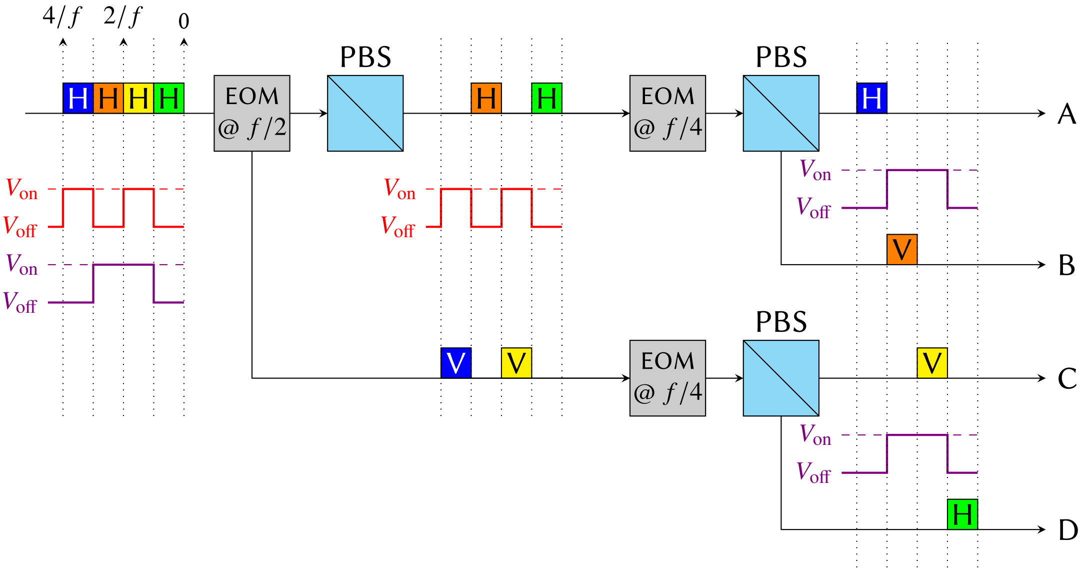

Figure 5.11: Operation of concatenated single switching units with f being the photon repetition rate. EOM 1 is driven with the red waveform of frequency $f/2$ while EOMs 2 and 3 are driven in tandem with the purple waveform of frequency $f/4$. Photons are first sorted at EOM 1 into EOM 2 or 3, then further sorted at EOM 2 or 3 into outputs A, B, C or D.

a fixed phase relationship between the operation of all the EOMs. The TTL counter is used to divide the frequency of the square pulses that drive all the EOMs simultaneously, therefore outputting one pulse at $f/2$ and two at $f/4$, as shown in Fig. 5.12.

When CW light is input to the switchyard, the outputs show rectangular waves with periods as low as 663ns±8ns, consistent with the driving frequency of 1.5MHz. The rise and fall times associated with these square pulses are measured to be approximately 50ns±8ns. This is appropriate for the routing of the single photons produced by our sources, as the novel schemes described in this section require repumping times of approximately 100ns, as shown in Fig. 5.13. The transmission efficiency of each switching unit is determined to be approximately 97% by summing the measured output from each of the arms after the PBS. If all channels are measured simultaneously, a clear switching behaviour is observed at all outputs of the switchyard (see Fig. 5.14.). The appearance of the pulsed patterns show rectangular waves possessing a 25% duty cycle, essentially dividing the total light into four square pulses.

For testing purposes on the modulator timings and response times, pulsed light is

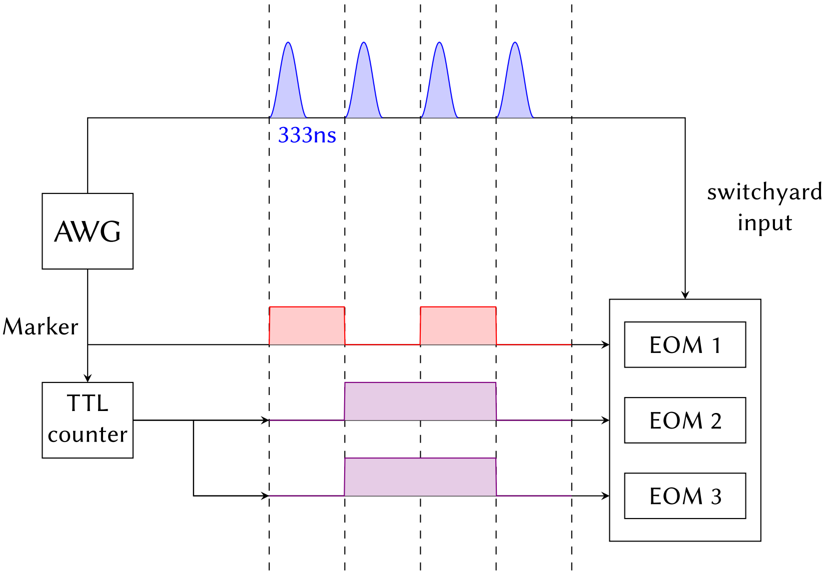

Figure 5.12: Configuration to maintain a fixed phase relationship between input pulses and EOMs. The marker pulse is partially used to drive EOM 1 while also being fed into the TTL counter to half its frequency. The output from the TTL counter is then used to drive EOMs 2 and 3 concurrently.

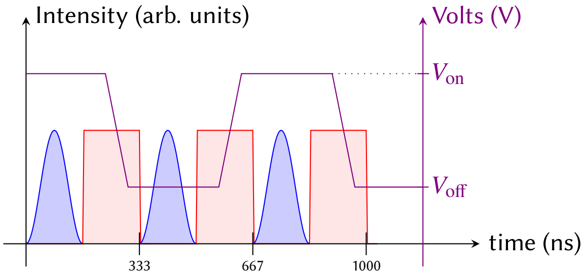

Figure 5.13: Scheme to accommodate rise and fall times within repumping gaps. The solid and dashed black lines represent the shaping and repump phase of the single photons respectively. Rise/fall times are effectively accommodated within the repumping gaps.

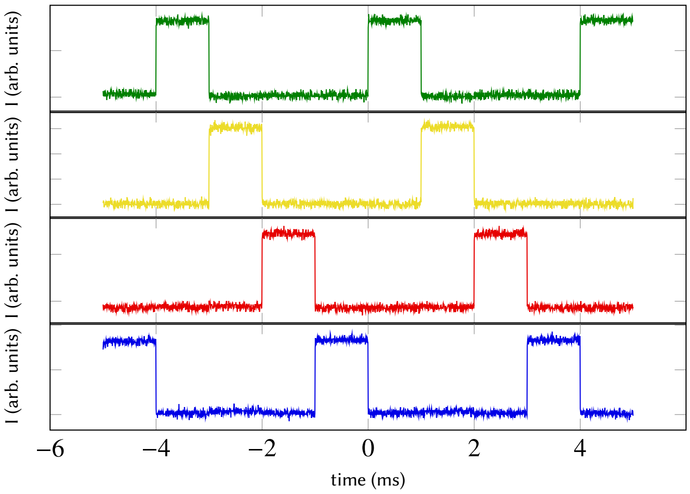

Figure 5.14: Relative behaviour between output channels A, B, C and D of the switchyard, without fibre delay lines being implemented. Clear switching behaviour is observed with pulses having a 25% duty cycle - consistent with our predictions. . This represents how one in every four light pulses will be sorted into each channel. The intensities are shown in arbitrary units to account for different photodiode sensitivities.

sent into the switchyard using an acousto-optic modulator (Crystal Technology 3110-120) controlled by an AWG (Tabor Electronics WX1284C). The AWG is capable of delivering 2V peak-to-peak and square waves of up to 500MHz. The AWG also generates a square, marker pulse that acts as the common clock for all the switching times, as shown in Fig. 5.12. The pulsed light is produced with a $\sin^2(\omega t)$ temporal profile and a period of 333ns, which corresponds to a repetition rate of $f = 3$ MHz. When the pulses are shaped, the switchyard works as expected and one in every four pulses is output from each of the channels, as shown in Fig. 5.16.

To produce photons that are indistinguishable for boson sampling purposes, it is necessary that they arrive simultaneously at different outputs after the switching process. The second, third and fourth routed photons, all emitted at different times, have arrival times delayed by $2/f$, $1/f$ and $3/f$ respectively. To compensate this and allow for a simultaneous arrival, it is possible to connect fibre delay lines of appropriate lengths to each of the output channels such that a sequence of four photons fed into the switchyard one after another each experiences the correct amount of delay for them to arrive simultaneously at the outputs. We can relate the difference in arrival time, δt to the difference in length of the fibre delay lines, δl_{m} as

Channels	Deviation with Respect to Channel D (ns)	Delay Length (m)
A	-22.5	200
B	-7.5	66.7
C	-15	133
D	0	0

Figure 5.15: Time deviations and delay lengths used for simultaneous pulse arrival.

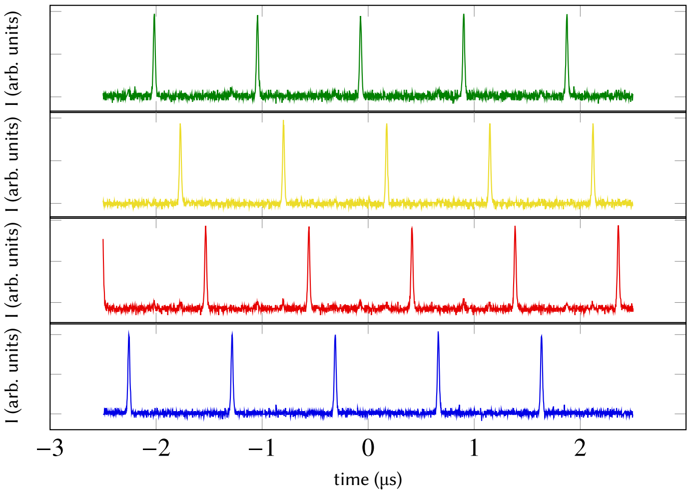

Figure 5.16: Relative behaviour of output channels A, B, C and D for shaped pulses, without fibre delay lines being implemented. As every output channel outputs only one of every four pulses, the switchyard works as expected.

$$\frac{\delta l_{\mathrm{m}}}{c} = \delta t = \frac{m}{f}, \tag{5.14}$$

where c refers to the speed of light in the fibre and $m \in \{0, 1, 2, 3\}$, as shown in Fig. 5.11 Fibre delay lines are now connected to the output channels as a proof-of-concept for the simultaneous arrival of pulses across all channels. Using eq. 5.14 for $f = 1.5$MHz and refractive index $n \approx 1.5$, the appropriate fibre delay lengths required for each of the channels are calculated (as shown in Table 5.15) and the fibre inputs are set to be connected to the switchyard using kineMATIX fibre couplers, making all channels arrive almost simultaneously. Preliminary data, shown in Fig. 5.17, shows the simultaneous arrival of pulsed light when using the stipulated fibre delay lines.

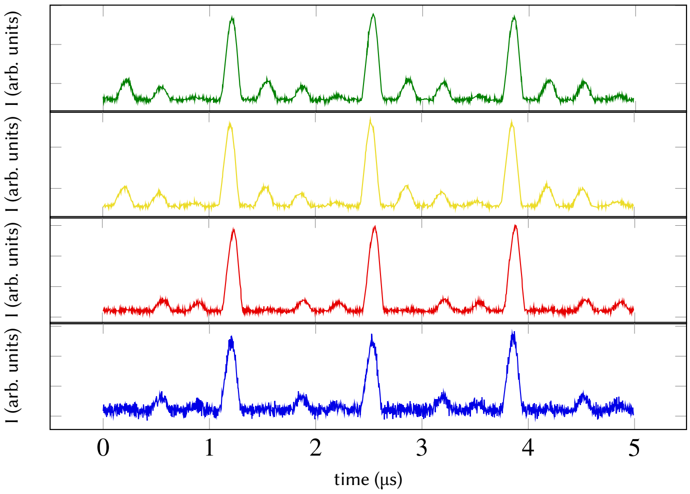

Figure 5.17: Preliminary data for the output behaviour of channels A, B, C and D for shaped pulses implementing fibre delay lines. A simultaneous pulse arrival is clearly demonstrated, but the switching efficiencies shown in Fig. 5.16 are yet to be improved.

5.4 Conclusions

In conclusion, we have conceptualised and built a switchyard employing a scalable approach capable of producing four simultaneously-arriving photons when a steady stream of photons are injected. We have tested the switchyard using both continuous and shaped pulses of light, yielding visibilities of 85% and 84% respectively. Finally, we have also performed a successful proof-of-concept of employing fibre delay lines to achieve the simultaneous arrival of pulses in different channels of the switchyard. For both continuous and shaped pulses of light, any deviations in arrival times of the pulses across different channels represented 4% or lesser of the temporal width of the pulses.

We seek to improve the extent for which photons arrive simultaneously by fine-adjusting the generating sequence on the AWG to match up with the given fibre lengths. When the switchyard is eventually operating with single photons, we plan to quantify simultaneity more accurately using Hong-Ou-Mandel interferometry.

Ultimately, we intend to carry out time-resolved multimode interferometry with the demultiplexed photons generated by the switchyard. This opens the door for us to perform 4-photon boson sampling as a means of establishing quantum superiority over classical computational devices - where such a task is considered to be demanding [18]. Moreover, the scalability of the switchyard enables a conceptually simple way of implementing boson sampling with an even larger number of photons, for which the source efficiencies must be improved. Given that source efficiencies can be improved by increasing the cooperativity of the atom-cavity system, efforts are underway [35, 36] to make the mode volumes of cavities smaller, enabling stronger coupling.

One of the key problems that arises when mode volumes are made smaller is the inclusion of a multilayer structure, which is negligible for large structures but starts becoming considerable for quantisation and light propagation. In the next chapter, we explore how the modelling of shorter cavities can be understood, quantized and reconciled with cavities comprising thin reflectors, when the multilayer dielectric stacks that make their mirrors are taken into account. This will be the topic of the next chapter.

*"**Shrek:** Onions have layers. Ogres have layers... You get it? We both have layers."*
***Donkey:** Oh, you both have layers. Oh. You know, not everybody likes onions.*
Cake! Everybody loves cake! Cakes have layers!"

—Shrek (2001)

6

The impact of multilayer dielectric stacks on light-matter coupling

The work presented in this chapter is adapted from the publication *"Light-matter interaction in open cavities with dielectric stacks",* published in Appl. Phys. Lett. **118**, 154002 (2021). [139].

6.1 Introduction

The finesse of a cavity, defined as the ratio of a cavity's free spectral range to its linewidth, ensures a good spectral resolution of each cavity resonance: If a single emitter such as an atom has a transition linewidth comparable to that of a cavity, it is possible to assume that atom-cavity interaction is limited to a single field mode.

To achieve the high mirror reflectivities required for enabling strongly coupled atom-cavity interactions, it is customary to use mirrors with highly reflective dielectric coatings, also called Bragg stacks [140, 141].

Dielectric Bragg stacks are composed of several layer pairs of dielectric materials whose refractive indices alternate. The optical thickness of said layers is with a quarter of the wavelength used. As high reflectivities are only achieved for a large number of such layers, it is customary for incident light to penetrate the stack through several layers before decaying.

From Chapter 5 we have identified that one of the key requirements for an atom-cavity system to produce photons with high efficiency in a vSTIRAP arrangement is the use of a high cooperativity system. High cooperativity systems can be achieved by minimising the mode volume of a cavity, which can be performed by either increasing the curvature of the mirrors forming the cavity, as is the case for Cav3 in Chapter 3, or by reducing the spacing between the mirrors.

At its extreme, the mirror spacing used for forming a cavity can be of the same order as the wavelength of interest [142]. This increases the relative portion of the cavity mode leaking within the dielectric stack [140, 143], potentially rendering inaccurate the customary spectral properties of a Fabry-Pérot resonator discussed in Chapter 2, such as the cavity's resonance frequency, linewidth and free spectral range.

The propagation of light in cavities limited by dielectric mirrors has been studied in the past under a resonance condition, in which the light propagating matches both the frequency for which the mirrors were designed to be reflective, and the frequency for which a Fabry-Pérot cavity with a mirror spacing of equal length would be resonant [140, 144, 145].

In this chapter, we go a step further in considering the more general case of a wave with an arbitrary wavelength traveling through the stack. This is especially relevant for producing single photons with atoms in cavities, as the atomic structure and the driving in the cavity require the use of several frequencies, potentially detuned by a significant number of cavity linewidths. To this end, in this chapter we write a closed expression for the coupling between an atom and the field within a cavity whose mirrors are dielectric multilayer stacks. A similar result has only been previously reported in the literature for the case of single-layered dielectric mirrors [146].

When modelling the dynamics of light-matter interaction within a cavity, the quantized light field is customarily normalised in terms of its quantisation volume, which normally corresponds to the geometric volume of the optical resonator [147]. This is indeed the case for the simple coupling expression shown in Eq.2.17.

In the case of the high-cooperativity cavities we consider in this chapter, modelling the surface of the mirror as a hard boundary to the cavity mode is no longer appropriate. To rectify this, we consider an open cavity system where the electric field is able to propagate through the dielectric mirror and couples to external free-space modes. This departs from the standard notion of having a mode volume and well defined frequency modes of the resonator, suitably modifying our calculation of the Purcell Factor. Whilst some aspects of this quantisation have already been addressed in the past, [148, 149], a description which takes into account a large number of dielectric layers has only been reported in the cases where the traveling wavelength coincides with the design wavelength of the stack.

In this chapter we revise the concept of mode volume and cavity resonance frequency for a cavity formed from dielectric mirrors. First, we describe the general quantisation procedure to be used for an atom within a cavity, where it interacts with a global electromagnetic field. This procedure departs from the standard input-output formulation used in the existing literature reporting open optical systems [147, 150, 151]. From this, we obtain a general expression for the coupling strength between the electromagnetic field modes and an atom placed within a cavity. One target application is the production of single photons leaking out from one side of the cavity. We thus consider a cavity which consists of one perfectly reflective mirror and one partially transparent dielectric mirror of finite thickness and real refractive index, a case that has been considered extensively in the literature [147, 150, 152].

In the intermediate subsections of the chapter, the model is expanded to describe a multilayer stack. This allows for a discussion on a more realistic specification of effective cavity lengths and corresponding mode volumes for short cavities, whose mirror separation is on the order of the wavelengths traveling through. The obtained results show that three quantities that are usually equal for cavities with thin mirrors differ substantially with this model: (i) the expected resonance frequency of the cavity, (ii) the resonance frequency of the emitter and (iii) the design frequency of the dielectric stack. By considering the limiting conditions to these effects, we demonstrate that the standard models of optical resonance are asymptotically re-achieved at extended cavity lengths.

In the final subsections of the chapter, a new model is developed for calculating the coupling of an emitter to the light field in the described dielectric cavities. The modelling considers the system to be an open quantum system, unconstrained by the surface of the mirrors.

6.2 Atom-field coupling

First, we describe the procedure for atom-field coupling: we will consider the physical situation of placing an atom between the mirrors of a cavity. In order to calculate an atom-cavity coupling, we first derive the modes that correspond to the solutions of the Maxwell's equations in a given physical system. Such physical system corresponds here to the set composed of the cavity, the multilayer stack and the outside environment. A quantisation is then performed on the calculated field.

Since the cavity mirror structures that we consider are either flat or have experimentally large curvature radii, on the order of centimetres, we will assume that the electromagnetic field between the mirrors can be separated into the product of a longitudinal and transverse component and only consider the longitudinal propagation throughout the chapter. This gives rise to the paraxial approximation for the Helmholtz equation [45].

The rectangular or cylindrical structures of the transverse modes arising in a cavity is a well known phenomenon [48], but the effects described here would apply similarly to any transverse mode. The emitters considered can only couple to one of the transverse modes sustained by the cavity, and as a consequence, the main effect that contributes to the coupling resides in the longitudinal position of the emitter. As a consequence, we can restrict ourselves to considering the cavity mode to be the fundamental one. Similarly, we will neglect any polarisation effect that may arise within the cavity.

The electromagnetic field within a cavity is described by solving the Helmholtz equation:

$$\left(\frac{d^2}{dx^2}+\epsilon_r(x)\frac{\omega^2}{c^2}\right)\Phi_\omega(x)=0, \tag{6.1}$$

where $\epsilon_r(x)$ is the relative permittivity of the physical medium, $\Phi_\omega(x)$ is the space-dependent field eigenmode of continuous index $\omega=2\pi c/\lambda$, λ is the wavelength of the wave travelling through the structure and c is the speed of light. The orthonormalisation condition for these modes is given by:

$$\langle\Phi_\omega,\Phi_{\omega'}\rangle=\int_{-\infty}^{\infty}dx\;\epsilon_r(x)\,\Phi_\omega^*(x)\,\Phi_{\omega'}(x)=\delta(\omega-\omega'). \tag{6.2}$$

For convenience, the eigenmodes solving Eq. 6.1 can be spatially separated into three regions: between the mirrors, within the stack, and outside of the cavity:

$$\Phi_\omega(x)=\Phi_{\omega,\text{in}}(x)+\Phi_{\omega,\text{stack}}(x)+\Phi_{\omega,\text{out}}(x). \tag{6.3}$$

After having obtained the eigenmodes $\Phi_\omega(x)$, it is possible to write a corresponding quantised electric field in the Schrödinger picture as:

$$\hat{E}(x)=-i\int_0^{\infty}d\omega\sqrt{\frac{\hbar\omega}{2\varepsilon_0}}\left(\Phi_\omega(x)\,\hat{a}_\omega-\Phi_\omega^*(x)\,\hat{a}_\omega^\dagger\right), \tag{6.4}$$

where

$$\begin{aligned}[\hat{a}_\omega,\hat{a}_{\omega'}^\dagger]&=\delta(\omega-\omega'),\\ [\hat{a}_\omega,\hat{a}_{\omega'}]&=0.\end{aligned} \tag{6.5}$$

Here, $\hat{a}_\omega$ and $\hat{a}_\omega^\dagger$ correspond to the annihilation and creation operators of photons with angular frequency ω. We highlight that the above quantisation procedure from first principles does not break the modes into separate parts (as opposed to any approach first quantising the field inside a perfect cavity and subsequently coupling the field modes to the outside using a variety of input-output formalisms [150, 151]), but rather considers the global modes occupying all the Hilbert space. These global modes behave as uncoupled quantum harmonic oscillators with a Hamiltonian of the form

$$\hat{H} = \int_0^\infty d\omega\, \hbar\omega \left(\hat{a}_\omega^\dagger \hat{a}_\omega + \frac{1}{2}\right), \tag{6.6}$$

where the $1/2$ term is usually removed to renormalise the zero-point energy of the field.

To take into account the interaction of the field with an atom localised between the mirrors, one would like:

1. To derive an effective Hamiltonian and master equations accounting for the dynamics inside of the cavity;
2. To describe the leakage of the photons from the cavity;
3. To characterise the photons leaking out of the cavity.

For this, we derive the Hamiltonian including the global field and the atom within the cavity. The presence of the atom from the outset makes the calculations relatively simpler than introducing it later, as shown in [150], since the atom, localised in space and interacting with the global modes $\hat{a}_\omega$, leads to a mode-selective behaviour of the overall system.

Let us assume that a point-like two-level atom with states $|g\rangle$ and $|e\rangle$ separated in energy by $\hbar\omega_A$, is positioned at $x = x_A$, between a perfect, mirror placed at $x = -\ell_c$ and a partially transparent dielectric mirror positioned at the origin. Here, $-\ell_c < x_A < 0$, where ℓ_c is the geometric length of the cavity. The electric field at the position of the atom can be written by evaluating Eq. (6.4) at $x = x_A$, and we consider a field-atom dipolar interaction:

$$\hat{V} = -\hat{d}\hat{E}\left(x_A\right), \tag{6.7}$$

where $\hat{d} = d\hat{\sigma}_+ + d^*\hat{\sigma}_-$ is the dipole moment of the atom, $\hat{\sigma}_+ = |e\rangle\langle g|$ and $\hat{\sigma}_- = |g\rangle\langle e|$. By applying the rotating wave approximation, the interaction terms read:

$$\hat{V} = i\hbar \int_0^{+\infty} d\omega \left(\eta_\omega \hat{\sigma}_+ \hat{a}_\omega - \eta_\omega^* \hat{a}_\omega^\dagger \hat{\sigma}_-\right), \tag{6.8}$$

with a coupling strength given by:

$$\eta_\omega = \sqrt{\frac{\omega}{2\hbar\epsilon_0}}\, d\,\Phi_{\omega,\mathrm{in}}(x_A). \tag{6.9}$$

Therefore, the total Hamiltonian of the atom-cavity global system is of the form

$$\hat{H} = \hbar\omega_A \hat{\sigma}_+ \hat{\sigma}_- + \int_0^{+\infty} d\omega \hbar\omega\, \hat{a}_\omega^\dagger \hat{a}_\omega + i\hbar \int_0^{+\infty} d\omega \Big(\eta_\omega \hat{\sigma}_+ \hat{a}_\omega - \eta_\omega^* \hat{a}_\omega^\dagger \hat{\sigma}_-\Big), \tag{6.10}$$

where the first term corresponds to the energy of the atom, the second term to the energy of the global electromagnetic field and the third term the interaction of this field with the atom placed between the mirrors.

6.3 Calculation of field modes in cavities

In order to derive an effective Hamiltonian describing the dynamics of the open atom-cavity system, we need to derive an effective atom-cavity coupling strength from Eq. (6.9). Therefore, it is necessary to find the modes Φ_ω that satisfy the orthonormalisation condition Eq. (6.2). We perform this calculation taking into account the structure of the partially transparent mirror of the cavity. First, we will examine the propagation of light in a cavity with a thin single-layered mirror and then build upon it to describe the case of multilayered stacks.

Let us model a cavity of length ℓ_c, as shown in Fig. 6.1. For the sake of simplicity, we assume that such a cavity has a perfect mirror on the left side, positioned at $x = -\ell_c$, and a partially transparent dielectric placed at the origin, with a real refractive index n_1 and a thickness δ. The dielectric layer thickness has been designed to support a target wavelength λ_0. In this structure, the spatial distribution of the electromagnetic field mode

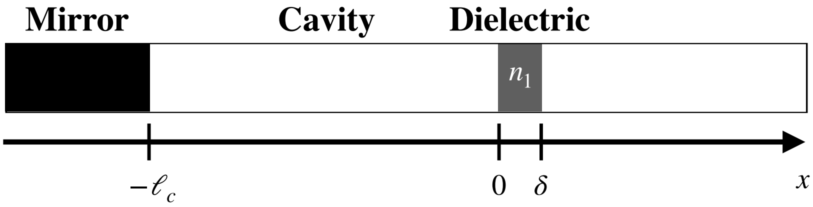

Figure 6.1: Description of the single-layered cavity model. A perfect mirror stands at $x = -\ell_c$, delimiting a cavity of length ℓ_c with a partially transparent dielectric material from $x = 0$ to $x = \delta$.

$\Phi_\omega(x)$ with frequency $\omega = 2\pi c/\lambda$ is described by the Helmholtz equation (6.1), with a relative permittivity structure of the form

$$\epsilon_r(x) = \begin{cases} 1 & x \in [-\ell_c, 0] \cup [\delta, \infty) \\ n_1^2 & x \in (0, \delta) \end{cases} . \tag{6.11}$$

Under these conditions, Helmholtz's equation is solved by a superposition of plane waves of the form

$$\Phi_\omega(x) = A_+ e^{i\frac{\omega}{c}\sqrt{\epsilon_r(x)}x} + A_- e^{-i\frac{\omega}{c}\sqrt{\epsilon_r(x)}x}. \tag{6.12}$$

The distinct solutions are then stitched together by the condition that $\Phi_\omega(x)$ and its derivative must ensure continuity throughout the points of discontinuity of $\epsilon_r(x)$, thus fixing the values of the coefficients A_+ and A_- for every region. For a single-layered stack, the solution has the form

$$\Phi_\omega(x) = \Phi_{\omega,\mathrm{in}}(x)\,\chi_{[-\ell_c,0]} + \Phi_{\omega,\mathrm{stack}}(x)\,\chi_{(0,\delta)} + \Phi_{\omega,\mathrm{out}}(x)\,\chi_{[\delta,\infty)}, \tag{6.13}$$

following the convention defined by Eq. (6.3). Here, $\chi_{\mathcal{D}}$ represents the indicator function within a domain $\mathcal{D} \subset \mathbb{R}$, i.e.,

$$\chi_{\mathcal{D}}(x) = \begin{cases} 1 & x \in \mathcal{D}, \\ 0 & \text{otherwise.} \end{cases}$$

The complete set of orthonormalised modes, described in the three regions, has the following form:

$$\begin{aligned}
\Phi_{\omega,\text{in}}(x) &= \frac{2i}{\sqrt{2\pi c\mathcal{A}}} e^{i\frac{\omega}{c}\ell_c} T(\omega)\sin\left[\frac{\omega}{c}(x+\ell_c)\right], \\
\Phi_{\omega,\text{stack}}(x) &= \frac{1}{\sqrt{2\pi c\mathcal{A}}} e^{i\frac{\omega}{c}\ell_c} \frac{T(\omega)}{1+r_1}\left[(e^{i\frac{\omega}{c}\ell_c} - r_1 e^{-i\frac{\omega}{c}\ell_c})e^{i\frac{\omega}{c}n_1 x} + (r_1 e^{i\frac{\omega}{c}\ell_c} - e^{-i\frac{\omega}{c}\ell_c})e^{-i\frac{\omega}{c}n_1 x}\right], \\
&\qquad\qquad\qquad\qquad\qquad\qquad\qquad\qquad\qquad\qquad\qquad\qquad\qquad\qquad (6.14) \\
\Phi_{\omega,\text{out}}(x) &= \frac{1}{\sqrt{2\pi c\mathcal{A}}}\left(e^{2i\frac{\omega}{c}\ell_c}\frac{T(\omega)}{T^*(\omega)} e^{i\frac{\omega}{c}x} - e^{-i\frac{\omega}{c}x}\right),
\end{aligned}$$

where $\mathcal{A}$ is the transverse area of the mode (a quantity which is calculated when the mode is normalised in three dimensions), r is the single-layer reflectivity

$$r_1 = \frac{n_1 - 1}{n_1 + 1}, \tag{6.15}$$

and $T(\omega)$ is the cavity spectral response function, which describes the ratio of intensities between the inside and outside of the cavity with respect to a particular frequency ω:

$$T(\omega) = \frac{t(\omega)}{1 + r(\omega)e^{2i\frac{\omega}{c}L_1}}. \tag{6.16}$$

Here, $L_1 = (\ell_c + \frac{\delta}{2})$. $T(\omega)$ depends on the single layer spectral transmission $t(\omega)$ and reflection $r(\omega)$ functions [147]:

$$t(\omega) = \frac{(1-r_1^2)e^{i(n_1-1)\frac{\omega}{c}\delta}}{1 - e^{2in_1\frac{\omega}{c}\delta}r_1^2}, \tag{6.17}$$

$$r(\omega) = \frac{r_1(e^{2in_1\frac{\omega}{c}\delta} - 1)}{1 - e^{2in_1\frac{\omega}{c}\delta}r_1^2} e^{-i\frac{\omega}{c}\delta} = |r(\omega)|\, e^{i\Phi_r(\omega)}, \tag{6.18}$$

which are complex and satisfy the beam splitter relations:

$$|t(\omega)|^2 + |r(\omega)|^2 = 1, \tag{6.19}$$

$$r^*(\omega)t(\omega) + t^*(\omega)r(\omega) = 0. \tag{6.20}$$

The squared norm of $T(\omega)$ can be decomposed as a sum of Lorentzian-like functions, having the form

$$|T(\omega)|^2 = \sum_{n=-\infty}^{+\infty} \frac{c}{2L_1} \frac{\gamma_1(\omega)}{(\omega - \tilde{\omega}_m(\omega))^2 + \left(\frac{\gamma_1(\omega)}{2}\right)^2}, \tag{6.21}$$

where

$$\gamma_1(\omega) = -\frac{c}{L_1} \ln|r(\omega)|, \tag{6.22}$$

$$\tilde{\omega}_m = \frac{\pi c}{L_1} m - \frac{c}{2L_1}(\Phi_r(\omega) + \pi). \tag{6.23}$$

In the high-finesse limit (reached when assuming a fictitious dielectric with a high refractive index), the reflection coefficient becomes $r(\omega) = r_1 e^{-i(\pi + \frac{\omega}{c}\delta)}$, i.e $\Phi_r(\omega) = -(\pi + \frac{\omega}{c}\delta)$, which tends to $-\pi$ in the limit of a negligible width δ of the dielectric, recovering the expression for a cavity with negligibly thin mirrors. Additionally, for cavities having $\delta \ll \ell_c$, such that $L_1 \approx \ell_c$, the squared norm of the response function can be approximated as follows:

$$|T(\omega)|^2 \approx \sum_{m=-\infty}^{\infty} \frac{c}{2\ell_c} \frac{\Gamma_m}{(\omega - \tilde{\omega}_m)^2 + \left(\frac{\Gamma_m}{2}\right)^2}, \tag{6.24}$$

where

$$\Gamma_m = \gamma_1(\omega_m) = -\frac{c}{\ell_c} \ln|r(\omega_m)|, \tag{6.25}$$

$$\tilde{\omega}_m = \omega_m + \frac{c}{2\ell_c}(\pi - \phi_r(\omega_m)), \tag{6.26}$$

with $\omega_m = m\pi c/\ell_c$. Under these conditions, the terms in the sum in Eq. (6.24) become Lorentzian, with each term centred around the resonance frequency $\tilde{\omega}_m$ and well separated from each other. Taking this into account we can now write the cavity response function as

$$T(\omega) \approx \sum_{m=-\infty}^{\infty} \sqrt{\frac{\Gamma_m c}{2\ell_c}} \frac{1}{(\omega - \tilde{\omega}_m) + i\frac{\Gamma_m}{2}} = \sum_{m=-\infty}^{\infty} T_m(\omega), \tag{6.27}$$

where every Lorentzian $T_m(\omega)$ is so narrow that it does not overlap with the other

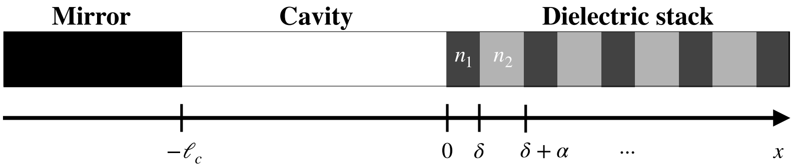

Figure 6.2: Description of the considered model. A perfect mirror stands at $x = -\ell_c$, delimiting a cavity of length ℓ with an alternating dielectric stack standing from zero.

Lorentzians $T_{m'}(\omega)$. With this result, it is possible to write the coupling strength (6.9) between the atom and a cavity with one thin dielectric mirror in the form:

$$\eta_\omega = \sum_{m=-\infty}^{\infty} i\sqrt{\frac{\Gamma_m \omega}{2\pi\hbar\epsilon_0 \ell_c \mathcal{A}}}\, d\, e^{i\frac{\omega}{c}\ell_c} \sin\left[\tfrac{\omega}{c}(x_A + \ell_c)\right] \frac{1}{(\omega - \tilde{\omega}_m) + i\frac{\Gamma_m}{2}}, \quad (6.28)$$

In the high-finesse case considered here, $\ell_c \mathcal{A}$ happens to be identical to the mode volume determined by the geometric parameters of the cavity: its mirror separation (or geometric length, ℓ_c), and mirror area, $\mathcal{A}$. However, we emphasise that the mode volume was not introduced by normalising the field in a perfect resonator of length ℓ_c. Instead, it is a result of the finite width of the resonances in Eq. (6.24). To this respect, recovering ℓ_c only appears in the case of a long, high-finesse resonator and this may not prevail when such condition is not met, as we shall demonstrate in the following discussion.

6.4 Field modes for cavities with multilayer stacks

Now, we perform the description of a multilayered stack: We extend our discussion to consider an alternating stack of two dielectric materials. As before, the first layer has a width δ and a refractive index n_1, and the second one a width α and a refractive index n_2. The stack has $2N-1$ layers: $N-1$ pairs of dielectrics and one additional layer of index n_1. Because of this, the first and last layers of the stack have the higher refractive index ($n_1 > n_2$)[153]. We do not include in our model a substrate on which the dielectric coating is deposited, which would normally correspond to a final, significantly thicker, layer of low index material. An updated cavity model is shown in Fig. 6.2 and the corresponding relative permittivity is given by:

$$\epsilon_r(x) = \begin{cases} 1 & -\ell_c < x \leq 0 \\ n_1^2 & j_1(\delta+\alpha) < x \leq j_1(\delta+\alpha)+\delta \\ n_2^2 & (j_2-1)(\delta+\alpha)+\delta < x \leq j_2(\delta+\alpha) \\ 1 & x > N(\delta+\alpha)-\alpha \end{cases}, \tag{6.29}$$

where $j_1 \in \{0,1,2,...,N-1\}$ and $j_2 \in \{1,2,...,N-1\}$. The cavity is designed such that its fundamental longitudinal mode is at wavelength λ_0, which is also used to specify the quarter wave dielectric layer optical thickness: $\delta = \lambda_0/4n_1$ and $\alpha = \lambda_0/4n_2$. For simplicity, we will further consider $n_2 = 1$. Again, by following the continuity of the field and its derivative, we solve Helmholtz equation (6.1) and find that the mode can be described in terms of the following functions:

$$B_0(\omega,x) = e^{i\frac{\omega}{c}(x+\ell_c)}, \tag{6.30}$$

$$B_j(\omega,x) = \begin{cases} \frac{1}{1-r_1}\left(B_{j-1}(\omega,x_{2,j})+r_1B^*_{j-1}(\omega,x_{2,j})\right)e^{i\frac{\omega}{c}\left(x-x_{2,j}\right)} & j \text{ even,} \\ \frac{1}{1+r_1}\left(B_{j-1}(\omega,x_{1,j})-r_1B^*_{j-1}(\omega,x_{1,j})\right)e^{i\frac{\omega}{c}n_1\left(x-x_{1,j}\right)} & j \text{ odd,} \end{cases} \tag{6.31}$$

where

$$x_{1,j} = \frac{j-1}{2}(\delta+\alpha), \tag{6.32}$$

$$x_{2,j} = \frac{j}{2}(\delta+\alpha)-\alpha. \tag{6.33}$$

The solution to the Helmholtz equation is then given by

$$\Phi_\omega(x) = \sum_{j=0}^{2N} CA_j(\omega,x)\chi_{\Omega_j}, \tag{6.34}$$

where j runs over the $2N-1$ possible layers, labelled as $\Omega_j \subset \mathbb{R}$, C is a normalisation factor common to all terms and $A_j(\omega,x) = B_j(\omega,x) - B^*_j(\omega,x)$. $A_0(\omega,x)$ corresponds to the mode propagating between the two mirrors and $A_{2N}(\omega,x)$ is the mode corresponding to the outgoing wave. Additionally, Ω_j has the form

$$\Omega_0 = [-\ell_c, 0], \tag{6.35}$$

$$\Omega_j = \begin{cases} \left[x_{2,j}, x_{2,j}+\alpha\right], & j \text{ even}, \\ \left[x_{1,j}, x_{1,j}+\delta\right], & j \text{ odd}. \end{cases} \tag{6.36}$$

Since we consider propagations of the field outside the dielectric stack to occur in both directions, for a mismatch of the light propagation frequency ω, with the stack design frequency $\omega_0 = 2\pi c/\lambda_0$, the intensity of the mode can decay exponentially by either exiting the cavity or passing through the stack from outside the cavity. In some cases, the mode passing through the stack can achieve extremal points of intensity within the dielectric-layer stack. Some examples of different modes with varying values of ω are shown in Fig. 6.3.

After a mode has been described in the form of Eq. (6.34), it is important to consider an effective transmissivity, reflectivity and response for a multilayered cavity, resembling Eq. (6.14). Following the normalisation of the modes in (6.34), the inside and outside modes have the form

$$\Phi_{\omega,\text{in}}(x) = 2ie^{i\frac{\omega}{c}\ell_c}\mathcal{T}(\omega)\sin\left[\frac{\omega}{c}(x+\ell_c)\right], \tag{6.37}$$

$$\Phi_{\omega,\text{out}}(x) = e^{2i\frac{\omega}{c}\ell_c}\frac{\mathcal{T}(\omega)}{\mathcal{T}^*(\omega)}e^{i\frac{\omega}{c}x} - e^{-i\frac{\omega}{c}x}. \tag{6.38}$$

Here, $\mathcal{T}(\omega)$ is the field amplitude ratio of the multilayered cavity, which has the form

$$\mathcal{T}(\omega) = \frac{e^{-i\frac{\omega}{c}(\ell_c+(N-1)(\delta+\alpha))}}{B^*_{2N-2}(\omega)}\frac{t(\omega)}{1+e^{i\frac{\omega}{c}\delta}e^{i\phi_B(\omega)}r(\omega)}, \tag{6.39}$$

where $\phi_B(\omega) = \arg\Big(B_{2N-2}(\omega,x_{1,2N-1})/B^*_{2N-2}(\omega,x_{1,2N-1})\Big)$. Here, $t(\omega)$ and $r(\omega)$ remain the same as for the single layer case. By indexing the response functions in terms of the number N of layers with index n_1, it can be shown that the response functions are

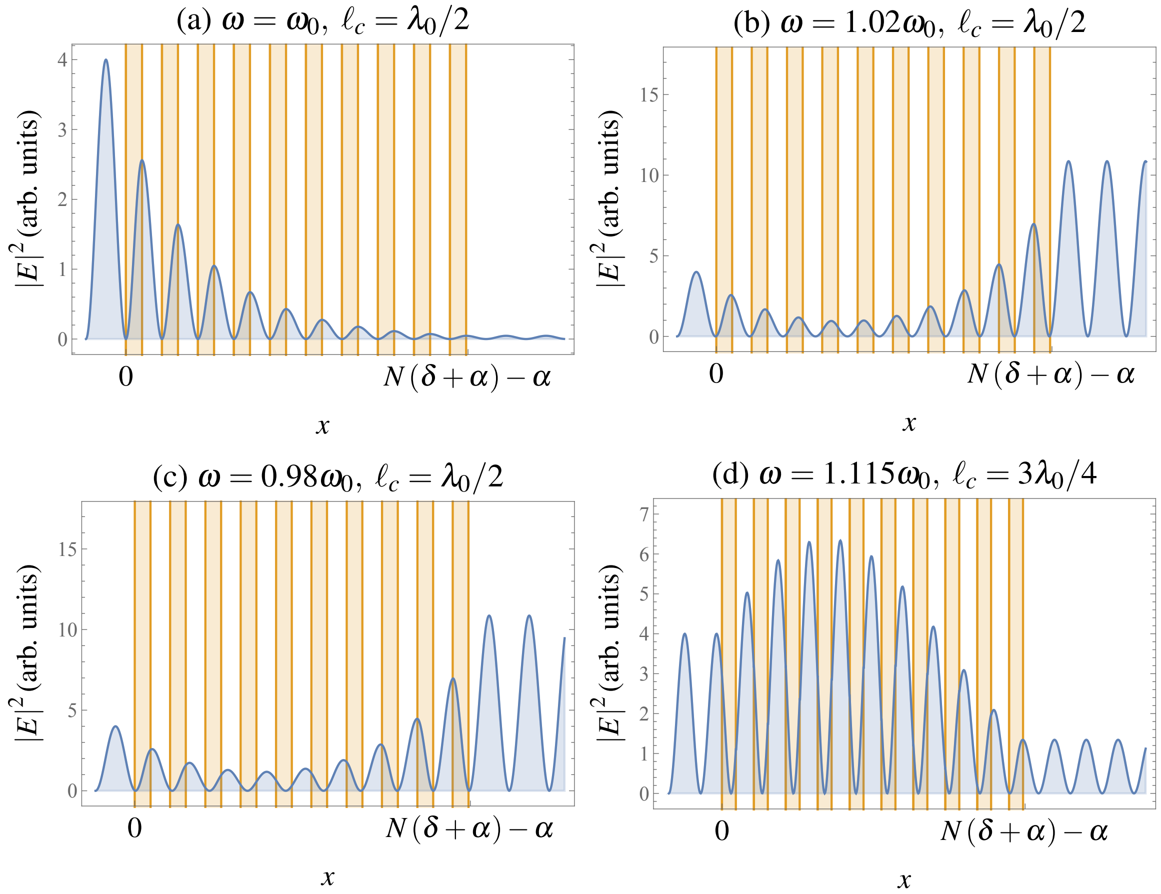

Figure 6.3: Mode propagation of a wave of wavelength λ, for a cavity with a multilayered stack with an index of $n_1 = 1.25$. A perfect mirror stands at $x = -\ell_c$, forming a cavity of length ℓ_c with an alternating dielectric stack of 21 alternating layers of width $\delta = \lambda_0/4n_1$ and $\alpha = \lambda_0/4n_2$ (n_2 is taken to be 1). The propagation frequency $\omega = 2\pi c/\lambda$ is varied to observe the mode propagation. In (a), the case when $\ell_c = \lambda_0/2$ and ω exactly matches with the cavity design resonance frequency ω_0 is shown, obtaining the strongest confinement of light inside of the cavity. In (b) and (c), we can see how the intensity changes when the propagating light is slightly off resonance. Finally, in (d) we increase the cavity length to reach $\ell_c = 3\lambda_0/4$ and observe that we achieve resonance coupling when $\omega = 1.1022\omega_0$. Moreover, we can see that in this case the intensity of the light within the layer stack exceeds the intensity of the light inside of the cavity.

connected recursively:

$$\frac{e^{-i\frac{\omega}{c}(\ell_c+(N-1)(\delta+\alpha))}}{B^*_{2N-2}(\omega)} = \mathcal{T}_{N-1}(\omega), \tag{6.40}$$

such that

$$\mathcal{T}_N(\omega) = \mathcal{T}_{N-1}(\omega)\,\frac{t(\omega)}{1+e^{i\frac{\omega}{c}\delta}e^{i\phi_B(\omega)}r(\omega)}.$$

Fig. 6.4 shows a series of different cavity response functions for varying numbers of layer stacks and cavity lengths. Here, our model is seen to exhibit the standard behaviour of an optical cavity by showing a decreased linewidth as the number of layers increases, as would be expected from increased mirror reflectivity. Furthermore, the free spectral range of the cavity clearly decreases as its length is increased.

Just as in the case of the single-layered cavity, we can also write the square modulus of the response function as a sum of Lorentzian-like functions, analogous to the one in Eq. (6.21):

$$|\mathcal{T}(\omega)|^2 = \sum_{m=-\infty}^{\infty}\left(\frac{c}{\delta|B_{2N-2}(\omega)|^2}\frac{\gamma_N(\omega)}{(\omega-\tilde{\omega}_m(\omega))^2+\left(\frac{\gamma_N(\omega)}{2}\right)^2}\right), \tag{6.41}$$

where

$$\gamma_N(\omega) = -c\frac{\ln|r(\omega)|}{\delta/2}, \tag{6.42}$$

$$\tilde{\omega}_m = \frac{c\pi}{\delta/2}m - c\frac{(\phi_r(\omega)+\phi_B(\omega)+\pi)}{\delta}. \tag{6.43}$$

The term $\phi_B(\omega)$ in the expression of $\tilde{\omega}_m$ accounts for the multilayer nature of the mirror. In the single-layered case, this has the simple, analytical form $\phi_{B_1}(\omega) = 2\ell_c\omega/c$, which leads to the expressions in Eqs. 6.22 and 6.23.

As we can see from Fig. 6.4, the multilayer structure leads to a narrowly peaked Lorentzian response function. From the individual Lorentzian peaks, it is possible to obtain numerical values for the cavity transmission parameters $L_N^{(m)}$, $\gamma_N^{(m)}$ and $\omega_N^{(m)}$ by performing a numerical fit of $|\mathcal{T}(\omega)|^2$:

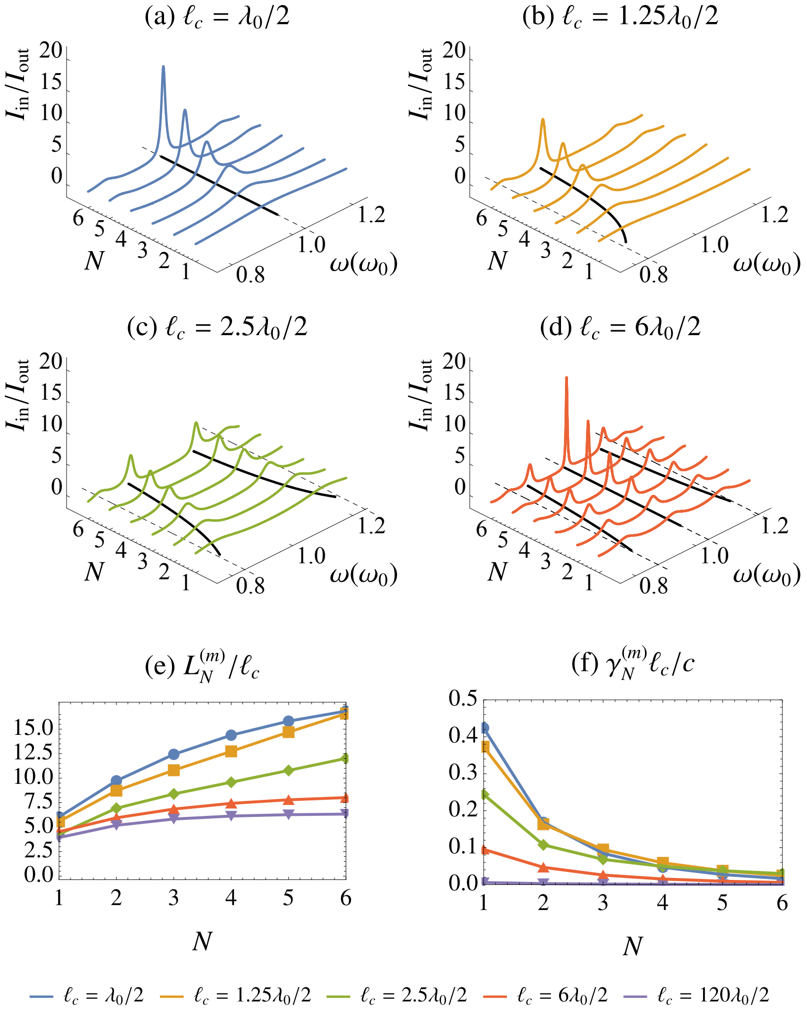

Figure 6.4: Cavity inside-outside intensity ratio, $I_{\text{in}}/I_{\text{out}}$, as a function of the angular frequency of the light and the number N of layers with index n_1, for a cavity with a multilayered stack with a refractive index $n_1 = 1.25$. A perfect mirror stands at $x = -\ell_c$, and there is an alternating dielectric stack with a varying number of N layers of width $\delta = \lambda_0/4n_1$ and $N-1$ layers of width $\alpha = \lambda_0/4n_2$ (where n_2 is taken to be 1). Both the number of dielectric layers and the spacing of the cavity are varied to observe different sorts of cavity response functions: (a) shows $\ell_c = \lambda_0/2$, (b) $\ell_c = 1.25\lambda_0/2$, (c) $\ell_c = 2.5\lambda_0/2$, and (e) $\ell_c = 6\lambda_0/2$,. All of these can be decomposed as a sum of Lorentzian functions in ω. The dashed lines correspond to cavity classical resonances: $\omega_m = m\pi c/\ell_c$, where m is the number of antinodes between the mirrors. The black, solid lines correspond to $\omega_N^{(m)}$, the peak responses followed by the modes. These do not coincide with ω_m and are strongly dependent on the number of layers. (e) and (f) also follow the values of the coupling parameters, $L_N^{(m)}$and $\gamma_N^{(m)}$ for different values of ℓ_c, with $L_N^{(m)} \to \ell_c$ for longer cavities. These values arise from the calculated Lorentzian transmissions and correspond to the eventual coupling parameters from Eq. 6.54.

$$|\mathcal{T}(\omega)|^2 = \sum_m \frac{c}{2L_N^{(m)}} \frac{\gamma_N^{(m)}}{\left(\omega - \omega_N^{(m)}\right)^2 + \left(\frac{\gamma_N^{(m)}}{2}\right)^2}. \tag{6.44}$$

For reasons explained below, $L_N^{(m)}$ can be called the coupling factor cavity length.

In the case of a single-layered mirror, we obtain the individual Lorentzians by evaluating the parameters in Eqs. 6.22 and 6.23 at the resonance frequencies $\tilde{\omega}_m$. Here, however, we cannot follow the same procedure due to the complicated nature of the coefficient $|B_{2N-2}(\omega)|^2$. Therefore, we apply a numerical fitting to recover the accuracy of the procedure described above.

We will now examine what happens when we vary the spacing between the mirrors. By taking into account the multilayer structure of the mirror, we also observe resonance frequency shifts from the expected resonances, i.e. for a cavity having a mirror spacing ℓ_c, the expected resonance frequency would be at

$$\omega_m = 2\pi c/\lambda_m = \frac{\pi m c}{\ell_c}, \tag{6.45}$$

where m is the number of antinodes fitting between the mirrors. However, the resonance frequencies that we obtain with a multilayered structure, in general, do not match the values of ω_m described above (see Fig. 6.5). In other words, if in the multilayered case we write $\omega_{\text{eff}} = \omega_N^{(m)} = \pi m \left(c/\ell_{\text{eff}}\right)$ for the resonance frequencies, then, in general ℓ_{eff} is different from ℓ_c. Importantly ℓ_{eff} is only the same as ℓ_c whenever $\ell_c = p\lambda_0/2$, where p is an integer number, then. Moreover, the shorter the cavity, the greater the difference between ω_{eff} and ω_m. Moreover, ℓ_{eff} is also different from the coupling factor cavity length, $L_N^{(m)}$, obtained from the cavity response function.

Since each term in Eq. (6.44) corresponds to a well separated single Lorentzian at a resonance frequency $\omega_N^{(m)}$, we can decompose the cavity response function as

$$\mathcal{T}(\omega) \approx \sum_m \sqrt{\frac{c}{2L_N^{(m)}}} \frac{\sqrt{\gamma_N^{(m)}}}{\left(\omega - \omega_N^{(m)}\right) + i\frac{\gamma_N^{(m)}}{2}} = \sum_m \mathcal{T}_m(\omega). \tag{6.46}$$

Unlike the single layer case, this expression for the response function is general; being applicable to cavities of any length, dielectric layer number and refractive index n_1. It is now possible to write the coupling strength (6.9) for this case:

$$\eta_\omega = \sum_{m=-\infty}^{\infty} i\sqrt{\frac{\gamma_N^{(m)}\omega}{2\hbar\epsilon_0 L_N^{(m)}\mathcal{A}}}d\,e^{i\frac{\omega}{c}\ell_c}\sin\left[\tfrac{\omega}{c}(x_A+\ell_c)\right]\frac{1}{\left(\omega-\omega_N^{(m)}\right)+i\frac{\gamma_N^{(m)}}{2}} \tag{6.47}$$

If we compare this result with the single-layer case of Eq. (6.28), we can see that the expressions are the same, with the exception that for the multilayer case we have $L_N^{(m)}$ instead of ℓ_c and $\gamma_N^{(m)}$ instead of Γ_m. As the value of $L_N^{(m)}$ may not necessarily correspond to ℓ_c, this parameter is given the name of coupling factor cavity length. Similarly, if we interpret the product $L_N^{(m)}\mathcal{A}$ in the pre-factor as the mode volume, it is no longer defined through the geometric length of the cavity, due to the discrepancy between $L_N^{(m)}$ and ℓ_c.

Over the width $\gamma_N^{(m)}$ of a single Lorentzian, ω is close to $\omega_N^{(m)}$ and varies very slowly, therefore we can further approximate the mode selective coupling $\eta_{\omega,m}$ as:

$$\eta_{\omega,m} \approx i\sqrt{\frac{\omega_N^{(m)}}{\hbar\epsilon_0 L_N^{(m)}\mathcal{A}}}d\,e^{i\frac{\omega}{c}\ell_c}\sin\left[\tfrac{\omega}{c}(x_A+\ell_c)\right]\sqrt{\frac{\gamma_N^{(m)}}{2\pi}}\frac{1}{\left(\omega-\omega_N^{(m)}\right)+i\frac{\gamma_N^{(m)}}{2}}. \tag{6.48}$$

6.5 Calculation of an effective Hamiltonian for cavities with multilayer stacks

Previously, we derived a Hamiltonian describing the global closed system consisting of an atom, cavity and environment. Now, our goal is to extract an effective Hamiltonian to describe the dynamics of the open atom-cavity system. This extraction has been studied in the literature for the single-layer case [150]. Given that the quantum information processing, retrieval and storage of single photons all happen within the limited scenario of a single excitation within the cavity [24], in the proceeding analysis we limit the Hilbert space to a subspace containing the excited atom state $|e,0\rangle$ and the single excitation of the cavity in a superposition of frequency modes around the resonance frequency $\omega_N^{(m)}$:

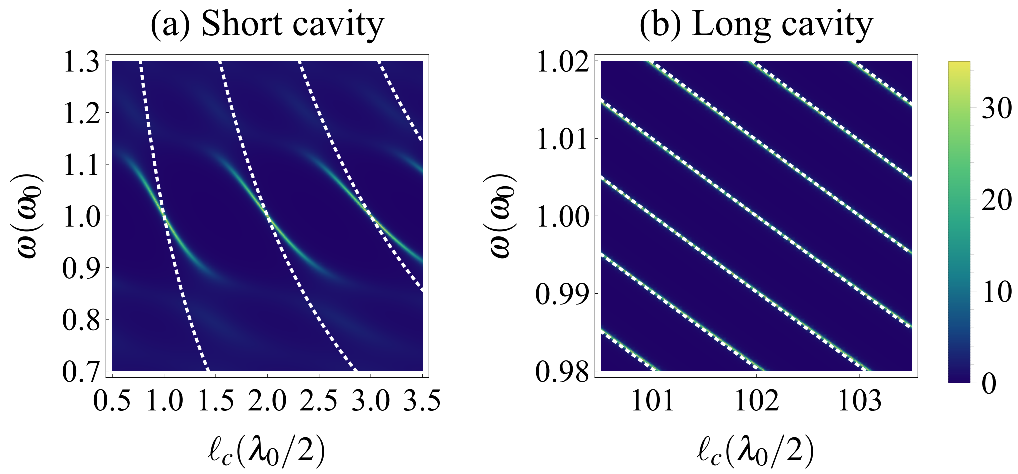

Figure 6.5: Calculated Inside/Outside intensity ratio using the electromagnetic propagation of the mode versus $\pi mc/\ell_c$ shown in white, dotted lines. When cavities are very short, the mismatch is appreciable and the maximum inside/outside ratio lines predicted classically differ significantly with respect to the mode prediction. We can see that, only at the points where we have a cavity of length $\ell_c = p\lambda_0/2$, where p is an integer, the predicted and actual lines match.

$|g, 1_m\rangle$. To write the effective Hamiltonian for such a system we define the following operator:

$$\hat{a}_m = \frac{1}{g_m}\int_0^\infty d\omega\, \eta_{\omega,m}\, \hat{a}_\omega, \tag{6.49}$$

which satisfies the commutation relations:

$$[\hat{a}_m, \hat{a}^\dagger_{m'}] = \delta_{mm'},$$
$$[\hat{a}_m, \hat{a}_{m'}] = 0.$$

The definition (6.49) allows one to transform the continuous model (6.10) into a discrete one, and to define the single photon excitation around the resonance frequency $\omega_N^{(m)}$ as $|1_m\rangle = \hat{a}^\dagger_m|0\rangle$.

It can be shown that g_m is a normalisation constant given by (see the Appendix A):

$$g_m = i\sqrt{\frac{\omega_N^{(m)}}{\hbar\epsilon_0 L_N^{(m)}\mathcal{A}}}\,d\,e^{i\frac{\omega_N^{(m)}}{c}\ell_c}\sin\left[\frac{\omega_N^{(m)}}{c}(x_A+\ell_c)\right] + \mathcal{O}\left(\epsilon^2\right), \tag{6.50}$$

up to an error of the order ϵ^2, where $\epsilon = \gamma_N^{(m)} \frac{x_A+\ell_c}{c}$. The width $\gamma_N^{(m)}$ decreases with a greater number of layers and cavity length, hence ϵ becomes smaller (see Fig. 6.4) and the approximation is well validated.

Assuming that only one of the cavity modes at $\omega_N^{(m)}$ is close to the resonance frequency ω_A of the atom, all other modes can be safely disregarded and the effective Hamiltonian then reads:

$$\hat{H}_{\text{eff}} = \hbar\omega_A\hat{\sigma}_+\hat{\sigma}_- + \left(\hbar\omega_N^{(m)} - i\hbar\frac{\gamma_N^{(m)}}{2}\right)\hat{a}_m^\dagger a_m + i\hbar g_m\hat{\sigma}_+\hat{a}_m - i\hbar g_m^*\hat{\sigma}_-\hat{a}_m^\dagger, \tag{6.51}$$

where $\omega_N^{(m)} - \omega_A \ll \omega_N^{(m)}$, g_m is the coupling of a single cavity mode $\omega_N^{(m)}$ with the atom and $\gamma_N^{(m)}$ is the width of Lorentzian centred at the resonance frequency $\omega_N^{(m)}$. This non-Hermitian Hamiltonian is a consequence of tracing out the environment to stay only with the dynamics of the cavity.

The expression (6.50) looks similar to the atom-cavity coupling for a perfect cavity, i.e., if we write the perfect cavity Hamiltonian with zero boundary conditions at the mirrors we obtain:

$$g_m = i\sqrt{\frac{\omega_m}{\hbar\epsilon_0\ell_c\mathcal{A}}}\,d\,e^{i\frac{\omega_m}{c}\ell_c}\sin\left[\tfrac{\omega_m}{c}(x_A+\ell_c)\right], \tag{6.52}$$

which is different from (6.50) by an error factor $\mathcal{O}\left(\epsilon^2\right)$, again, due to the mismatch between ℓ_c and $L_N^{(m)}$ and ω_m and $\omega_N^{(m)}$.

For the more general case, when the atom is not necessarily on resonance with the cavity, (i.e. we consider the states $|e,0\rangle$, $|g,1\rangle$, as well as $|e,1\rangle$ and $|g,0\rangle$), it can be shown that the Hamiltonian (6.51) becomes:

$$\begin{aligned}\hat{H}_{\text{eff}} = \hbar\omega_A\widehat{\sigma}_+\widehat{\sigma}_- + \hbar\sum_m\left(\omega_N^{(m)} - i\frac{\gamma_N^{(m)}}{2}\right)\widehat{a}_m^\dagger\widehat{a}_m + ig_m\widehat{\sigma}_+\widehat{a}_m \\ - ig_m^*\widehat{\sigma}_-\widehat{a}_m^\dagger + i\underline{g}_{\,m}\widehat{\sigma}_-\widehat{a}_m - i\underline{g}^*_{\,m}\widehat{\sigma}_+\widehat{a}\dagger_m,\end{aligned} \tag{6.53}$$

where

$$\underline{g}_m = i\sqrt{\frac{\omega_N^{(m)}}{\hbar\epsilon_0 L_N^{(m)}\mathcal{A}}}\, d^* e^{i\frac{\omega_N^{(m)}}{c}\ell_c} \sin\left[\frac{\omega_N^{(m)}}{c}(x_A+\ell_c)\right] + O\left(\epsilon^2\right). \tag{6.54}$$

6.6 Conclusions

We have examined light-matter interaction in optical cavities delimited by multilayered dielectric mirrors using a model where no assumptions over the longitudinal constraints of the field have been made. The analysis of the multilayer structure allowed us to perform a more realistic description of the effective cavity length and corresponding mode volume.

The effective cavity length ℓ_{eff}, as defined in the literature [143, 154, 155], determines the cavity resonance and, as we have shown in this chapter, does not correspond to the coupling factor cavity length $L_N^{(m)}$ used for determining the strength of the cavity-matter coupling. Due to the overlap of several Lorentzians in $|\mathcal{T}(\omega)|^2$ and to the propagation of the mode within the dielectric stacks, we have found that these two lengths may not correspond to each other whenever a multilayer structure is taken into consideration. Additionally, the resonance frequencies through which ℓ_{eff} is defined no longer coincide with the expected resonances at integer multiples of $c/(2l_c)$. In other words, ℓ_{eff} is different from the geometric cavity length ℓ_c unless the latter is an integer multiple of $\lambda_0/2$, where λ_0 is the stack design wavelength. A pronounced side effect of this discrepancy is that the most common approach [45] for determining a cavity length by means of measuring its free-spectral range is bound to fail for very short cavities. This has been observed, for example, for optical nanofibre cavities [156]. Indeed, the actual geometric length of the cavity encompassed between the mirrors might differ substantially, even orders of magnitude, from the one measured using the free spectral range of a cavity, something evidenced by Figure 6.4(e). This difference may be of importance in applications where the cavity spacings used are very short and the mirrors are made of dielectric coatings [157, 158] .

The standard model for light-matter interaction in optical cavities considers the mode volume of the cavity to be the product between the longitudinal extent of the mode (considered to be only the separation between the mirrors) and a factor accounting for the transverse behaviour of the mode [48]. However, here we have shown that this is only valid if the mirrors can be seen as hard mode-delimiting boundaries. Any physical cavity is very different to that respect. The mode penetrates into the dielectric mirror stack, couples to the outside and the light frequency is not quantised in these open systems. However, even though we don't explicitly consider a mode volume, we show that the atom-cavity coupling involves a factor having the unit of volume. Only in the case of a perfect cavity having hard boundaries at the positions of the mirrors, this factor coincides with the geometric definition of the mode volume. In the multilayered case, however, this factor does not necessarily correspond to the geometric volume of the cavity, particularly due to the discrepancy between the geometric length ℓ_c, the effective length ℓ_{eff} and $L_N^{(m)}$.

Specifically, for a cavity with a mirror spacing $\ell_c = \lambda_0/2$, the effective cavity length ℓ_{eff} coincides with ℓ_c, however the coupling factor cavity length does not: $L_{19}^{(1)} \approx 3.06\ell_c$. If we increase the mirror spacing, such that $\ell_c = 1.8\lambda_0/2$, then for the other parameters we obtain: $\ell_{\text{eff}} \approx 0.53\ell_c$ and $L_{19}^{(1)} \approx 2.4\ell_c$. As expected, for longer cavities the discrepancy between these terms decreases, e.g., when $\ell_c = 30.8\lambda_0/2$ we obtain $\ell_{\text{eff}} \approx 0.97\ell_c$ and $L_{19}^{(q)} \approx 1.09\ell_c$, where q is the number of the mode with highest amplitude. This discrepancy between the coupling factor cavity length $L_N^{(m)}$ and geometric cavity length ℓ_c can lead to a Purcell factor different from the one calculated by using a standard approach, especially with short mirror spacings.

Eventually, from the general quantised field we extract an effective Hamiltonian describing an open cavity system. From this we explicitly calculate the atom-cavity coupling rate both for on- and off-resonant behaviour. This quantisation from first principles of more realistic open cavities is a preliminary step for considering the complex dynamics featuring a laser-driven atom in such cavities. Work from our collaborators in Dijon is ongoing to derive microscopic models [159] for controlling photonic states produced from such cavities [96].

We also note that submicrometric confinement of light in (dissipative and dispersive) metallic media gives rise to surface plasmon polaritons that can be used for quantum optics at nanoscale [160]. Albeit these are no multilayered structures, the construction of quantised models taking into account the resulting losses follows a similar approach and is based on a microscopic oscillator model for the medium coupled to the electromagnetic field [161] with a particular care for finite-size media [162, 163].

In the future, we expect the presented method to help us describe the leakage of single photons in the cavity to the environment. Additionally, we consider this chapter and the publication it is derived from [139] to be useful for researchers which use emitters inside of short cavities, where this effect is manifested. Some of the following are potential applications: Coupling of ions [145] and atoms to fibre-tip optical cavities[164], quantum dots[165], NV-centres [142, 157, 166], the use of two different frequencies within a short multilayered cavity [167] and, in general, whenever there is a very short cavity that couples strongly to a discrete quantum emitter. In sum, the substantial deviations from the simple model discussed here would make it impossible to establish strong coupling unless these corrections were considered. Finally, these results could also prove useful for the spectral characterisation of devices with multilayered structures[141].

7

Outlook and conclusions

The goal of this chapter is twofold. The first part will discuss the potential avenues for the improvement of single-photon sources using atoms in high-finesse cavities. The second part will provide concluding remarks to understand the contributions of this work to the greater context of the field.

7.1 Perspectives

In this thesis, we have shown several methods and avenues to improve the efficiency in the production of single photons using atoms in cavities, with the aim of having sources that enable the production of continuous streams of single photons with high efficiency. In this section, we will describe some of the future avenues enabled by this work, with the aim of pushing atom-cavity based single-photon sources to higher limits:

7.1.1 Experimental implementation of repumping methods

So far, an analysis of the methods necessary to improve photon generation efficiency with the stochastic loading of atoms in high-finesse cavities have shown significant theoretical improvements in the generation of continuous streams of single photons. In the near future, we expect to implement the repumping methods presented in Chapter 5, as the required components and devices are already present in the laboratory.

7.1.2 Implementation of high-cooperativity cavities

One of the most important conclusions from Chapter 5 has been that, for the D_2 line of ^{87}Rb, cavities with cooperativities of $C \gtrsim 10$ are already at the limit of photon production efficiency due to the mixing of levels at the detunings and magnetic fields applied. In this sense, new cavity prototypes existing in the laboratory promise to reach the upper limit of photon generation efficiency in the D_2 line. When combined with the novel driving schemes that would permit the generation of polarised single photons without the need for splitting the atomic magnetic structure. The implementation of photon generation schemes using the novel cavity architectures would represent great improvements for these sources. This is especially interesting, as it has been recently seen [109] that entangled multi-photon states generated from a single atom can be more resilient and scalable than those produced by other photonic platforms.

7.1.3 Interfacing of cavities and dipole traps

The most recent cavity designs have been made with the specific intention of interfacing a dipole trap to load an atom within an optical cavity. In view of the fact that the current implementations of single-photon sources rely on the probabilistic loading of atoms in the cavity, an interfacing of a dipole-trapped atom with a cavity would enable the realization of fully deterministic single-photon sources.

Novel designs that enable the loading of atoms in miniaturized pyramid MOTs interfaced with high-cooperativity cavities are being tested by Mark IJspeert and Chloe So.

7.1.4 Cavities resonant to the D_1 line of ^{87}Rb

The D_1 line of ^{87}Rb, with a higher energy separation of its excited levels, would enable a more reliable generation of polarised photons in alternating driving schemes such as the ones discussed in this thesis. This is a challenge in itself because the coupling strengths in the D_1 line are much weaker than those in the D_2 line. Whilst this could be partially compensated using stronger driving fields, a much smaller cavity is required to reach the same coupling strength.

Previous analyses [37, 63] have shown that the generation of single photons on the D_1 line would only be viable when driving the atom near the $\left|\widetilde{\psi}(F' = 1)\right\rangle$ level, but even in this case the current cavity design used for producing polarised photons does not reach the strong coupling regime that would enable a reliable source.

7.1.5 Demultiplexing and $(n > 2)$-photon interference

Complex optical networks require the use of multiple inputs and outputs to produce quantum unitary operations. One example of such networks is a multimode interferometer, in which the input modes are connected via a unitary operation to the output modes.

Previous work in the group has dealt with generating quantum logic operations such as a controlled NOT gate, demonstrated in 2015 [61], as well as examining the time resolved interference of two photons sent through a multimode interferometer [27].

In the future, the group intends to perform similar experiments with multiple single photons. We hope that the combination of the current demultiplexing methods and the novel techniques for improving photon repumping will enable the generation of streams of multiple photons that enable the time resolved interference of multiple photons without relying on random routing, something that can be done for four photons with the current devices in the laboratory, and easily scalable to the time resolved interference of eight photons.

7.1.6 Reabsorption and quantum networks

All elements required to realise a quantum network between atoms in separate cavities are readily available in the laboratory. As mentioned in Chapter 3, the light sources have been made with the specific purpose of simultaneously driving and locking two cavities. Whilst this idea has been implemented by a small set of research groups in the world, the high degree of controllability used in our sources could enable the tailoring of photons that can be easily absorbed by a remote atom in another cavity.

In a similar vein, the idea of entanglement swapping by means of a joint measurement on photons that are themselves entangled with atoms left behind is very promising and in reach with the present setup. It is going to result in a quantum state reduction leaving a pair of entangled atoms behind, and thus represents an elementary quantum network link for establishing remote entanglement.

7.1.7 Photon-bin entanglement

Let us consider the interference of three doubly-humped photons into the input ports of a beam splitter, following the pattern shown in Figure 7.1. Each of these photons is characterised as having a creation operator split into early and late temporal modes, or time bins. Two photons enter the input port A of a beam splitter in modes $\hat{a}^\dagger = \left(\hat{a}_1^\dagger + \hat{a}_2^\dagger\right)/\sqrt{2}$ and $\hat{\hat{a}}^\dagger = \left(\hat{a}_3^\dagger + \hat{a}_4^\dagger\right)/\sqrt{2}$. Here, the subscript associated with each operator corresponds to the time interval in which each photon is meant to appear. Simultaneously, a photon overlapping with the second interval of the first photon and the first interval of the second photon is sent through the input port B: it occupies mode $\hat{b}^\dagger = \left(\hat{b}_2^\dagger + \hat{b}_3^\dagger\right)/\sqrt{2}$.

After passing through a 50:50 beam splitter, the modes will follow the beam splitter relations and occupy modes $\hat{c}^\dagger$ and $\hat{d}^\dagger$: each of the creation operators in mode i will be split such that the output operators are written as

$$\hat{c}_i^\dagger = \frac{a_i^\dagger + b_i^\dagger}{\sqrt{2}}; \hat{d}_i^\dagger = \frac{a_i^\dagger - b_i^\dagger}{\sqrt{2}};$$

It would be possible, following the ideas of Chapter 4, to extend the time resolved

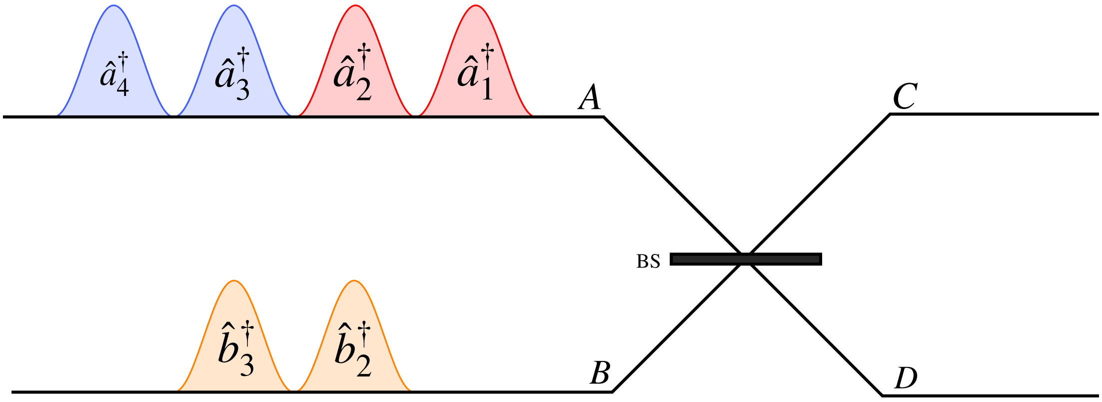

?figurename? 7.1: Interference of three non-simultaneous arriving photons, with the aim of entangling the first and the fourth bin entering through the input port A.

interference of photons on a beam splitter to the interference of three photons. In this case, a partial measurement of the system would enable the generation of an entangled state between two photons emitted on the same rail.

By performing the measurement of the two photons on the central time bins $(2,3)$ that interfere with the first and the second photon on port A, it would be possible to entangle the two photon humps in the first and last bin $(1,4)$. The entanglement would be mediated by the photon in the lower spatial arm, entangling two photon peaks that were never in contact. The measurement outcome would determine the phase of the final state:

$$|\psi_{\text{ent}}\rangle = \frac{1}{\sqrt{2}}\left(\hat{a}^\dagger_{B1} + e^{i\phi_{23}}\hat{a}^\dagger_{B4}\right)|0\rangle,$$

where ϕ_{23} is zero if the two detectors that fired are equal, and π if they are different. This could be useful to extend the time extent and coherence time of a single photon.

It should be noted that $\hat{a}_1^\dagger$ and $\hat{a}_4^\dagger$ are non-overlapping temporal modes of the same input channel. However, with all processes being relatively slow compared to active polarisation switching elements, these two modes can be easily captured and sent to different spatial modes, with appropriate delays to have them available simultaneously if desired. Thus the entanglement of temporal modes could be mapped easily to spatial modes.

7.2 Conclusions

This thesis has shown the physical principles and experimental methods required for generating polarised and non-polarised single photons using atom-cavity systems. The device is tunable, controllable and well-understood, enabling an excellent degree of control over the interaction of single atoms and single photons that are emitted with it. This is evident from the results and ideas presented in Chapter 2, which showed how atoms embedded in cavities can be used to produce single-photon sources, and from Chapter 3, which listed all the devices and techniques used in the laboratory to control and characterise the photons produced by the source.

This degree of control is noticeable in the generation of long single photons with controllable amplitudes and phases, enabling the implementation of feedback protocols that allow for changes on a single-photon wavepacket's tail whilst its head is already measured. This has enabled us to examine and reevaluate the concept of what a single photon is: since the notion of a photon being a single excitation of an optical mode holds even if that mode is not well defined or subject to changes while it is already under observation, this gives an experimenter the power of influencing the temporal evolution of quantum systems. This has been evident from Chapter 4, where the implementation of the feedback protocol has not induced additional losses in the coherence of the emitted single photons. Although the feedback experiment has been performed using the non-polarised source, its results would be equally valid for a polarised source, and this one has been introduced to highlight future developments in the design of better, more standardised single-photon sources.

Due to a more thorough understanding of the role of the atomic structure of ^{87}Rb and its role in the efficiency limitations of single-photon generation, it would seem that the cavity designs that are to be implemented in the near future are reaching the limit of what an atom-cavity source can do with the D_2 line of ^{87}Rb. This was clear from Chapter 5, where simulations were performed to demonstrate the efficiency limitations of the D_2, opening the way for experimentally implementing polarised single-photon sources which are more robust to strong magnetic fields. While this is still several years away from fruition, the results achieved in this chapter could be used to improve the already existing sources, by potentially exploring other atomic transitions (such as those from the D_1 line of ^{87}Rb). At the same time, these results could be useful for other platforms which generate single photons using emitters embedded in cavities, such as ions [94], quantum dots [168] or defects in diamond [169]. Most of these results are soon to be implemented in our laboratory, with most of the experimental tools and devices already available.

Finally, in Chapter 6 we have also examined theoretically the models of atom-cavity coupling when considering the dielectric structure of the mirrors that confine the cavities, obtaining results that explicitly show a mismatch between the geometric length of the cavity and that one which can be estimated using the free spectral range of the cavity. This constitutes an important step both in theory and experiment, where atom-cavity coupled systems may need to take into account the design of their mirrors to accurately understand the coupling between a single emitter and the cavities it is embedded in.

All of these ideas and results show that there is still ample room for improvement, with a better understanding of single-atom single-photon interaction enabling us to implement more efficient, scalable and complex light-matter interfaces. The developments performed in this thesis could be useful for ensuring that future light-matter interfaces inside and outside the research group are able to operate at scale and improved, something which could be important in the event of future commercial exploitation.

References

[1] J. P. Dowling and G. J. Milburn, Philosophical Transactions of the Royal Society of London. Series A: Mathematical, Physical and Engineering Sciences **361**, 1655 (2003), ISSN 1364-503X, 1471-2962.

[2] R. P. Feynman, International Journal of Theoretical Physics **21**, 467 (1982), URL `https://doi.org/10.1007/bf02650179`.

[3] D. Deutsch, Proceedings of the Royal Society A: Mathematical, Physical and Engineering Sciences **400**, 97 (1985), ISSN 1364-5021, 1471-2946.

[4] D. Deutsch and R. Jozsa, Proceedings of the Royal Society of London. Series A: Mathematical and Physical Sciences **439**, 553 (1992), URL `https://doi.org/10.1098%2Frspa.1992.0167`.

[5] L. K. Grover, in *Proceedings of the twenty-eighth annual ACM symposium on Theory of computing - STOC '96* (ACM Press, 1996), URL `https://doi.org/10.1145/237814.237866`.

[6] P. Shor, in *Proceedings 35th Annual Symposium on Foundations of Computer Science* (1994), pp. 124–134.

[7] M. A. Nielsen and I. L. Chuang, *Quantum Computation and Quantum Information* (Cambridge University Press, Cambridge ; New York, 2010), 10th ed., ISBN 978-1-107-00217-3.

[8] P. G. Kwiat, J. R. Mitchell, P. D. D. Schwindt, and A. G. White, Journal of Modern Optics **47**, 257 (2000), `https://www.tandfonline.com/doi/pdf/10.1080/09500340008244040`, URL `https://www.tandfonline.com/doi/abs/10.1080/09500340008244040`.

[9] C.-Y. Lu, D. E. Browne, T. Yang, and J.-W. Pan, Phys. Rev. Lett. **99**, 250504 (2007), URL `https://link.aps.org/doi/10.1103/PhysRevLett.99.250504`.

[10] P. G. Kwiat, K. Mattle, H. Weinfurter, A. Zeilinger, A. V. Sergienko, and Y. Shih, Phys. Rev. Lett. **75**, 4337 (1995), URL `https://link.aps.org/doi/10.1103/PhysRevLett.75.4337`.

[11] E. Knill, R. Laflamme, and G. J. Milburn, Nature **409**, 46 (2001), ISSN 0028-0836, URL `https://doi.org/10.1038%2F35051009`.

[12] P. Kok, W. J. Munro, K. Nemoto, T. C. Ralph, J. P. Dowling, and G. J. Milburn, Reviews of Modern Physics **79**, 135 (2007).

[13] R. Raussendorf, D. E. Browne, and H. J. Briegel, Physical Review A **68**, 022312 (2003).

[14] D. E. Browne and T. Rudolph, Phys. Rev. Lett. **95**, 010501 (2005), URL `https://link.aps.org/doi/10.1103/PhysRevLett.95.010501`.

[15] F. Lenzini, B. Haylock, J. C. Loredo, R. A. Abrahão, N. A. Zakaria, S. Kasture, I. Sagnes, A. Lemaitre, H.-P. Phan, D. V. Dao, et al., Laser & Photonics Reviews **11**, 1600297 (2017).

[16] L. S. Madsen, F. Laudenbach, M. F. Askarani, F. Rortais, T. Vincent, J. F. F. Bulmer, F. M. Miatto, L. Neuhaus, L. G. Helt, M. J. Collins, et al., Nature **606**, 75 (2022), URL `https://doi.org/10.1038/s41586-022-04725-x`.

[17] F. Arute, K. Arya, R. Babbush, D. Bacon, J. C. Bardin, R. Barends, R. Biswas, S. Boixo, F. G. S. L. Brandao, D. A. Buell, et al., Nature **574**, 505 (2019), URL `https://doi.org/10.1038/s41586-019-1666-5`.

[18] H.-S. Zhong, H. Wang, Y.-H. Deng, M.-C. Chen, L.-C. Peng, Y.-H. Luo, J. Qin, D. Wu, X. Ding, Y. Hu, et al., Science **370**, 1460 (2020), `https://www.science.org/doi/pdf/10.1126/science.abe8770`, URL `https://www.science.org/doi/abs/10.1126/science.abe8770`.

[19] J. F. F. Bulmer, B. A. Bell, R. S. Chadwick, A. E. Jones, D. Moise, A. Rigazzi, J. Thorbecke, U.-U. Haus, T. V. Vaerenbergh, R. B. Patel, et al., Science Advances **8** (2022), URL `https://doi.org/10.1126/sciadv.abl9236`.

[20] H. J. Kimble, Nature **453**, 1023 (2008), ISSN 0028-0836, 1476-4687.

[21] R. Ursin, F. Tiefenbacher, T. Schmitt-Manderbach, H. Weier, T. Scheidl, M. Lindenthal, B. Blauensteiner, T. Jennewein, J. Perdigues, P. Trojek, et al., Nature Physics **3**, 481 (2007), URL `https://doi.org/10.1038/nphys629`.

[22] P. B. R. Nisbet-Jones, J. Dilley, A. Holleczek, O. Barter, and A. Kuhn, New Journal of Physics **15**, 053007 (2013), ISSN 1367-2630.

[23] J. C. Loredo, C. Antón, B. Reznychenko, P. Hilaire, A. Harouri, C. Millet, H. Ollivier, N. Somaschi, L. D. Santis, A. Lemaître, et al., Nature Photonics **13**, 803 (2019), URL `https://doi.org/10.1038/s41566-019-0506-3`.

[24] S. Ritter, C. Nölleke, C. Hahn, A. Reiserer, A. Neuzner, M. Uphoff, M. Mücke, E. Figueroa, J. Bochmann, and G. Rempe, Nature **484**, 195 (2012), URL `https://doi.org/10.1038/nature11023`.

[25] T. Wilk, S. C. Webster, A. Kuhn, and G. Rempe, Science **317**, 488 (2007), ISSN 0036-8075, 1095-9203.

[26] D. Moehring, P. Maunz, S. Olmschenk, K. Younge, D. Matsukevich, L.-M. Duan, and C. Monroe, Nature **449**, 68 (2007).

[27] T. D. Barrett, A. Rubenok, D. Stuart, O. Barter, A. Holleczek, J. Dilley, P. B. R. Nisbet-Jones, K. Poulios, G. D. Marshall, J. L. O'Brien, et al., Quantum Science and Technology **4**, 025008 (2019), ISSN 2058-9565.

[28] J. I. Cirac, P. Zoller, H. J. Kimble, and H. Mabuchi, Physical Review Letters **78**, 3221 (1997).

[29] T. E. Northup and R. Blatt, Nature Photonics **8**, 356 (2014), URL `https://doi.org/10.1038/nphoton.2014.53`.

[30] P. Lodahl, Quantum Science and Technology **3**, 013001 (2017), URL `https://doi.org/10.1088/2058-9565/aa91bb`.

[31] B. Hensen, H. Bernien, A. E. Dréau, A. Reiserer, N. Kalb, M. S. Blok, J. Ruitenberg, R. F. L. Vermeulen, R. N. Schouten, C. Abellán, et al., Nature **526**, 682 (2015), URL `https://doi.org/10.1038/nature15759`.

[32] J. I. Cirac and H. J. Kimble, Nature Photonics **11**, 18 (2017), ISSN 1749-4893.

[33] A. Kuhn, J. Smith, M. Keller, and D. M. Lucas, *Short roadmap to quantum networking*, https://www2.physics.ox.ac.uk/research/the-atom-photon-connection/roadmap-to-quantum-networking (2019).

[34] D. Hunger, T. Steinmetz, Y. Colombe, C. Deutsch, T. W. Hänsch, and J. Reichel, New Journal of Physics **12**, 065038 (2010), ISSN 1367-2630.

[35] T. H. Doherty, A. Kuhn, and E. Kassa, *Multi-resonant open-access micro-cavity arrays for light matter interaction* (2022), URL `https://arxiv.org/abs/2207.03676`.

[36] T. Doherty, Ph.D. thesis, University of Oxford (2021).

[37] T. D. Barrett, D. Stuart, O. Barter, and A. Kuhn, New Journal of Physics **20**, 073030 (2018), ISSN 1367-2630.

[38] R. Goldstein, Laser Focus **34** (1968).

[39] F. Pockels, *Lehrbuch Der Kristalloptik,* (Wentworth Press, 2018), ISBN 978-0-270-67734-8.

[40] S. Haroche and J.-M. Raimond, *Exploring the Quantum: Atoms, Cavities, and Photons* (Oxford University Press, 2006), ISBN 978-0-19-170862-6.

[41] E. Purcell, Physical Review **69**, 681, B10 (1946), ISSN 0031-899X.

[42] D. Kleppner, Phys. Rev. Lett. **47**, 233 (1981), URL `https://link.aps.org/doi/10.1103/PhysRevLett.47.233`.

[43] N. Ismail, C. C. Kores, D. Geskus, and M. Pollnau, Opt. Express **24**, 16366 (2016).

[44] M. Fox, *Quantum Optics: An Introduction*, no. 15 in Oxford Master Series in Physics (OUP Oxford, Oxford ; New York, 2006), ISBN 9780198566731, URL `https://books.google.co.uk/books?id=2%5FZP-LDF9jkC`.

[45] B. E. Saleh and M. C. Teich, *Fundamentals of Photonics*, vol. 22 (John Wiley & Sons, 1991).

[46] A. E. Siegman, *Lasers* (University Science Books, Mill Valley, Calif, 1986), ISBN 0935702113.

[47] M. A. Bandres and J. C. Gutiérrez-Vega, J. Opt. Soc. Am. A **21**, 873 (2004).

[48] W. T. Silfvast, *Laser Fundamentals* (Cambridge University Press, Cambridge ; New York, 2008), second edition ed., ISBN 978-0-521-54105-3.

[49] O. Svelto, *Principles of Lasers*, vol. 5 (Springer US, 2010).

[50] E. Jaynes and F. Cummings, Proceedings of the IEEE **51**, 89 (1963), ISSN 0018-9219.

[51] G. S. Vasilev, A. Kuhn, and N. V. Vitanov, Physical Review A **80**, 013417 (2009), ISSN 1050-2947, 1094-1622.

[52] P. Nisbet-Jones, Ph.D. thesis, University of Oxford, Clarendon Laboratory (2012).

[53] J. Dilley, P. Nisbet-Jones, B. W. Shore, and A. Kuhn, Physical Review A **85**, 023834 (2012).

[54] T. Wilk, S. C. Webster, H. P. Specht, G. Rempe, and A. Kuhn, Phys. Rev. Lett. **98**, 063601 (2007), URL `http://link.aps.org/doi/10.1103/PhysRevLett.98.063601`.

[55] A. Predojević and M. W. Mitchell, eds., *Engineering the Atom-Photon Interaction: Controlling Fundamental Processes with Photons, Atoms and Solids*, Nano-Optics and Nanophotonics (Springer International Publishing, 2015), ISBN 978-3-319-19230-7.

[56] A. Kuhn and D. Ljunggren, Contemporary Physics **51**, 289 (2010), ISSN 0010-7514, `http://dx.doi.org/10.1080/00107511003602990`, URL `http://dx.doi.org/10.1080/00107511003602990`.

[57] G. S. Agarwal, J. Opt. Soc. Am. B **2**, 480 (1985), URL `https://opg.optica.org/josab/abstract.cfm?URI=josab-2-3-480`.

[58] R. J. Thompson, G. Rempe, and H. J. Kimble, Phys. Rev. Lett. **68**, 1132 (1992), URL `https://link.aps.org/doi/10.1103/PhysRevLett.68.1132`.

[59] A. Kuhn, M. Hennrich, and G. Rempe, Phys. Rev. Lett. **89**, 067901 (2002), URL `https://link.aps.org/doi/10.1103/PhysRevLett.89.067901`.

[60] P. B. R. Nisbet-Jones, J. Dilley, D. Ljunggren, and A. Kuhn, New Journal of Physics **13**, 103036 (2011), ISSN 1367-2630, URL `https://doi.org/10.1088%2F1367-2630%2F13%2F10%2F103036`.

[61] A. Holleczek, O. Barter, A. Rubenok, J. Dilley, P. B. R. Nisbet-Jones, G. Langfahl-Klabes, G. D. Marshall, C. Sparrow, J. L. O'Brien, K. Poulios, et al., Phys. Rev. Lett. **117**, 023602 (2016), URL `https://link.aps.org/doi/10.1103/PhysRevLett.117.023602`.

[62] M. Hennrich, T. Legero, A. Kuhn, and G. Rempe, Physical Review Letters **85**, 4872 (2000), ISSN 0031-9007, 1079-7114.

[63] T. Barrett, Ph.D. thesis, University of Oxford (2018).

[64] O. Barter, Ph.D. thesis, University of Oxford (2016).

[65] G. S. Vasilev, D. Ljunggren, and A. Kuhn, New J. Phys. **12**, 063024 (2010), ISSN 1367-2630.

[66] T. D. Barrett, O. Barter, D. Stuart, B. Yuen, and A. Kuhn, Physical Review Letters **122** (2019), ISSN 0031-9007, 1079-7114.

[67] T. Wilk, H. P. Specht, S. C. Webster, G. Rempe, and A. Kuhn, Journal of Modern Optics **54**, 1569 (2007), URL `https://doi.org/10.1080/09500340600736777`.

[68] R. Schmied, arXiv:1403.7050 [physics, physics:quant-ph] (2014), `1403.7050`.

[69] D. A. Steck (2001).

[70] P. Tremblay, A. Michaud, M. Levesque, S. Thériault, M. Breton, J. Beaubien, and N. Cyr, Phys. Rev. A **42**, 2766 (1990).

[71] A. Sargsyan, E. Klinger, G. Hakhumyan, A. Tonoyan, A. Papoyan, C. Leroy, and D. Sarkisyan, JOSA B **34**, 776 (2017), ISSN 1520-8540.

[72] N. V. Vitanov, A. A. Rangelov, B. W. Shore, and K. Bergmann, Rev. Mod. Phys. **89**, 015006 (2017), URL `https://link.aps.org/doi/10.1103/RevModPhys.89.015006`.

[73] U. Gaubatz, P. Rudecki, S. Schiemann, and K. Bergmann, The Journal of Chemical Physics **92**, 5363 (1990), `http://dx.doi.org/10.1063/1.458514`.

[74] U. Gaubatz, P. Rudecki, M. Becker, S. Schiemann, M. Külz, and K. Bergmann, Chemical Physics Letters **149**, 463 (1988), ISSN 0009-2614.

[75] K. Bergmann, H.-C. Nägerl, C. Panda, G. Gabrielse, E. Miloglyadov, M. Quack, G. Seyfang, G. Wichmann, S. Ospelkaus, A. Kuhn, et al., Journal of Physics B: Atomic, Molecular and Optical Physics **52**, 202001 (2019), URL `https://doi.org/10.1088/1361-6455/ab3995`.

[76] T. Legero, T. Wilk, M. Hennrich, G. Rempe, and A. Kuhn, Phys. Rev. Lett. **93**, 070503 (2004).

[77] T. Legero, T. Wilk, A. Kuhn, and G. Rempe, Advances In Atomic, Molecular, and Optical Physics **53**, 253 (2006).

[78] J. McKeever, A. Boca, A. D. Boozer, R. Miller, J. R. Buck, A. Kuzmich, and H. J. Kimble, Science **303**, 1992 (2004), ISSN 0036-8075, 1095-9203.

[79] J.-R. Álvarez, M. IJspeert, O. Barter, B. Yuen, T. D. Barrett, D. Stuart, J. Dilley, A. Holleczek, and A. Kuhn, Journal of Physics B: Atomic, Molecular and Optical Physics **55**, 054001 (2022), URL `https://doi.org/10.1088/1361-6455/ac5674`.

[80] T. Wilk, Ph.D. thesis, Max-Planck-Institute of Quantum Optics (2008).

[81] J. Hofmann, M. Krug, N. Ortegel, L. Gérard, M. Weber, W. Rosenfeld, and H. Weinfurter, Science **337**, 72 (2012), URL `https://doi.org/10.1126%2Fscience.1221856`.

[82] L. Stephenson, D. Nadlinger, B. Nichol, S. An, P. Drmota, T. Ballance, K. Thirumalai, J. Goodwin, D. Lucas, and C. Ballance, Physical Review Letters **124** (2020), URL `https://doi.org/10.1103%2Fphysrevlett.124.110501`.

[83] H. Bernien, B. Hensen, W. Pfaff, G. Koolstra, M. S. Blok, L. Robledo, T. H. Taminiau, M. Markham, D. J. Twitchen, L. Childress, et al., Nature **497**, 86 (2013), URL `https://doi.org/10.1038%2Fnature12016`.

[84] R. Stockill, M. Stanley, L. Huthmacher, E. Clarke, M. Hugues, A. Miller, C. Matthiesen, C. L. Gall, and M. Atatüre, Physical Review Letters **119** (2017), URL `https://doi.org/10.1103%2Fphysrevlett.119.010503`.

[85] M. Pompili, S. L. N. Hermans, S. Baier, H. K. C. Beukers, P. C. Humphreys, R. N. Schouten, R. F. L. Vermeulen, M. J. Tiggelman, L. dos Santos Martins, B. Dirkse, et al., Science **372**, 259 (2021), URL `https://doi.org/10.1126%2Fscience.abg1919`.

[86] M. Keller, B. Lange, K. Hayasaka, W. Lange, and H. Walther, Journal of Physics B: Atomic, Molecular and Optical Physics **36**, 613 (2003).

[87] H. Takahashi, E. Kassa, C. Christoforou, and M. Keller, Phys. Rev. A **96**, 023824 (2017).

[88] M. Keller, B. Lange, K. Hayasaka, W. Lange, and H. Walther, Nature **431**, 1075 (2004), ISSN 0028-0836, 1476-4687.

[89] A. B. Mundt, A. Kreuter, C. Becher, D. Leibfried, J. Eschner, F. Schmidt-Kaler, and R. Blatt, Phys. Rev. Lett. **89**, 103001 (2002).

[90] H. G. Barros, A. Stute, T. E. Northup, C. Russo, P. O. Schmidt, and R. Blatt, New Journal of Physics **11**, 103004 (2009).

[91] A. Stute, B. Casabone, B. Brandstätter, D. Habicher, H. G. Barros, P. O. Schmidt, T. E. Northup, and R. Blatt, Applied Physics B **107**, 1145 (2012), ISSN 1432-0649.

[92] M. Teller, D. A. Fioretto, P. C. Holz, P. Schindler, V. Messerer, K. Schüppert, Y. Zou, R. Blatt, J. Chiaverini, J. Sage, et al., Physical Review Letters **126** (2021), URL `https://doi.org/10.1103/physrevlett.126.230505`.

[93] V. Krutyanskiy, M. Galli, V. Krcmarsky, S. Baier, D. A. Fioretto, Y. Pu, A. Mazloom, P. Sekatski, M. Canteri, M. Teller, et al., *Entanglement of trapped-ion qubits separated by 230 meters* (2022), URL `https://arxiv.org/abs/2208.14907`.

[94] H. Takahashi, E. Kassa, C. Christoforou, and M. Keller, Phys. Rev. Lett. **124**, 013602 (2020), URL `https://link.aps.org/doi/10.1103/PhysRevLett.124.013602`.

[95] T. Macha, E. Uruñuela, W. Alt, M. Ammenwerth, D. Pandey, H. Pfeifer, and D. Meschede, Physical Review A **101** (2020), URL `https://doi.org/10.1103/physreva.101.053406`.

[96] A. Kuhn, M. Hennrich, T. Bondo, and G. Rempe, Appl Phys B **69**, 373 (1999), ISSN 1432-0649.

[97] C. J. Hood, Ph.D. thesis, California Institute of Technology (2000), URL `https://resolver.caltech.edu/CaltechETD:etd-09222005-105541`.

[98] T. E. Northup, Ph.D. thesis, California Institute of Technology (2008), URL `https://resolver.caltech.edu/CaltechETD:etd-05242008-114227`.

[99] J. Dilley, Ph.D. thesis, University of Oxford, Clarendon Laboratory (2012).

[100] A. Holleczek, Ph.D. thesis, University of Oxford (2015).

[101] T. Barrett, Ph.D. thesis, University of Oxford (2018).

[102] T. Puppe, I. Schuster, A. Grothe, A. Kubanek, K. Murr, P. W. H. Pinkse, and G. Rempe, Physical Review Letters **99** (2007), URL `https://doi.org/10.1103/physrevlett.99.013002`.

[103] N. Podoliak, H. Takahashi, M. Keller, and P. Horak, Physical Review Applied **6** (2016), URL `https://doi.org/10.1103/physrevapplied.6.044008`.

[104] D. Stuart, Ph.D. thesis, University of Oxford (2014).

[105] N. Holland, D. Stuart, O. Barter, and A. Kuhn, Journal of Modern Optics **65**, 2133 (2018), URL `https://doi.org/10.1080/09500340.2018.1499978`.

[106] N. Holland, Ph.D. thesis, University of Oxford (2020).

[107] L. Förster, W. Alt, I. Dotsenko, M. Khudaverdyan, D. Meschede, Y. Miroshnychenko, S. Reick, and A. Rauschenbeutel, New Journal of Physics **8**, 259 (2006), ISSN 1367-2630.

[108] J. Gallego, W. Alt, T. Macha, M. Martinez-Dorantes, D. Pandey, and D. Meschede, Physical Review Letters **121**, 173603 (2018), ISSN 0031-9007, 1079-7114.

[109] P. Thomas, L. Ruscio, O. Morin, and G. Rempe, Nature **608**, 677 (2022), URL `https://doi.org/10.1038/s41586-022-04987-5`.

[110] C. J. Foot, *Atomic Physics*, no. 7. Atomic, Optical, and laser physics in Oxford Master Series in Physics (Oxford University Press, Oxford ; New York, 2005), ISBN 978-0-19-850695-9 978-0-19-850696-6.

[111] S. Chu, L. Hollberg, J. E. Bjorkholm, A. Cable, and A. Ashkin, Phys. Rev. Lett. **55**, 48 (1985).

[112] R. Hanbury Brown and R. Q. Twiss, Nature **178**, 1046 EP (1956).

[113] H. J. Kimble, M. Dagenais, and L. Mandel, Physical Review Letters **39**, 691 (1977).

[114] C. K. Hong and L. Mandel, Phys. Rev. Lett. **56**, 58 (1986).

[115] P. Grangier, G. Roger, and A. Aspect, EPL (Europhysics Letters) **1**, 173 (1986).

[116] M. O. Scully and M. S. Zubairy, *Quantum Optics* (Cambridge University Press, 1997), URL `https://doi.org/10.1017/cbo9780511813993`.

[117] E. Schrödinger, Naturwissenschaften **23**, 807 (1935), ISSN 1432-1904.

[118] K. Landsman, in *Foundations of Quantum Theory: From Classical Concepts to Operator Algebras*, edited by K. Landsman (Springer International Publishing, Cham, 2017), Fundamental Theories of Physics, pp. 435–457, ISBN 978-3-319-51777-3.

[119] J. Zhang, Y.-x. Liu, R.-B. Wu, K. Jacobs, and F. Nori, Physics Reports **679**, 1 (2017), ISSN 0370-1573.

[120] S. Habib, K. Jacobs, and H. Mabuchi, p. 10 (2002).

[121] Y. Yamamoto, N. Imoto, and S. Machida, Physical Review A **33**, 3243 (1986), ISSN 0556-2791.

[122] M. A. Armen, J. K. Au, J. K. Stockton, A. C. Doherty, and H. Mabuchi, Physical Review Letters **89** (2002).

[123] W. P. Smith, J. E. Reiner, L. A. Orozco, S. Kuhr, and H. M. Wiseman, Physical Review Letters **89** (2002).

[124] C. Sayrin, I. Dotsenko, X. Zhou, B. Peaudecerf, T. Rybarczyk, S. Gleyzes, P. Rouchon, M. Mirrahimi, H. Amini, M. Brune, et al., Nature **477**, 73 (2011).

[125] C. K. Hong, Z. Y. Ou, and L. Mandel, Physical Review Letters **59**, 2044 (1987), URL `https://doi.org/10.1103%2Fphysrevlett.59.2044`.

[126] P. Schneeweiss, S. Zeiger, T. Hoinkes, A. Rauschenbeutel, and J. Volz, Opt. Lett. **42**, 85 (2017), URL `https://opg.optica.org/ol/abstract.cfm?URI=ol-42-1-85`.

[127] T. Legero, T. Wilk, A. Kuhn, and G. Rempe, Applied Physics B: Lasers and Optics **77**, 797 (2003), `quant-ph/0308024`.

[128] S. Deléglise, I. Dotsenko, C. Sayrin, J. Bernu, M. Brune, J.-M. Raimond, and S. Haroche, Nature **455**, 510 (2008), URL `https://doi.org/10.1038/nature07288`.

[129] B. Hacker, S. Welte, S. Daiss, A. Shaukat, S. Ritter, L. Li, and G. Rempe, Nature Photonics **13**, 110 (2019), ISSN 1749-4885, 1749-4893.

[130] A. Peruzzo, M. Lobino, J. C. F. Matthews, N. Matsuda, A. Politi, K. Poulios, X.-Q. Zhou, Y. Lahini, N. Ismail, K. Worhoff, et al., Science **329**, 1500 (2010).

[131] H.-P. Breuer and F. Petruccione, *The Theory of Open Quantum Systems* (Oxford University PressOxford, 2007), URL `https://doi.org/10.1093/acprof:oso/9780199213900.001.0001`.

[132] M. Auzinsh, D. Budker, and S. Rochester, *Optically Polarized Atoms: Understanding Light-Atom Interactions* (Oxford University Press, Oxford, New York, 2010), ISBN 978-0-19-956512-2.

[133] J. R. Johansson, P. D. Nation, and F. Nori, Computer Physics Communications **184**, 1234 (2013), ISSN 0010-4655.

[134] T. Barrett, *rb-cqed: Modelling simple atoms and 87rb in cavity-qed*, `https://github.com/tomdbar/rb-cqed` (2018).

[135] L. Giannelli, P. Sgroi, J. Brown, G. S. Paraoanu, M. Paternostro, E. Paladino, and G. Falci, Physics Letters A **434**, 128054 (2022), URL `https://doi.org/10.1016/j.physleta.2022.128054`.

[136] X. Laforgue, G. Dridi, and S. Guérin, Phys. Rev. A **105**, 032807 (2022), URL `https://link.aps.org/doi/10.1103/PhysRevA.105.032807`.

[137] *Integrated Optical Amplitude Modulator*, URL `https://www.jenoptik.com/products/optoelectronic-systems/light-modulation/integrated-optical-modulators-fiber-coupled/amplitude-modulator#:~:text=The%20Jenoptik%20integrated%20optical%20amplitude,up%20to%20the%20gigahertz%20range`.

[138] J. D. Ellis, *Field Guide to Displacement Measuring Interferometry* (SPIE, 2014), URL `https://doi.org/10.1117/3.1002328`.

[139] A. Saharyan, J.-R. Álvarez, T. H. Doherty, A. Kuhn, and S. Guérin, Applied Physics Letters **118**, 154002 (2021), URL `https://doi.org/10.1063/5.0047145`.

[140] H. A. Macleod, *Thin-Film Optical Filters* (Institute of Physics Publishing, 2018), ISBN 978-1-315-27049-4 978-1-351-98222-1.

[141] C. J. Hood, H. J. Kimble, and J. Ye, Phys. Rev. A **64**, 033804 (2001).

[142] A. M. Kern, D. Zhang, M. Brecht, A. I. Chizhik, A. V. Failla, F. Wackenhut, and A. J. Meixner, Chem. Soc. Rev. **43**, 1263 (2014), ISSN 1460-4744.

[143] P. Zhong, W. Rong-han, and W. Qi-ming, Acta Physica Sinica (Overseas Edition) **4**, 810 (1995), ISSN 1004-423X.

[144] J. H. Apfel, Applied Optics **16**, 1880 (1977), ISSN 0003-6935, 1539-4522.

[145] K. J. Vahala, Nature **424**, 839 (2003), ISSN 1476-4687.

[146] S. M. Dutra and P. L. Knight, Phys. Rev. A **53**, 3587 (1996).

[147] W. Vogel and D.-G. Welsch, *Quantum Optics* (Wiley, 2006), 1st ed., ISBN 978-3-527-40507-7 978-3-527-60852-2.

[148] K. Ujihara, A. Nakamura, O. Manba, and X.-P. Feng, Jpn. J. Appl. Phys. **30**, 3388 (1991), ISSN 1347-4065.

[149] X.-P. Feng, Optics Communications **83**, 162 (1991), ISSN 0030-4018.

[150] S. M. Dutra, *Cavity Quantum Electrodynamics: The Strange Theory of Light in a Box*, Wiley Series in Lasers and Applications (Wiley, Hoboken, NJ, 2005), ISBN 978-0-471-44338-4.

[151] D. Walls and G. J. Milburn, *Input–Output Formulation of Optical Cavities* (Springer Berlin Heidelberg, Berlin, Heidelberg, 2008), pp. 127–141, ISBN 978-3-540-28574-8, URL `https://doi.org/10.1007/978-3-540-28574-8_7`.

[152] B. Rousseaux, Ph.D. thesis, Laboratoire Interdisciplinaire Carnot de Bourgogne (2016).

[153] M. Banning, J. Opt. Soc. Am. **37**, 792 (1947).

[154] Y. Suematsu, S. Arai, and K. Kishino, Journal of Lightwave Technology **1**, 161 (1983), ISSN 1558-2213.

[155] L. A. Coldren, S. W. Corzine, and M. L. Mashanovitch, *Diode Lasers and Photonic Integrated Circuits* (Wiley-Blackwell, Hoboken, N.J, 2012), 2nd ed., ISBN 978-0-470-48412-8.

[156] C. Wuttke, Ph.D. thesis, Mainz, Univ., Diss. (2014).

[157] A. A. P. Trichet, P. R. Dolan, D. James, G. M. Hughes, C. Vallance, and J. M. Smith, Nano Lett. **16**, 6172 (2016), ISSN 1530-6984.

[158] M. Mader, J. Reichel, T. W. Hänsch, and D. Hunger, Nature Communications **6**, 7249 (2015), ISSN 2041-1723.

[159] G. L. Giorgi, A. Saharyan, S. Guérin, D. Sugny, and B. Bellomo, Phys. Rev. A **101**, 012122 (2020).

[160] D. E. Chang, A. S. Sørensen, E. A. Demler, and M. D. Lukin, Nature Physics **3**, 807 (2007), ISSN 1745-2473.

[161] B. Huttner and S. M. Barnett, Physical Review A **46**, 4306 (1992), ISSN 1050-2947.

[162] V. Dorier, J. Lampart, S. Guérin, and H. R. Jauslin, Physical Review A **100** (2019), ISSN 2469-9926.

[163] V. Dorier, S. Guérin, and H.-R. Jauslin, Nanophotonics **9**, 3899 (2020), ISSN 2192-8614.

[164] M. Brekenfeld, D. Niemietz, J. D. Christesen, and G. Rempe, Nature Physics **16**, 647 (2020).

[165] V. Loo, L. Lanco, A. Lemaître, I. Sagnes, O. Krebs, P. Voisin, and P. Senellart, Applied Physics Letters **97**, 241110 (2010).

[166] S. Johnson, P. R. Dolan, T. Grange, A. A. P. Trichet, G. Hornecker, Y. C. Chen, L. Weng, G. M. Hughes, A. A. R. Watt, A. Auffèves, et al., New J. Phys. **17**, 122003 (2015), ISSN 1367-2630.

[167] S. Garcia, F. Ferri, J. Reichel, and R. Long, Optics Express **28**, 15515 (2020).

[168] C. Antón, J. C. Loredo, G. Coppola, H. Ollivier, N. Viggianiello, A. Harouri, N. Somaschi, A. Crespi, I. Sagnes, A. Lemaître, et al., Optica **6**, 1471 (2019), URL `https://doi.org/10.1364%2Foptica.6.001471`.

[169] E. N. Knall, C. M. Knaut, R. Bekenstein, D. R. Assumpcao, P. L. Stroganov, W. Gong, Y. Q. Huan, P.-J. Stas, B. Machielse, M. Chalupnik, et al., Phys. Rev. Lett. **129**, 053603 (2022), URL `https://link.aps.org/doi/10.1103/PhysRevLett.129.053603`.

A

Appendix for Chapter 6

A.1 Reference table for wavelengths

For the purposes of future reference, we list here the parameters used to characterise our system:

Definition	Notation
Mirror stack design wavelength and angular frequency.	$\lambda_0, \omega_0 = \frac{2\pi c}{\lambda_0}$
Propagating light wavelength and angular frequency (continuous).	$\lambda, \omega = \frac{2\pi c}{\lambda}$
Geometric cavity length	ℓ_c
Cavity resonance wavelength and angular frequency.	$\lambda_m, \omega_m = \frac{2\pi c}{\lambda_m} = \frac{\pi c m}{\ell_c}$
Actual cavity resonance angular frequency, leading to a resonance effective length.	$\omega_{\text{eff}} = \omega_N^{(m)}$, $\ell_{\text{eff}} = \frac{\pi c m}{\omega_{\text{eff}}}$
Coupling factor cavity length.	$L_N^{(m)}$

?tablename? A.1: Relevant notations for the different wavelengths and frequencies within the atom-cavity system. The index m corresponds to the number of anti-nodes of the wave between the mirrors, and N to the $2N-1$ dielectric layers.

A.2 Derivation of $|T(\omega)|^2$ as a sum of Lorentzian functions

As shown by Eq. 6.16, $T(\omega)$ has the form

$$T(\omega) = \frac{t(\omega)}{1 + r(\omega) e^{2i\frac{\omega}{c}(\ell_c + \frac{\delta}{2})}}. \tag{A.1}$$

By writing the square modulus of $T(\omega)$ from Eq. 6.16, and using the conditions of Eqs. 6.19 and 6.20, we get

$$|T(\omega)|^2 = \frac{1 - |r|^2}{|1 + |r|e^{i\Phi}|^2} = \left[1 - \frac{|r|e^{i\Phi}}{1 + |r|e^{i\Phi}} - \frac{|r|e^{-i\Phi}}{1 + |r|e^{-i\Phi}}\right], \tag{A.2}$$

where for simplicity we have not written the dependence of $r(\omega)$ on ω, and we have used the following notations $r(\omega) = |r|e^{i\Phi_r(\omega)}$, and $\Phi = 2\frac{\omega}{c}L_1 + \Phi_r(\omega)$. Using the geometric series formula

$$\sum_{n=1}^{+\infty} q^n = \frac{q}{1-q}, \quad |q| < 1 \tag{A.3}$$

we can write the above expression for the response function as follows

$$|T(\omega)|^2 = 1 + \sum_{n=1}^{+\infty} |r|^n \left(e^{in(\Phi+\pi)} + e^{-in(\Phi+\pi)} \right)$$
$$= \sum_{n=-\infty}^{+\infty} |r|^{|n|} e^{in(\Phi+\pi)}. \qquad \text{(A.4)}$$

We further apply the Poisson summation formula, which states that

$$\sum_{n=-\infty}^{+\infty} f(n) = \sum_{m=-\infty}^{+\infty} \int_{-\infty}^{+\infty} dx\ f(x) e^{-i2\pi mx} = \sum_{m=-\infty}^{+\infty} \tilde{f}(m) \qquad \text{(A.5)}$$

where $\tilde{f}(m) = \mathrm{F}_m \left[f(x) \right]$ is the Fourier transform of $f(x)$. We apply the Fourier transform to the function

$$f(x) = |r|^{|x|} e^{ix(\Phi+\pi)} = e^{|x| \ln |r| + ix(\Phi+\pi)}$$

and obtain

$$\mathrm{F}_m \left[f(x) \right] = \frac{2a}{a^2 + \alpha^2}, \qquad \text{(A.6)}$$

where $a = -\ln|r|$, $\alpha = \Phi + \pi - 2\pi m$. Hence,

$$\tilde{f}(m) = \frac{-2 \ln |r|}{(\ln |r|)^2 + ((\Phi + \pi) - 2\pi m)^2}. \qquad \text{(A.7)}$$

We further expand this expression by writing the explicit expression for Φ:

$$\tilde{f}(m) = \frac{-2 \ln |r|}{(\ln |r|)^2 + ((2\frac{\omega}{c} L_1 + \Phi_r + \pi) - 2\pi m)^2}, \qquad \text{(A.8)}$$

and multiplying both the numerator and the denominator by $(c/2L_1)^2$ we find the Lorentzian structure of the cavity spectral response function, still having the parameters $\tilde{\omega}_m$ and γ_1 depend on ω:

$$|T(\omega)|^2 = \sum_{n=-\infty}^{+\infty} \frac{c}{2L_1} \frac{\gamma_1(\omega)}{(\omega - \tilde{\omega}_m(\omega))^2 + \left(\frac{\gamma_1(\omega)}{2}\right)^2}, \tag{A.9}$$

$$\gamma_1(\omega) = -\frac{c}{L_1} \ln |r(\omega)|, \tag{A.10}$$

$$\tilde{\omega}_m = \frac{\pi c}{L_1} m - \frac{c}{2L_1} (\Phi_r(\omega) + \pi), \tag{A.11}$$

A.3 Derivation of the effective Hamiltonian

In order to extract the description of the atom-cavity open system, we first solve the Schrödinger equation

$$i\hbar \frac{\partial}{\partial t} |\psi(t)\rangle = \hat{H} |\psi(t)\rangle . \tag{A.12}$$

If we put the Hamiltonian of Eq. 6.10 and the following wavefunction

$$|\psi(t)\rangle = \int_0^{+\infty} d\omega \left(e^{-i\omega t} c_{g,1}(\omega, t) |g, 1_\omega\rangle + e^{-i\omega_A t} c_{e,0}(t) |e, 0\rangle \right) \tag{A.13}$$

into Eq. (A.12), where $|1_\omega\rangle$ corresponds to the single excitation of a mode Φ_ω, i.e. $|1_\omega\rangle = \hat{a}_\omega^\dagger |0\rangle$, we obtain the dynamical equations for the coefficients $c_{g,1}(\omega, t)$, $c_{e,0}(t)$ [152]:

$$\dot{c}_{g,1}(\omega, t) = -\sum_m \eta^*_{\omega,m} e^{i(\omega - \omega_A)t} c_{e,0}(t), \tag{A.14}$$

$$\dot{c}_{e,0}(t) = \int_0^{+\infty} d\omega \sum_m \eta_{\omega,m} e^{-i(\omega - \omega_A)t} c_{g,1}(\omega, t). \tag{A.15}$$

In order to trace out the continuous degrees of freedom from the dynamics, we define the integrated, mode-selective probability amplitude:

$$c_{g,1}^{(m)}(t) = \frac{1}{g_m} \int_0^{+\infty} d\omega \, \eta_{\omega,m} e^{-i(\omega - \omega_A)t} c_{g,1}(\omega, t). \tag{A.16}$$

We now write the time derivative of this quantity, using the property

$$\eta^*_{\omega,m}\eta_{\omega,m'} = \delta_{mm'}|\eta_{\omega,m}|^2, \tag{A.17}$$

which is a consequence of the fact that the response function is a sum of narrow peaked and well separated Lorentzians. Using this property we get the equation of motion for the m-th mode, using the integration of Eq. (37) and inverting the order of time and frequency integration:

$$\begin{aligned}\dot{c}^{(m)}_{g,1}(t) = \dot{c}^{(m,0)}_{g,1}(t) - \frac{1}{g_m}\int_0^{+\infty} d\omega\, |\eta_{\omega,m}|^2 c_{e,0}(t) \\ + \frac{i}{g_m}\int_0^{t} dt' c_{e,0}(t') \int_0^{+\infty} d\omega\, |\eta_{\omega,m}|^2 (\omega-\omega_A) e^{-i(\omega-\omega_A)(t-t')}\end{aligned} \tag{A.18}$$

where we introduce the time derivative of the initial time defined as follows:

$$c^{(m,0)}_{g,1} = \frac{1}{g_m}\int_0^{+\infty} d\omega\, \eta_{\omega,m} e^{-i(\omega-\omega_A)t} c_{g,1}(\omega,0). \tag{A.19}$$

Two integrals appear in (A.18):

$$\mathcal{I}_1 = \int_0^{+\infty} d\omega\, |\eta_{\omega,m}|^2, \tag{A.20}$$

$$\mathcal{I}_2 = \int_0^{+\infty} d\omega\, |\eta_{\omega,m}|^2 (\omega-\omega_A) e^{-i(\omega-\omega_A)(t-t')}, \tag{A.21}$$

which can be evaluated using complex contour methods, and in the limit of $\epsilon = \gamma^{(m)}_N \frac{x_A+\ell}{c} \ll 1$, we obtain (here after in the parameters $\gamma^{(m)}_N$, $L^{(m)}_N$ and $\omega^{(m)}_N$ we omit the index indicating the number of layers)

$$\mathcal{I}_1 = \frac{\omega^{(m)}|d|^2}{\hbar\epsilon_0\mathcal{A}L^{(m)}} \sin^2\left[2\frac{\omega^{(m)}}{c}(x_A+\ell_c)\right], \tag{A.22}$$

$$\mathcal{I}_2 = \frac{\omega^{(m)}|d|^2}{\hbar\epsilon_0\mathcal{A}L^{(m)}} \sin^2\left[2\frac{\omega^{(m)}}{c}(x_A+\ell_c)\right] \left(\Delta_m - i\frac{\gamma^{(m)}}{2}\right) e^{-i(\Delta_m - i\frac{\gamma^{(m)}}{2})(t-t')}, \tag{A.23}$$

where $\Delta_m = \omega^{(m)} - \omega_A$. We note that, since we defined g_m as the normalization coefficient of (A.16), then the integrals $\mathcal{I}_1$ and $\mathcal{I}_2$ become

$$\mathcal{I}_1 = |g_m|^2, \tag{A.24}$$

$$\mathcal{I}_2 = |g_m|^2 \left(\Delta_m - i\frac{\gamma^{(m)}}{2}\right) e^{-i(\Delta_m - i\frac{\gamma^{(m)}}{2})(t-t')}, \tag{A.25}$$

with

$$g_m = i\sqrt{\frac{\omega^{(m)}}{\hbar\epsilon_0\mathcal{A}L^{(m)}}}\, d e^{i\frac{\omega^{(m)}}{c}\ell_c} \sin\left[\frac{\omega^{(m)}}{c}(x_A + \ell_c)\right] + \mathcal{O}\left(\epsilon^2\right). \tag{A.26}$$

Having obtained the expression for g_m, we can now rewrite the dynamical equation (A.18) as follows:

$$\begin{aligned} \dot{c}^{(m)}_{g,1} = \dot{c}^{(m,0)}_{g,1} &- g^*_m c_{e,0}(t) \\ &+ i g^*_m \int_0^t dt' c_{e,0}(t') \left(\Delta_m - i\frac{\gamma^{(m)}}{2}\right) e^{-i(\Delta_m - i\frac{\gamma^{(m)}}{2})(t-t')} \end{aligned} \tag{A.27}$$

If we formally integrate equation (A.14) and put the result in (A.16), it can be shown that

$$c^{(m)}_{g,1}(t) - c^{(m,0)}_{g,1} = -g^*_m \int_0^t dt' c_{e,0}(t') e^{-i(\Delta_m - i\frac{\gamma^{(m)}}{2})(t-t')}, \tag{A.28}$$

hence Eq. (A.27) becomes

$$\dot{c}^{(m)}_{g,1} = \dot{c}^{(m,0)}_{g,1}(t) - g^*_m c_{e,0}(t) - i\left(\Delta_m - i\frac{\gamma^{(m)}}{2}\right)(c^{(m)}_{g,1}(t) - c^{(m,0)}_{g,1}(t)). \tag{A.29}$$

Considering that at initial time $t = 0$ the atom is in its excited state and there is no photon in the cavity, we finally get the following set of dynamical equations

$$\begin{aligned} \dot{c}^{(m)}_{g,1} &= -g^*_m c_{e,0}(t) - i\left(\Delta_m - i\frac{\gamma^{(m)}}{2}\right) c^{(m)}_{g,1}, \\ \dot{c}_{e,0} &= \sum_m g_m c^{(m)}_{g,1}(t), \end{aligned} \tag{A.30}$$

which then yields that for the state described by the wavefunction

$$|\psi(t)\rangle = \sum_m c_{g,1}^{(m)} |g, 1_m\rangle + c_{e,0}(t) |e, 0\rangle \tag{A.31}$$

the Hamiltonian can be written as

$$\hat{H}_{\text{eff}} = \hbar \sum_m \left(\Delta_m - i\frac{\gamma^{(m)}}{2}\right) |a\rangle\langle a|_m^{\dagger} |a\rangle\langle a|_m + ig_m |\sigma\rangle\langle\sigma|_+ |a\rangle\langle a|_m - ig_m^* |\sigma\rangle\langle\sigma|_- |a\rangle\langle a|_m^{\dagger}, \tag{A.32}$$

where $\hat{a}_m$ is defined in (6.49). Finally, we can write the effective Hamiltonian back from the rotating frame, via the transformation:

$$R = \exp\left(i\omega_A t(|\sigma\rangle\langle\sigma|_+ |\sigma\rangle\langle\sigma|_- + \sum |a\rangle\langle a|_m^{\dagger} |a\rangle\langle a|_m)\right), \tag{A.33}$$

leading to an effective Hamiltonian describing the dynamics restricted between the mirrors:

$$\begin{aligned}\hat{H}_{\text{eff}} = \hbar\omega_A |\sigma\rangle\langle\sigma|_+ |\sigma\rangle\langle\sigma|_- + \hbar \sum_m \left(\omega^{(m)} - i\frac{\gamma^{(m)}}{2}\right) |a\rangle\langle a|_m^{\dagger} |a\rangle\langle a|_m \\ + ig_m |\sigma\rangle\langle\sigma|_+ |a\rangle\langle a|_m - ig_m^* |\sigma\rangle\langle\sigma|_- |a\rangle\langle a|_m^{\dagger}.\end{aligned} \tag{A.34}$$

It can be shown that in the case where we have off-resonant atom-cavity coupling, the effective Hamiltonian can be written as follows

$$\begin{aligned}\hat{H}_{\text{eff}} = \hbar\omega_A |\sigma\rangle\langle\sigma|_+ |\sigma\rangle\langle\sigma|_- + \hbar \sum_m \left(\omega^{(m)} - i\frac{\gamma^{(m)}}{2}\right) |a\rangle\langle a|_m^{\dagger} |a\rangle\langle a|_m + ig_m |\sigma\rangle\langle\sigma|_+ |a\rangle\langle a|_m \\ - ig_m^* |\sigma\rangle\langle\sigma|_- |a\rangle\langle a|_m^{\dagger} + i\underline{g}_{m} |\sigma\rangle\langle\sigma|_- |a\rangle\langle a|_m - i\underline{g}_{m}^* |\sigma\rangle\langle\sigma|_+ \left|a\right\rangle\left\langle^{\dagger}\right|_m,\end{aligned} \tag{A.35}$$

where

$$\underline{g}_{m} = i\sqrt{\frac{\omega^{(m)}}{\hbar\epsilon_0 L^{(m)}\mathcal{A}}} d^* e^{i\frac{\omega^{(m)}}{c}\ell_c} \sin\left[\frac{\omega^{(m)}}{c}(x_A + \ell_c)\right] + O\left(\epsilon^2\right). \tag{A.36}$$

B

Code availability

Due to pending publication (as of February 6th, 2023) of material in Chapter 5, the code will be made available after the material in this chapter has been published.

The codes available for the rest of this thesis are available in the following repository: `https://doi.org/10.5287/bodleian:VJBje0gxY`.